TACTILE SENSING WITH FIBRE BRAGG GRATINGS AND NEURAL NETWORKS

Barbara Mary Cowie

A thesis submitted to Aston University
for the degree of Doctor of Philosophy

ASTON UNIVERSITY
Photonics Research Group
Aston Triangle, Birmingham, B4 7ET, United Kingdom

June 2008

Abstract

This thesis describes novel developments in the use of fibre Bragg gratings with neural networks to achieve tactile sensing. The tactile sensing regime used here is known as distributive tactile sensing and comprises a small number of sensors monitoring a substrate (in this case a metal strip or a plate). The sensor output data are processed using one or more neural networks which have been trained using data collected previously. The spatial resolution of such a tactile sensor is much smaller than the inter-sensor spacing and information about a contacting load such as shape, size and orientation can be sensed. The difficulties and problems in using fibre Bragg gratings in this type of sensing have been explored, and a larger 'smart surface has been constructed which is capable of deducing information about a person standing on it.

Fibre Bragg grating sensors are usually expensive to interrogate, and part of this thesis describes a low cost interrogation system for a group of such devices which can be indefinitely scaled up for larger numbers of sensors without requiring an increasingly broadband light source. It incorporates inherent temperature correction and also uses fewer photodiodes than the number or sensors it interrogates, using neural networks to interpret the photodiode data.

Lastly a novel sensing arrangement using an FBG grating encapsulated in a silicone polymer is presented. This sensor is capable of distinguishing between different surface profiles with ridges 0.5 to 1mm deep and 2mm pitch and either triangular, semicircular or square in profile. Early experiments using neural networks to distinguish between these profiles are also presented.

The potential applications for tactile sensing systems incorporating fibre Bragg gratings and neural networks are explored.

INDEXING TERMS: fibre sensors, distributive tactile sensing, low cost interrogation, surface profile sensor.

DOCUMENT REVISION NUMBER: 1 (POST-VIVA)

Acknowledgements

I would like to acknowledge the help and support of the following people and organisations:

Dr David J Webb, my supervisor.

Betty Tam and Paul Slack of the Clinical Biomedical Research group at Aston University, with whom I collaborated for the experimental work in section 3.4.1.

Pensiri Tongapadungrod, whose work the smart surface in Chapter 4 extends and builds on.

Mark Broomby of Halcrow who produced the finite element analysis plots in chapter 4.

Andrew Main, with whom I collaborated for the work in Chapter 5.

Tom Allsop and John Williams of the Photonics Research Group, Aston University, with whom I collaborated for the work in chapter 6.

Bert Biggs who provided practical help in the Photonics Laboratories.

My proofreaders and my family who have been very patient and supportive.

I acknowledge the sponsorship of EPSRC, without whose financial support I could not have done this work.

The companies who gave me permission to use their photographs from their Internet sites to make this thesis more readable.

And those patient individuals who stood on one leg on the footplate in chapter 4 while I took measurements.

Contents

List of Figures

List of tables

Chapter 1 - Introduction

The work described in this thesis is by nature interdisciplinary. It combines elements from the fields of Photonics, Mechanical Engineering and Artificial Intelligence. The main body of the work concerns the application of optical fibre sensors to distributive tactile sensing. This type of sensing involves the use of neural networks to interpret the strain (or deflection) patterns set up in a flexible substrate when an object (or objects) make contact with it. A sensing scheme of this kind can be used to create a tactile sensor to determine various parameters of the contacting object – its position, contacting area, shape, weight and so on. Neural networks are trained to interpret the signals from the sensors by being provided with examples of strain (or deflection) data for known contact conditions. They can then interpret sensor data for unknown contacting objects and predict their parameters. The advantage of this type of system is that the position resolution is much smaller than the inter-sensor spacing, so that large scale sensors can be made with only a few sensing elements.

FBG sensors have been the subject of much research over the years, and are now considered to be a mature technology for such applications as the monitoring of large-scale civil engineering structures such as tunnels and bridges. However there are many other potential applications for optical fibre sensors which are less well developed. In particular the area of healthcare is one in which this type of sensing has potentially much to offer, and into which much research effort is being channelled. However whereas in the area of structural monitoring a 'raw' strain reading is an appropriate and useful output value for a structural

engineer to monitor, this is very rarely if ever the case in biomedical applications. One, or worse, a set of strain readings would be an irritating distraction for a surgeon who is performing a surgical procedure. It is in this context that the processing of FBG sensor data becomes important. If a set of sensor outputs can be automatically interpreted, preferably in real-time, by a processing system of some kind so that the system output is a 'high level' parameter, preferably conveying some information that the surgeon cannot already access by other means, then such a system could be an important advance.

This work builds on the experiences of other researchers who explored the possibilities of distributive tactile sensing but did not use the same types of sensors. One of the main applications of their work was the area of endoscopy, and in particular the area of developing an endoscope with tactile sensitivity. FBG sensors have distinct advantages in endoscopy compared with the other sensor types available.

Other areas of healthcare could also benefit from this approach, particularly if the sensor/processing system could be trained to offer some kind of diagnosis or treatment suggestion as its output. In the future this approach could potentially speed up diagnosis, or possibly make diagnosis of various conditions available in the GP surgery rather than requiring a visit to a consultant. An 'expert system' of this type could even be used by a school nurse for screening for asthma for instance, if a suitable system of sensors could be devised providing the required information to the processing system.

The area of podiatry is a suitable entry point into medical applications for this type of system since foot problems are common, so it should be possible to amass enough data to train a system, while foot and gait disorders are not in themselves life-threatening (although if they result in a lack of mobility this can cause or exacerbate life threatening conditions), so gaining confidence with this new type of system could be done without

serious consequences, particularly if it were used 'in parallel' with an established diagnostic method. For these reasons the footplate described at the end of Chapter 4 was chosen as a suitable practical application for these theoretical principles. There are also possible veterinary applications for gait analysis to which these ideas may be extended. The aims and objectives of this work were:

- To review the current developments in related technologies.
- To conduct experiments with Fibre Bragg Grating sensors in 1 and 2 dimensional distribute tactile sensing applications
- To examine and evaluate a lower cost method of interrogating FBG sensors for use in this type of application.
- To conduct experiments on a novel arrangement of optical fibre sensors encapsulated in silicone for tactile sensing applications.

The work is divided into five chapters. Chapter two is a literature review describing the background and current developments in tactile sensing, optical fibre sensors and neural networks. Chapter three describes work done using FBG sensors in a one-dimensional application such as would be used in an endoscope, including shape sensing and a direct comparison between FBG sensors and resistive strain gauges. Chapter four moves on to two-dimensional systems for detecting the position and shape of a contacting object and includes work on a footplate that has potential applications in podiatry, animal care or security systems. Chapter 5 describes a low cost interrogation system for the 2-dimensional systems seen in chapter 4, using chirped gratings which overlap in wavelength and effectively interrogate each other. Chapter 6 looks at a combination of FBG sensors and neural networks for tactile sensing, aimed at surface profile sensing in the 0.1-1mm range.

The last chapter presents conclusions and looks ahead to the direction of possible future work in this field.

Much of the work presented here has been published in peer reviewed journals and at conferences; a complete list is provided in Appendix 2.

Chapter 2 - Literature Review

Introduction

In this chapter a review of each of the components of the systems described in the remainder of the thesis is presented. Firstly the area of tactile sensing is explored, with particular reference to the potential use of artificial tactile sensing in endoscopy and the development of distributive tactile sensing; secondly Fibre Bragg grating sensors are described, including a discussion of their interrogation; lastly neural networks are explained, and compared with some alternative algorithms.

2.1 Tactile sensing overview

Tactile sensing is a developing field with a great number of potential applications. Although a great deal of research and development has been done in this area there is still a great deal of work to be done, particularly in the areas of robotics and minimally invasive surgery. In their review paper written in 1999, Lee and Nicholls [1] considered no fewer than 44 different types of tactile sensors and sensing systems, and concluded that:

> "... this survey has found increased emphasis and understanding of device materials, tactile sensing processes and requirements, the recognition of the value of results from dextrous manipulation and telepresence systems, and an emerging engineering approach to sensor packaging. All these, together with the application pull from medicine and service industries, bode very well for the next stage in the development of this fascinating field. Tactile sensors offer exciting possibilities for use in mechatronic devices and measuring instruments in many areas of science, and engineering robotics and industrial automation are the application areas that have generated the most

> interest because contact interactions are a fundamental feature of any physical manipulation system. However there are many other potential application areas including agriculture, food processing, medicine, dentistry, entertainment, and future domestic and service industries".

Maheshwari and Saraf [2] state that

> "... there is great interest in developing humanoid robots that can sense shapes textures and hardness and manipulate complex objects which are not readily possible by vision alone "

2.2 Human tactile sensing

The human tactile sense is highly developed and is capable of deducing a great deal of information about an object in a very short space of time – its surface texture, softness, slipperiness, the degree to which it is being gripped, its temperature, moisture content, discontinuities and vibration, and it is this sophistication that makes artificial tactile sensing such a challenging area of research and development. Human mechanical tactile sensing is achieved by 4 types of sensing structures in the skin, each of which responds to different types of tactile stimulus (see fig.1)[3,4]. Each sensing structure comprises a neuron and the structure surrounding its ending. The type of stimulus to which each type of structure responds is thought to be due to both the type of neuron and the type of sensing structure surrounding its ending.

1. The Merkel cell has the simplest structure; it is a special type of cell in the base layer of the epidermis that surrounds a slowly adapting type of mechanically sensitive neuron (mechanoreceptor). These cells discharge continuously in response to sustained pressure and are sensitive to the edges, corners and curvature of objects held in the hand.
2. Meissner corpuscles are relatively large groups of cells in the dermal ridges that lie just beneath the epidermis. They comprise layers of cells that cushion and surround the endings of between two and six of a rapidly adapting type of mechanoreceptor. This pillow-like arrangement protects the neuron endings from longer-term tactile stimuli,

allowing them to be selectively sensitive to rapid tactile transients. Meissner's corpuscles are most numerous in the finger pads. Together with the Merkel cells they provide the tools for delicate work on textured surfaces such as cotton or wood, or on embossed surfaces such as Braille text. Elevations as small as 5 microns in height can be detected.

3. Pacinian corpuscles are found in the dermis and deeper tissues. They are large structures, each surrounding a single rapidly adapting type of nerve ending that is extremely sensitive and can detect deformation in the nanometre range. The overlying layers of skin protect the receptor from the very large, low frequency stresses and strains of normal activity. Pacinian corpuscles are the size of rice grains. There are about 300 in a hand and they are particularly responsive to vibration. Pacinian corpuscles discharge one or two impulses when compressed, and again when released.

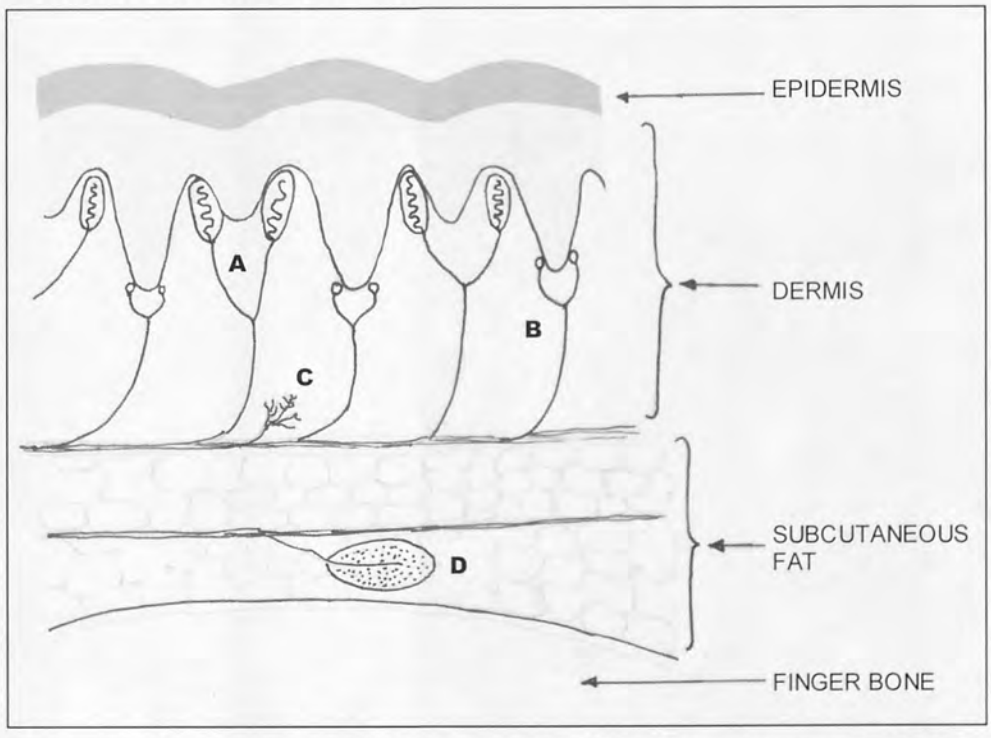

Fig 1. The structure and nerve endings in the human fingertip [4]. A Meissner's corpuscles, B Merkel Cells, C a group of Ruffini endings, D a Pacinian corpuscle

4. Ruffini endings, which are located in the connective tissue of the dermis, are tied into the local collagen matrix. This makes them selectively sensitive to skin stretch and drag (shearing stress). The neurons connecting to Ruffini endings are slowly adapting.

Although artificial tactile sensors do not yet seek to emulate simultaneously all the mechanisms found in the human sense of touch by using 4 types of sensors to achieve detection of objects, study of the human system can assist the understanding of the types of tactile stimuli involved. Often a tactile sensor is developed to replicate a single aspect of human tactile sensing which is particularly important to the application involved, for example the authors of [5] have found that the PVDF (polyvinylidene fluoride) film used in their sensors emulates the action of Pacinian Corpuscles. In Chapter 6 a system is investigated that attempts to emulate the action of Meissner's corpuscles and Merkel cell-neurite complexes, described in 1 and 2 above, in their ability to detect roughness and small ridges in the surface of a contacting object.

Emulating the human sense of touch is particularly important when handling delicate, soft, deformable items, since it enables such objects to be handled without damage, while detecting the onset of slippage so that the object can be gripped more firmly if necessary. The human tactile sense can also detect the hardness and texture of a contacting object, and emulating this type of sensing is particularly sought after in the area of minimally invasive surgery. In traditional surgical procedures a surgeon is able to palpate an area of tissue to detect lumps, blockages, or to assess the condition of an organ, for example to detect gallstones. In minimally invasive surgery this is not an option open to the surgeon, and the possibility of developing endoscopes incorporating tactile sensors, to restore the sense of touch to the surgeon, is highly desirable.

Maheshwari and Saraf [2] state that:

> "Sensation of touch, primarily the determination of stress distribution over the area of physical contact between the sensor and the object surfaces, is a critical component to advance minimum invasive surgical procedures by giving the surgeon a "touch sensation" to decipher, for example, cancer tissue and gallstone using the signal from tactile sensor".

The work described in chapters 3 and 4 of this thesis shows how Optical Fibre sensors can be used in a distributive tactile sensing system to achieve aspects of human-like touch. Optical

fibre sensors have very low material costs and could potentially be used in a disposable version of an endoscope with tactile sensitivity.

2.3 Endoscopy

Etymologically, the word 'endoscope' is derived from the Greek prefix *endo*, meaning 'within', and the verb *skopein*, meaning 'to observe' [6]. Endoscopy thus means looking inside, and usually refers to looking inside the human body for medical reasons.

The use of endoscopes is not limited to medical applications however, they are also used for other applications such as automotive diagnostics [7] (fig 2), contraband search operations [8], building survey work including investigation of cavity wall tie corrosion [9] and termite infestations [10], veterinary applications including snakes [11], fish [12], and horses [13], inspecting trees for the presence of bats [14], dentistry [15], inspection of nuclear fuel cells [16] and other inaccessible or hazardous areas, and inspection of soldered joints under ball grid array electronic components [17]. Tactile sensitive endoscopy would be useful in some of these applications, for example in automotive engineering the ability to sense the degree to which the bore of an engine cylinder was scored may be useful.

2.3.1 History of Endoscopy

The first endoscope, the Lichtleiter, was designed by a German doctor called Bozzini in 1805. It was used for inspecting the urethra and bladder, and used a candle for its source of light.

Further development of endoscopes was halted for the next 50 years however, because his medical contemporaries ridiculed the device. In 1853 a French doctor, Desormeaux, produced a similar device using a brighter light source which used a burning mixture of paraffin and turpentine. Despite causing burns to the patients, this device was considered successful. In 1869 Trouve used electrically generated light in a similar device, and in 1877 Nitze improved the arrangement by introducing an iced water-cooling system and telescopic lenses, and it is he who is credited as being the father of cystoscopy [18].

It was the invention of optical fibres in the 1950s that enabled rapid advances to be made in the field of endoscopy, since the light could then be guided along a flexible path without the use of a complex arrangement of lenses and prisms.

However it was the development of Charge Coupled Devices (which convert optical data into electrical current and can be used in low-light environments, resulting in both improved quality of images and decreased size of the endoscopic systems) allowing the magnification and projection of images onto television screens, that allowed the techniques of endoscopic (or laparoscopic) surgery to become truly integrated into general surgery [19].

2.3.2 Endoscopic Surgery

Endoscopic surgery (also called minimally invasive or keyhole surgery) is a technique that involves the use of endoscopes allow a surgeon to perform a surgical procedure inside the body cavity through a very small incision. Normally one endoscope is used for observation and carries light and imaging equipment, while a second endoscope carries tools for performing the surgical procedure. Neurosurgeons have also developed endoscopic

applications as alternatives to traditional open procedures. Endoscopic surgery is used for the treatment of hydrocephalus, arachnoid cysts, spinal tumors and pituitary tumors [20].

The advantages of minimally invasive surgery are clear, for example when endoscopic surgery is used to remove gallstones: because the abdominal muscles are not cut, patients have less pain and fewer complications than they would have had after surgery using a large incision across the abdomen. Recovery usually involves only one night in the hospital, followed by several days of restricted activity at home [21]. Conventional gallstone surgery required a week's stay in hospital followed by up to 3 months of restricted activity.

The size of endoscopes has decreased in recent years so that smaller cavities can be explored, e.g. the cavity surrounding the spinal cord [22], and they have become more flexible.

Minimally invasive surgery requires as few instruments as possible to be inserted into the patient. Typically one endoscope is used to provide vision systems to the surgeon, and a second for surgical tools (although for minor procedures and biopsies these are combined into a single endoscope). To introduce tactile sensitivity into minimally invasive surgery it would not be acceptable for a third separate instrument to be used purely for tactile sensing, so it is necessary for one of the existing endoscopes to be instrumented for this purpose. This means that only certain types of tactile sensor would be suitable for this application – they must occupy very little space and withstand being sterilised between surgical procedures.

2.4 Artificial Tactile sensors

Artificial Tactile sensors fall into three broad groups: individual sensing elements, arrays of sensing elements each working individually to build a tactile 'image', and distributive tactile sensing systems where sensors act as a group and the resulting data are interpreted using pattern recognition techniques. Arrays of tactile sensing elements have received the greatest amount of attention from researchers, with a great amount of development effort going into making the individual elements as small as possible to improve the spatial resolution of a

device. However one particular challenge in the application of tactile sensing to endoscopy is how to present the tactile information to the surgeon. The human brain is extremely good at data selection, disregarding unwanted information in a particular context and focussing on the relevant data. Artificial tactile sensing systems will only become useful in a surgical setting when the surgeon can be presented with tactile information that is precise, concise, relevant and quickly understood.

Eltaib and Hewit [23] in their review of Tactile sensing technology for minimal access surgery conclude that

> "The design and fabrication of tactile sensors have received the greatest attention to date and a number of reasonably effective arrays are becoming available. Tactile data processing is still fairly rudimentary and much effort is needed to provide surgeons with meaningful and useable information. The field of tactile sensing is likely to be a fruitful one for a number of years while the difficult problems of trying to emulate the human tactile facility are tackled. However, the benefits to minimal access surgeons of regaining their lost sense of touch are immense".

Artificial Tactile sensors can be broadly categorised into 3 groups: individual sensors, arrays and distributive tactile sensing systems.

2.4.1 Individual Sensors

Individual sensors based on various types of transducers have been described; according to Lee and Nicholls in 1989 [24] they were predominately resistive, capacitive, and piezo-electric. These types of sensors still predominate [25, 26, 27], but sensors using such diverse sensing mechanisms as optical [28], mechanical [29], elastomer [30] and nanoparticles [2] have also been reported. The disadvantage of many of these sensor types for applications such as endoscopy is that they are too large to be fitted into an endoscope, and would not withstand being sterilised.

2.4.2 Arrays of sensing elements

Arrays of sensors have been developed using capacitive [31], resistive [32], piezoelectric [33] and other types of sensing elements. These arrays of sensors are typically used in an

arrangement where each sensing element is a 'tactel' or 'taxel', individual sensors whose outputs are ideally independent of each other and often linear, and a picture of the tactile environment is built up in the same way as an image is created from its component pixels. This results in a large number of sensing elements, particularly if a large sensing area is required, with a large number of electrical connections and a resulting high computational load.

2.4.3 Distributive Tactile sensing

Distributive tactile sensing is distinct from the array type of system. The principle of a distributive tactile sensing system exploits the deformation of a homogenous flexible medium of reliable, repeatable behaviour under contact, which is monitored by a group of sensors. The outputs from these sensors are interpreted not individually but as a group, and the sensor outputs need not be linear and should ideally not be independent of each other, rather crosstalk between the sensors is useful. The grouped output data are interpreted by a neural network, which is trained to recognise patterns in the sensor data and interpret them to provide information concerning the contacting object. The advantage that this type of system has over arrays of sensors is that it can be scaled to cover large areas without increasing the number of individual sensors, since the spatial resolution achievable is smaller than the distance between sensing elements. Also, because the number of sensing elements is smaller for a given area than an array type sensor the computing load is smaller and the speed of data processing much faster for a large sensing area.

2.4.4. Origins of Distributive Tactile Sensing

Distributive tactile sensing had its origins in 1994:

In 1994 [34] Holweg and Jongkind used neural networks to interpret the patterns in data from a 256-element tactile matrix sensor with a rubber surface being used to grip an object. The neural network was able to distinguish the shape, position and orientation of the object. This

was one of the first tactile sensing systems to use neural networks, however the sensors were still a traditional array type.

Also in 1994, Ellis et al [35] described the use of two thin stainless steel plates, each with 4 strain gauges, as a tactile sensor to detect the mass and length of a rod grasped between the two plates. Thin plate theory was used to calculate the mass and length of the test loads, which were longer than the plates sensors and so overhung the edges. This system interpreted the sensor outputs collectively rather than individually, and the resolution of the system was smaller than the inter-sensor distance, but the authors did not use neural networks to interpret the data.

Peter Brett [36-39] was the first to call this type of tactile sensing "distributive". In a personal interview with him (2005) he said "…. I was the first to determine that this approach was a plausible solution to tactile sensing and I termed it 'the distributive approach' to tactile sensing. I was working with one of my research assistants Rhodri Stone at Bristol University at the time (1992-1996). We started by looking at how to sense, by tactile means, the contact pressure transients from within a robotic gripper (Parallel plate) when gripping and manipulating dough-like materials. From this work we determined that meaningful information could be gained directly from the static response of a surface produced by a contacting object. Most of the surfaces were somewhat simple. The work really advanced onto surfaces …….. with Pensiri Tongpadungrod, [40,41], one of my research students who completed her Bristol PhD in 2002."

In 1995 Stone and Brett published a paper [42] comparing 3 methods of interpreting data for tactile sensing. They found that using a neural network was at least as accurate as using an optimisation of parameters approach and more accurate than using a direct model approach. The optimisation of parameters approach was found to be more computationally intensive than the direct model, which could run at 30Hz. The paper does not mention the comparative

computation time using the neural network; however neural networks, once trained, are very simple algorithms which have a fast execution time, so the implication is that neural networks were found to be at least as accurate and potentially faster than the other two techniques. The mechanical arrangement used for this comparison was a thin aluminium plate, clamped at one edge, with a load distributed evenly across its width (i.e. parallel to the clamped edge) and was part of a project to develop mechanical handling equipment for non-rigid materials such as dough, detecting deformation and slippage of the load. The plate had 8 strain gauges arranged in a line perpendicular to the clamped edge.

In 1997 [43] Brett and Stone extended this work to applications in minimally invasive surgery by using crude optical fibre sensors attached to a nylon flexible substrate within a plastic bellowed tube. Three optical fibres were mounted along the length of the tube, each one being cut through so that any misalignment caused by the curvature of the nylon substrate would decrease the amount of light transmitted along the fibre. The relationship between the radius of curvature of the tube and the sensor outputs was non-linear. The magnitude of an applied load and the load position were predicted using a neural network to interpret the sensor data.

In 1997 Stone published his thesis [44]. In it he described an experimental 2 dimensional tactile sensing surface, which used neural networks to detect the shoe size of a person standing on the plate. The position and orientation of the person's foot was controlled by a mechanical stop. Using just 2 sensors it was possible to correctly detect the size of a person's shoe 80% of the time.

In 2000 Brett and Li [45] used a similar system to create a tactile keyboard with 35 'zones' but using only 5 sensors. The sensors each comprised a light emitting diode and a photodetector which were mounted under the surface pointing upwards towards a patch of reflective tape on the underside of the sensing surface. The amount of light reflected back

towards the photodetector varied as the sensing surface deflected, thus the sensors effectively measured displacement (ambient light was excluded).

In 2002 Tongpadungrod [46] used Principal Components Analysis and a genetic algorithm to optimise the position of the sensors used in both 1 and 2 dimensional distributive tactile sensing systems. She found that the optimised positions were not very different from the evenly spaced positions, particularly for larger numbers of sensors on a given substrate. Tongpadungrod used a 2d tactile sensing plate to detect the position, shape, size, weight and orientation of a load [47]. This system used infrared proximity sensors (see fig. 52 in 4.1)

In 2004 Tam extended the 1d system work for endoscopy – she demonstrated a system which could detect the number of contact points (one or two), the distance between the contacting points, the direction of the load and the stiffness of contact. The system processed 25 samples per second [48,49].

She concluded that this kind of sensing could be used to give an endoscope tactile sensitivity that would not only locate the position of touching but also the quality of touch i.e. the hardness/texture of the object being touched. The sensors used in this system were resistive strain gauges.

2.5. Optical fibre sensors

Optical fibre sensors have distinct advantages compared to other sensor types. They are immune to electrical noise (they could for instance be used inside a magnetic resonance imaging scanner), can be multiplexed and can be used in reflection so that only a single connecting fibre is required to serve a group of sensors. Optical fibre sensors are also small and light - a typical Fibre Bragg Grating (FBG) has a length of between 5 and 20mm and a fibre diameter of 250μm (125μm without coating). They are also resilient to temperatures up to 400°C [50] and pressures up to 100MPa [51] which could allow them to be used in surgical instruments requiring sterilisation. They can also be embedded into polymer [52] or

composite materials [53]. Optical sensors have already been applied to biomedical problems requiring sensor sterilisation such as pressure sensing for intra-aortic balloon pumping therapy [54], precision liquid level sensing [55] and cell chemical sensing [56]. Optical fibre sensors also have an expected lifespan of at least 25 years (after proper stabilisation by annealing) [57]. This compares favourably with strain gauges, which can only reliably be used for 1-2 years, due to problems of debonding between the electrical leads and the strain gauge rosette. [58]

2.5.1 Fibre Bragg Grating Sensors

An FBG is a longitudinal periodic variation of the index of refraction in the core of an optical fibre (fig. 4). The discovery of the first Fibre Bragg Grating was made in 1978 by Hill et al [59], who used germanium doped silica optical fibre to make a narrowband reflector. FBGs work on the principle of Bragg reflection. When light propagates through alternate regions of higher and lower refractive index, partial reflection occurs at each interface between those regions. If the spacing between those regions is regular and such that all the partial reflections add up in phase the total reflection can grow to nearly 100%. Clearly this condition will only occur for a specific wavelength, which is called the Bragg wavelength. For all other wavelengths the reflections are not in phase, indeed they interfere destructively and the net reflected amplitude is close to zero, resulting in high transmission [60].

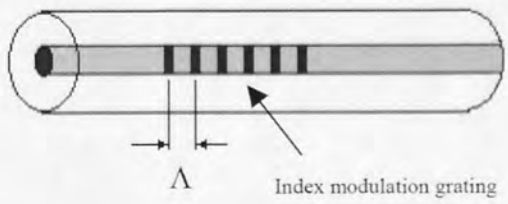

Fig. 4 Fibre Bragg grating schematic

The effect of the grating is to make the fibre into a highly wavelength-selective mirror. If broadband light is directed through the grating, a narrow band of light (typically between 0.5nm and 1nm) will be reflected (fig. 5).

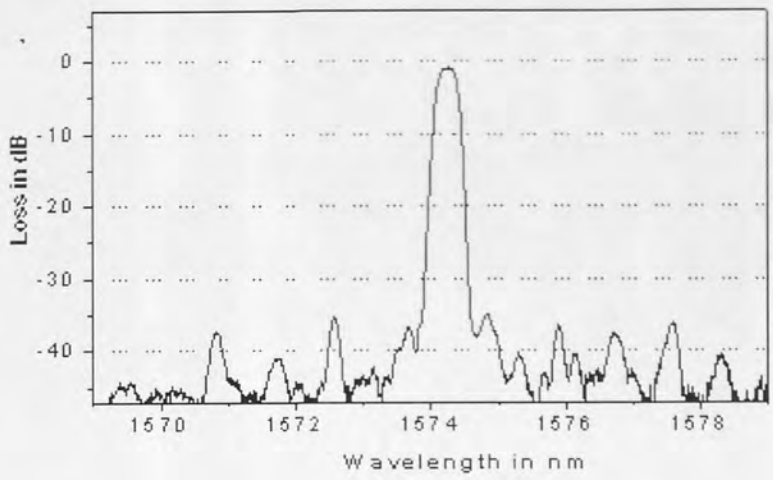

Fig. 5 Typical FBG reflected spectrum

The wavelength of the reflected light is given by: $\lambda_B = 2n\Lambda$ [61], where λ_B is the peak reflected wavelength or Bragg wavelength, n is the effective refractive index of the fibre core and Λ is the period of the grating (fig. 4). When the fibre is subjected to an increase in strain or temperature, both n and Λ are affected and the Bragg wavelength increases. For silica fibre, the wavelength–strain sensitivity at 1550nm has been measured as 1.15 pm/με, and the wavelength-temperature sensitivity as 13 pm/deg C [61].

Fibre Bragg Grating sensors are sensitive not only to temperature and strain but also to a number of other measurands, however for the purposes of this study they are used exclusively as strain sensors. FBGs are made by exposing the optical fibre to UV radiation, and gratings can only be inscribed because silica glass is photosensitive.

2.5.2 Photosensitivity

Photosensitivity is the term used to describe a change in the value of the refractive index of an optical fibre in response to light. An optical fibre irradiated by laser UV light will show a change in its transmission properties due to a permanent change of the refractive index. This is a non-linear phenomenon. Hill *et al* [62] first discovered the UV photosensitivity of optical fibres in 1978; however although there has been a great deal of research into photosensitivity, it is still not fully understood.

No one theory can explain photosensitivity in all cases; but although there is still disagreement on the subject, there is consensus that photosensitivity is a combination of several effects and that the relative contributions from each effect differ according to type of fibre, the way the fibre is prepared (hydrogenation, UV irradiation, flame brushing, etc) and the way it is inscribed

The three main mechanisms thought to underlie photosensitivity are:

1. Colour Centres (light absorption centres) which are caused by molecular level point defects in silica glass. These colour centres absorb light at a particular wavelength and molecular changes occur to these point defects which cause the refractive index of the glass to change. [63] Silica glass is chemically Silicon dioxide (SiO_2) in which Silicon atoms bonds oxygen atoms in the ratio 2:1. Each Silicon atom forms 4 covalent bonds with oxygen atoms, each oxygen atom forming 2 covalent bonds with silicon atoms. In Carbon dioxide (which is chemically related to SiO_2) each carbon atom forms two double bonds with each of 2 oxygen atoms, however silicon is a bigger atom than carbon and can only form a single covalent bond with each oxygen atom. Each oxygen atom forms one covalent bond with each of two neighbouring silicon atoms, and a large crystal structure is formed which has an empirical chemical formula of SiO_2 but does not contain molecules with this formula (fig. 6). [64]

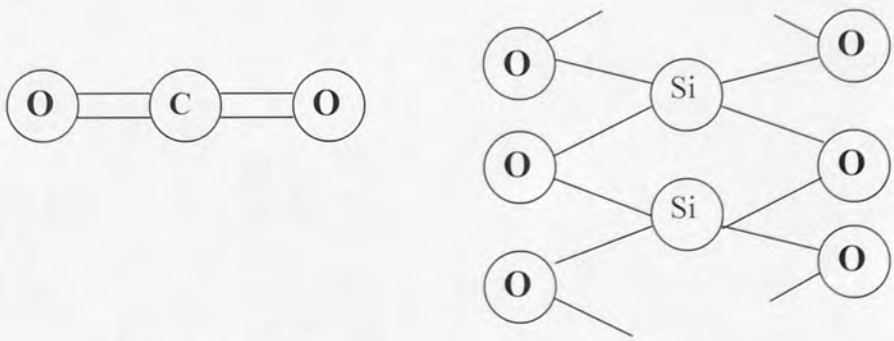

Fig. 6 Covalent bonds of Carbon Dioxide (left) and Silicon Dioxide (right)

Within the silica lattice there are also 'wrong' bonds, where Silicon atoms bond in different ways with the oxygen atoms causing defects in the crystal structure of the glass. Three different types of defects in silica glass have been identified: the E' centre, the nonbonding [or nonbridging] oxygen hole centre (NBOHC), and the peroxy centre (fig 7) [65]

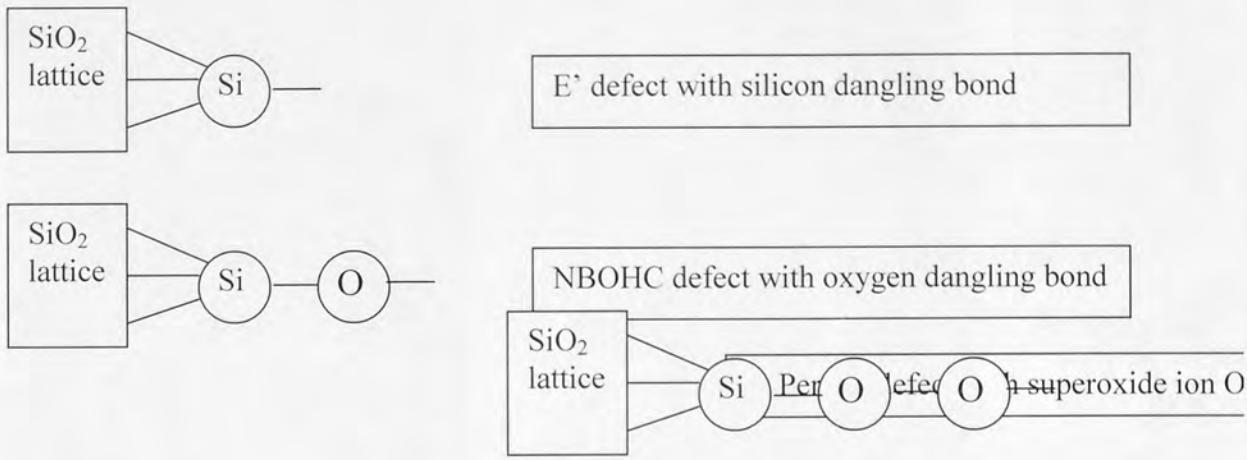

Fig. 7 Molecular structure of defects in silica glass

Although it is generally acknowledged that this is one of the main mechanisms responsible for photosensitivity, the exact nature and photochemistry of these colour centres are uncertain [66].

2. Densification – the change of the density of glass due to UV exposure. It has been shown that when a grating is inscribed into glass periodic corrugations appear along the surface, showing that the volume of the glass has decreased where the glass was exposed to bright UV fringes. [67] This increase in the density of the glass causes a corresponding increase in its refractive index.

3. Structural relaxation – When an optical fibre is being manufactured, it cools quickly when it has been drawn. The outer cladding layer cools more quickly than the inner core, so stresses are set up in the fibre. The localized heating effect of the UV laser light causes relaxation of the thermoelastic stress in the core of the fibre and therefore changes the refractive index. [68]

4. Physical Damage – some gratings are written using very high energy short pulses of light which are highly focused onto the fibre core. This causes physical damage and very large changes in refractive index. [68] This technique can also be used to store information in optical media. [69].

2.5.3 Coupled Mode Theory

Coupled Mode Theory is a mathematical method used to analyse the light propagation in optical fibres. There are two approaches for analysing the behaviour of fields in any kind of waveguide structure. The first is to solve Maxwell's equations in that structure. The second method is to express the fields in the waveguide as a sum of the individual modes of light propagating in the structure. The first method should give correct results, but only the simplest cases are possible to solve analytically. The second method yields only an approximate answer, but is often the only way a solution can be found. The main assumption made by coupled mode theory is that the coupling between the modes is weak. Even in a single mode fibre there are at least 2 modes to be considered, the incident and the reflected modes.

Erdogan [70] used coupled mode theory to show that the bandwidth of the spectral peak reflected by a Bragg grating of length L is given by:

$$\frac{\Delta\lambda_o}{\lambda} = \frac{s\overline{\delta n}_{eff}}{n_{eff}}\sqrt{1+\left(\frac{\lambda_d}{s\overline{\delta n}_{eff}\,L}\right)^2}$$

Where n_{eff} is the effective refractive index of the fibre, $s\overline{\delta n}_{eff}$ is the "AC" part of the induced index change, $\Delta\lambda o/\lambda$ represents the bandwidth of the reflected spectral peak, and λ_d is the inscription wavelength.

The general form of the relationship between spectral width and grating length can be deduced from this equation. A longer exposed length generally produces a narrower bandwidth FBG. When the value of the expression within the square root sign is much greater

than one the spectral width varies as 1/L. However as L increases the value of that expression decreases until the 1 becomes the significant quantity and no further length-related change to the spectral width occurs. The authors of [71] used this equation to simulate the results shown in fig 8.

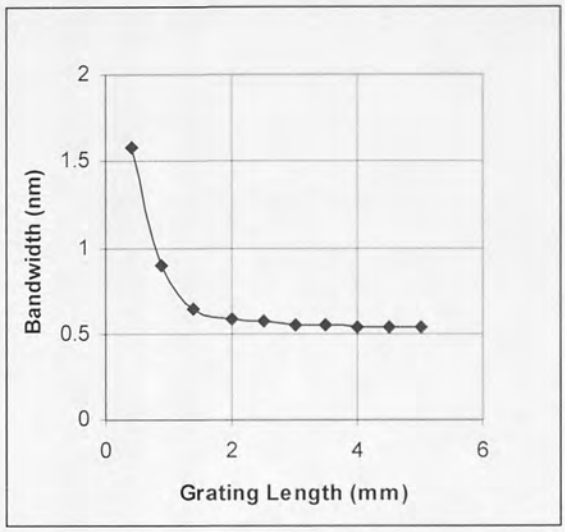

Fig. 8. Relationship between grating length and bandwidth

In practice spectral widths larger than this are usually obtained because of practical difficulties including imperfections of laser and lens alignment. Most of the gratings seen in the following chapters had spectral widths of about 1nm with a length of 10mm, spectral width not being an important parameter for most of the experiments performed.

2.5.4 Fabrication of Fibre Bragg Gratings

Fibre Bragg Gratings are made by taking a length of single mode optical fibre, subjecting it to high pressure hydrogenation to increase its photosensitivity, and then subjecting the core of the fibre to an intense interference pattern of ultra violet light. The wavelength generally used is 244nm from an argon ion laser. There are three commonly used methods for achieving this: the phase mask method, the holographic method and the direct write method. (FBGs can also be made using germanium doped silica fibre, and there are also several other dopants used to

increase the photosensitivity of fibre for sensor inscription, however the most frequently used conditions are those described here).

2.5.4.1. Phase Mask method

A phase mask is made from a flat sheet of silica glass, which is transparent to ultraviolet light. On one of the flat surfaces a pattern of periodic surface relief corrugations is etched using photolithographic techniques. The corrugations are of the order of micrometers in period and depth. The shape of the periodic pattern approximates a square wave in profile. The optical fibre is placed almost in contact with the phase mask, at right angles to its corrugations as shown schematically in fig. 9. Ultraviolet light, which is incident normal to the phase mask, passes through it and is diffracted by the periodic corrugations. Usually most of the diffracted light is contained in the 0, +1 and –1 diffracted orders with a substantial proportion in the zero order. However, the phase mask is designed to suppress the diffraction into the zero order by careful choice of the depth of the corrugations in the phase mask. In practice the amount of light in the zero order can be reduced to less that 5% with approximately 80% of the total light intensity divided equally in the +/-1 orders. The pitch of the corrugations determines the wavelength of the Bragg grating. [72] The picture below (fig 9) has been exaggerated for the purpose of clarity.

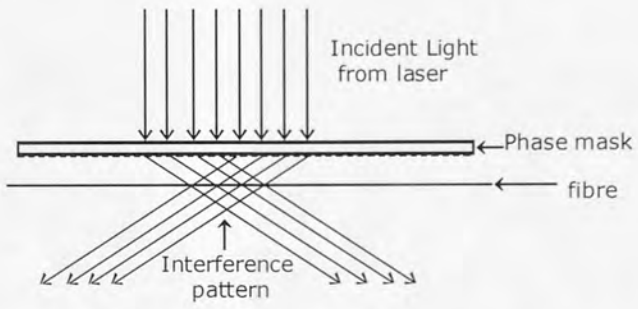

Fig. 9 Phase mask method of grating inscription

The periodicity of an FBG is one half of that of the phase mask as the fringe pattern results from the interference between the ±1 diffraction orders of the phase mask. The beam from the

laser is traversed along the phase mask and fibre by means of a precision translation stage. A typical FBG has an exposed length of 10-20mm. The strength of the grating (i.e. the transmission loss in dB at the Bragg wavelength) is determined by the speed of traverse of the beam and the laser power. A higher laser power and slower traverse will produce a stronger grating. The degree to which the fibre is hydrogenated will also have an effect (more hydrogenation will generally produce a stronger grating) and the presence of various dopants in the silica fibre will also affect the FBG strength. If FBGs are required to be written at wavelengths other than the wavelength determined by the phase mask geometry, the fibre can be strained during inscription so that after inscription, when the strain is released, the wavelength of the resulting grating is shorter than would have been written into unstrained fibre. In this way gratings of wavelengths up to 2nm shorter than the phase mask used can be achieved. This technique was used to produce the 9 grating arrays used in chapter 4, where the phase mask available had only 5 different sets of corrugations. The disadvantage of using this method is that unless measurement equipment is included in the inscription apparatus to measure it, the amount of strain applied is not known at the time of inscription, so it is only after the grating has been made and the strain released that the wavelength of the grating is known. Also very firm clamping arrangements must be available for the strained fibre, otherwise it will slip during inscription and produce a collection of small weak gratings at different wavelengths instead of one strong grating.

2.5.4.2 Holographic Method

The holographic (interferometric) technique creates the UV interference pattern by splitting the UV light into 2 separate light paths and recombining them at the optical fibre location (fig 10). The two beams are guided to the optical fibre by two mirrors. The wavelength of the Bragg grating is determined by the angle of intersection of the two beams, which is controlled

by the angles of the two mirrors, and also the wavelength of the laser itself. This technique requires precision and careful adjustment.

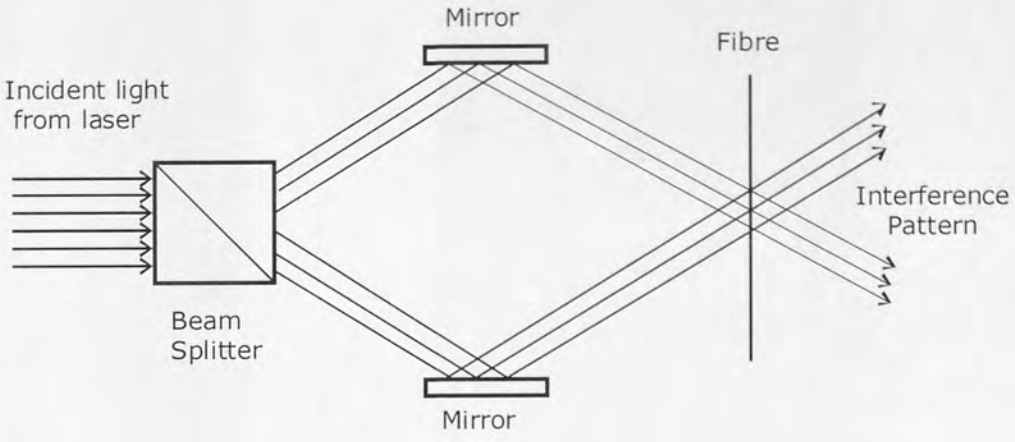

Fig. 10 Holographic method of grating inscription

Other advantages of the phase mask method are that it is easier to align the fibre since it is aligned with the phase mask rather than the diffraction pattern of the beams of light, and lower coherence requirements on laser beam because the wavelength of grating is dependent on the phase mask period and not on the laser wavelength.

2.5.4.3. Direct Write Method (also called Point-by-Point)

The laser beam is focussed to a spot size equal to the required period of the FBG. A short but intense pulse of UV light is directed onto the fibre. The fibre is then moved one grating period in a direction at right angles to the beam and the process is repeated. An extremely high precision translation stage is used and the entire process is under computer control. It is usually done in a clean room. This process is used in commercial manufacture of optical fibre gratings and is also a popular way of writing Long Period Gratings (LPGs), which as their name implies have a longer period than FBGs and so require slightly less precision in the writing equipment. It has the advantage that wavelength of the grating produced is not related to the laser wavelength, and that a simple change of computer settings will result in a different FBG wavelength.

2.5.5 Chirped gratings

Chirped Fibre Bragg gratings (CFBGs) have a wider spectral peak than Bragg gratings. These gratings can be made by axially varying either the period of the grating or the index of refraction of the core or both. Special chirped phase masks are available with a varying pitch of corrugations along their length.

2.5.5. Blazed FBGs

In a Blazed or tilted Bragg grating the bands of varying refractive index are tilted at an angle to the fibre axis. Light which otherwise would be guided in the fibre core, is coupled into the loosely bound, guided cladding or radiation modes. The bandwidth of the radiated light is dependent on the tilt angle of the grating planes and the strength of the index modulation.

2.5.6. Long Period Gratings

The long-period grating (LPG) has a period typically in the range 100 μm to 1 mm. The LPG promotes coupling between the propagating core mode and co-propagating cladding modes. The high attenuation of the cladding modes results in the transmission spectrum of the fibre containing a series of attenuation bands centred at discrete wavelengths, each attenuation band corresponding to the coupling to a different cladding mode. An example of the transmission spectrum of an LPG is shown in figure 11. [73]

The wavelengths of the attenuation bands can be calculated using the formula:

$$\lambda = [n_{eff}(\lambda) - n^{i}_{clad}(\lambda)]\Lambda$$

where $n_{eff}(\lambda)$ is the effective refractive index of the propagating core mode at wavelength λ, $n^{i}_{clad}(\lambda)$ is the refractive index of the ith cladding mode and Λ is the period of the LPG.

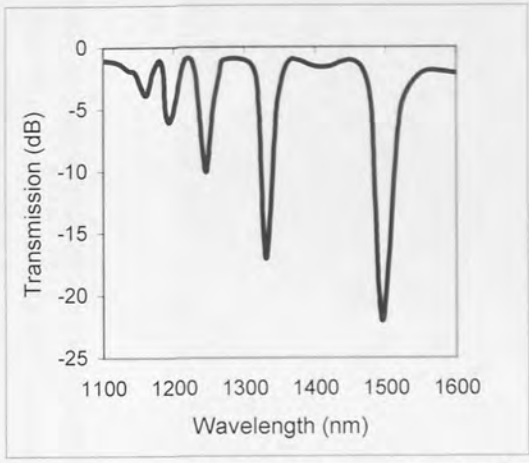

Fig. 11 Transmission characteristic of an LPG fabricated in SMF-28 with period 320μm

2.5.7. Multiplexing FBG Sensors

There are two main systems for multiplexing several sensors on a single fibre. One is Wavelength Division Multiplexing (WDM), and this is the system used in Chapters 3 and 4. Each sensor is fabricated so that it has a different reflective wavelength, and the system described below (section 2.5.8) is used to interrogate the sensors. The second system is Time Division Multiplexing (TDM). A Time Division Multiplexed sensing system utilises identical, low reflectivity Fibre Bragg Gratings that all have the same reflective wavelength. The principle of operation of such a system is based on the time-of-flight of signals returning from the individual sensors. A single, short pulse of light from a broadband source is launched down an optical fibre containing the gratings located at various positions along the length of the fibre. When the pulse reaches the first grating in the array, a small percentage of light will be reflected from the grating at a wavelength determined by the strain and temperature (or some other measurand) experienced by the first grating. This reflected signal is detected and analysed by the interrogation unit whilst the remainder of the pulse of broadband light continues to propagate down the fibre. At each subsequent grating the same process occurs, so that the interrogation unit receives a number of pulses, one from each grating. These pulses arrive at a time determined by the grating distance from the

interrogator, and thus one grating can be distinguished from another in the array by analysing the timing of the pulse arrival [74].

2.5.8. Interrogation of Fibre Bragg Gratings

Fibre Bragg grating sensors are interrogated by a variety of methods. In laboratory situations a broadband light source and an Optical Spectrum Analyser (OSA) are used, with a 50/50 optical splitter (3dB coupler) (fig 12). The Optical Spectrum Analyser detects the single narrowband spectral peak reflected by the FBG sensor. Any changes in the wavelength of that peak due to the change in ambient temperature, strain on the sensor or change in some other measurand can be recorded and quantified. In the experiments conducted in the following

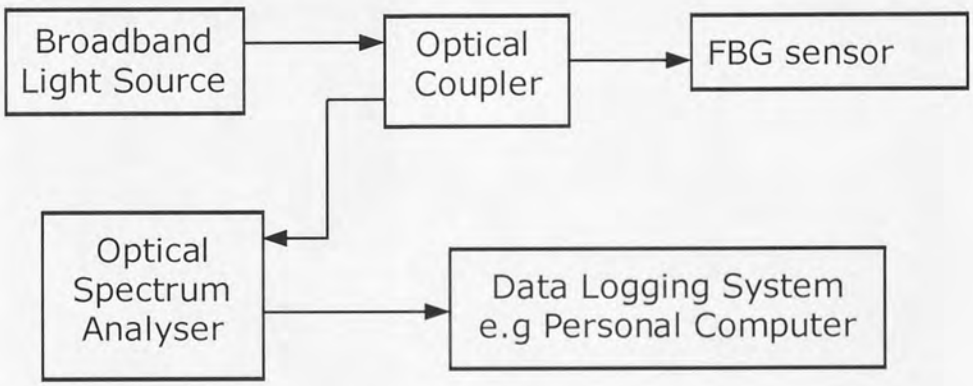

Fig. 12 Schematic of interrogation system for FBG sensors

chapters a PC running LabView [75] was used for this purpose. However, this system is expensive (a new system could cost around £50,000) and not very fast. The refresh time for the OSA could be as fast as 10Hz if a narrow wavelength band was being monitored, but if several FBGs at different wavelengths are being monitored simultaneously a broader spectral width must be monitored, and the OSA refresh time (and hence data sampling rate) could be much slower. During the experiments conducted in the following chapters the OSA refresh rate was typically once every two seconds.

Other methods of interrogating FBGs have been investigated:

Simpson et al [76] used a blazed FBG and an array of 2048 Charge-Coupled devices (CCD) (photodetectors). Blazed FBGs (BFBGs) have the property that the angle at which light is emitted from the side of the grating is dependent upon its wavelength. As the wavelength of the spectral peak being reflected by the grating under interrogation changed (due to a change in the measurand) the area of the CCD array being illuminated by the light emitted from the side of the BFBG changed, giving an indication of the magnitude of the measurand.

Norman et al [77] used a 40 channel arrayed waveguide grating to interrogate an FBG. As the wavelength of the spectral peak changed in response to a measurands, the amount of light arriving at each channel of the AWG changed. Each channel was monitored electronically and the peak wavelength reflected by the FBG was calculated

Cusano et al [78] used an optical fibre filter and a simple photodetector to measure strain (fig. 13)

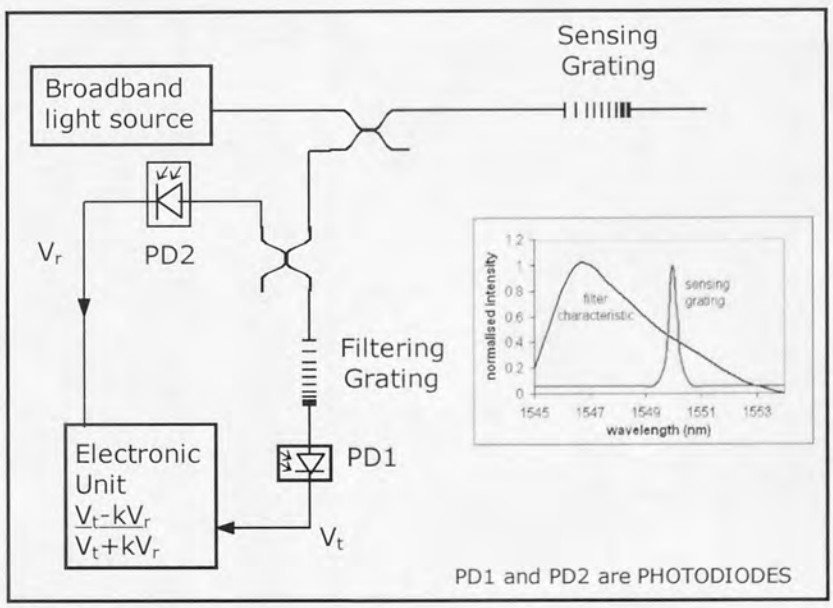

Fig. 13 Schematic Of Sensing System used by Cusano et al [78].

The optical fibre filter was an FBG with an asymmetric characteristic as shown in fig 13 which was made by curving the optical fibre in the plane of an apodised phase mask.

The wavelength of the spectral peak reflected by the grating was such that when it was not under strain almost all the light was blocked by the filter. However, as the strain on the

grating increased and the reflected spectral peak increased in wavelength, progressively more light was transmitted through the filter to the photodetectors. The disadvantage of methods based on light intensity measurement is that source intensity fluctuations translate directly into errors in strain measurement. Some method of compensating for these fluctuations is required, and in the arrangement seen above the outputs from the two photodiodes labelled PDR and PDT are both affected equally by source fluctuations, so after the mathematical processing shown these variations cancel out.

Fallon et al [79] used a long period grating to interrogate an FBG in a similar manner (see fig 14):

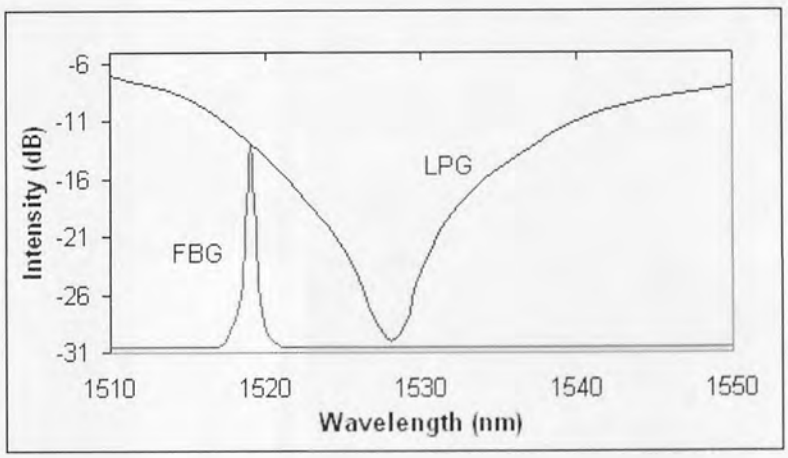

Fig 14 Spectra of the FBG strain sensor and the LPG used for interrogation [79]

Romero et al [80] used a Chirped FBG in the same way, again compensating for any changes in source power by measuring unfiltered source power in a second photodetector and mathematically adjusting for source power fluctuations. All three of these similar arrangements described (78,79 and 80) used a greater number of photodiodes than the number of sensors being interrogated. This adds to the cost and complexity of such a system.

Chapter 5 describes a low cost interrogation system using chirped gratings that uses fewer photodetectors than the number of gratings being interrogated. Neural Networks are used to interpret the output voltages of the photodiodes into meaningful measurements.

Commercially available FBG interrogation systems are available from Insensys [81] Smart Fibres Ltd [82], FosTa [83], Micron Optics [84], FOS&S [85] and others. These interrogators are usually priced between £2000 and £20,000 depending upon the number of sensors they can simultaneously interrogate, the accuracy, the speed (no. of scans per second) and the bandwidth they are capable of scanning.

Until recently it has been the case that for small changes in a measurand, so that variations of the order of a few pm in wavelength are to be measured, an Optical Spectrum Analyser and a high quality broadband light source are required. Newer interrogation systems are becoming more sensitive e.g. the Micron Optics Si425 interrogator claims 0.2pm repeatability [86].

An OSA gives a digitised version of the spectrum observed by the spectrum analyser. For very small changes in wavelength the way in which this digital information is translated into a single value representing the central wavelength reflected by the FBG becomes significant. There are various ways of extracting this central value. One way is to carry out a polynomial fit to the most significant points of the curve. Another is to calculate the centroid of the peak, and a third way is to use the 'Full Width at Half Maximum' algorithm.

2.5.8.1 Polynomial fit

A spreadsheet program such as Microsoft Excel can be used to carry out a polynomial fit to a set of data, generally using a Least Squares method to achieve the fit. There are a number of factors to be considered in this case, in particular the number of data points to attempt to fit, the order of the polynomial to be used and the shape of the grating characteristic. If the decision is made to fit a polynomial to 'all points which fall above a certain power level' or 'the 12 points with the highest power level' then there can be a problem when there is a transition between one set of points being used and the next, or where there is borderline uncertainty as to which points to include for the curve fit. The result is shown below in fig.15,

where the points on this graph should all fall around 1548.412nm, but it can be seen that intermittently the value falls to around 1548.405nm. This happens when a new point is included in the polynomial fit, or when a point is no longer included. This is a kind of

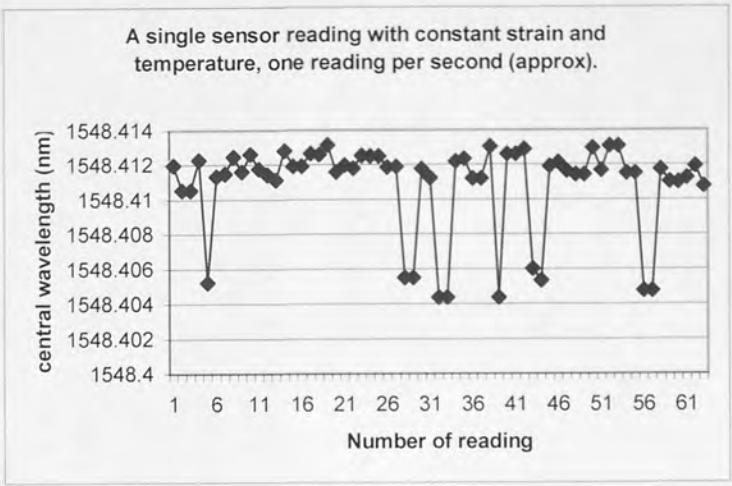

Fig 15 Digitisation error due to central wavelength extraction algorithm

digitisation error and is unavoidable, although it could be decreased by including more points in the polynomial fit so that the effect of changing one of the points used is not so pronounced, or by reducing the weighting given to points near the edge of the sampling window, both of which would add to the complexity of the calculation and so the calculation time.

Another factor to be considered is that although the ideal shape of the reflection spectrum of an FBG is symmetrical and similar to a sync function or a Gaussian, this is not always the case in practical applications. Also where an FBG is mounted onto a substrate using adhesive (as seen in chapter 3,4 and 5) there can be strains set up in the FBG as the adhesive cures which alter the characteristic shape and make it more difficult for a satisfactory polynomial fit to be achieved. In this case a slight change in strain and therefore a change in the spectral points which are used for the polynomial fit could yield a disproportionately large change in the result of the peak detection algorithm, indeed there may also be some uncertainty between 2 possible 'best fit' solutions which might result in the effect seen in fig 15, as the algorithm

switches between the two possibilities. There may also be unexpected changes in the best-fit curve as the strain experienced by the grating changes if the adhesive does not take up the strain evenly so that some regions of the FBG are strained more than others. This will cause the shape of the grating characteristic to change with strain in a way that does not necessarily reflect the changes in strain applied, for instance if one region of the grating remains relatively unstrained while the remainder becomes subject to a greater strain the spectral peak will become distorted and the best fit curve will have a peak at a lower wavelength than reflects the actual strain experienced by the grating.

To illustrate the point, fig. 16 shows the 17 most significant spectral points around the peak of 4 of the 9 gratings used in chapter 4, with second order polynomial fits added using Microsoft Excel:

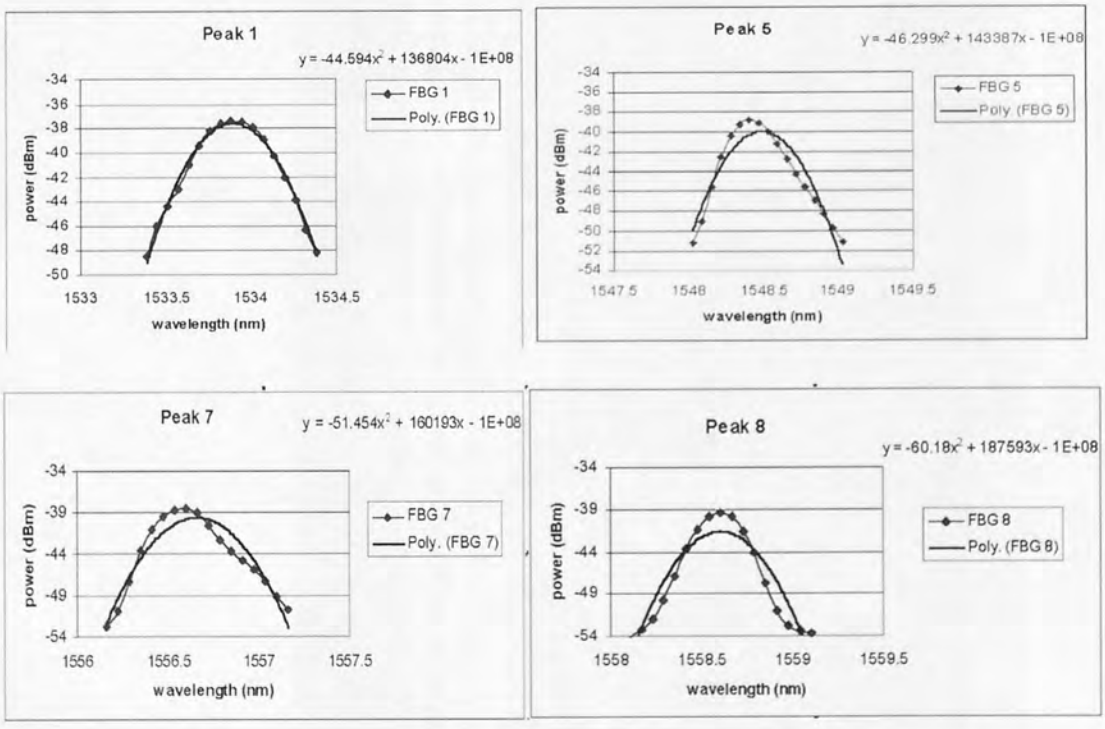

Fig 16 Examples of 2nd order Polynomial fits to FBG spectral peaks

Peak 1 shows a peak that is well suited to a polynomial fit, whereas Peaks 5,8 and 9 are less well suited. One advantage of using a quadratic fit in particular is the simplicity in calculating the peak wavelength from the equation of the quadratic curve.

2.5.8.2 Centroid algorithm.

The centroid detection algorithm described in [87] uses the algorithm in Equation (1), where i_j and λj represent the intensity and the centre wavelength of the jth pixel respectively and where λ_B is the Bragg wavelength:

$$\lambda_B = \frac{\Sigma_j \lambda_j i_j}{\Sigma_j i_j} \qquad (1)$$

This expression represents a moving average that evaluates the wavelength of the spectral peak to within a fraction of the wavelength separation between adjacent pixels. The number of pixels chosen used to evaluate the expression in equation (1) should be large enough to give stable wavelength resolution and minimise the effect seen in fig. 15.

Ezbiri al [87] compared the two methods and concluded that both the centroid detection method and the least squares /polynomial fit methods could be used, but that the quadratic curve fit method gave the most stable results

2.5.8.3 Mean of half maximum

This method involves calculating the mean wavelength at half the maximum amplitude of the spectral peak (see fig. 17). . Linear interpolation between the two data points above and below the 'half maximum amplitude' value is used to find the two values of wavelength from which to calculate the mean.

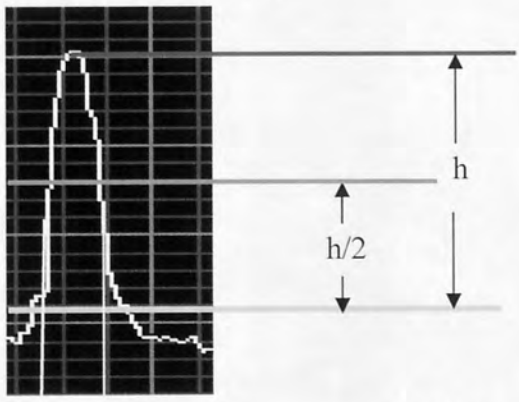

$$\lambda_B = \frac{\lambda_1 + \lambda_2}{2}$$

Fig. 17. Mean of half maximum algorithm

This method was used in the experiments described in chapter 4. This algorithm was implemented in the Labview software which was used to capture and interpret the Optical Spectrum Analyser output data.

Dyer et al [88] compared the performance of the 3 peak detection algorithms described here and found that the third of the three algorithms was slightly more accurate than the other two. Others have also considered a spectrum correlation technique [89] and a digital filtering technique [90].

The comparison of the various algorithms and techniques for peak detection usually involve some trade-off between accuracy, signal to noise ratio and computational load. In the applications discussed in this thesis the absolute values of peak wavelength are not as important as the change in peak wavelength in response to strain. An absolute error in wavelength detection, provided it is constant for every experiment, would not be an issue. Computational load is possibly an issue since the algorithm used was written in MatLab code and executed within a Labview program.

2.5.9 FBG applications

Fibre Bragg grating sensors have been used for strain sensing in a variety of applications:

- Structural monitoring of buildings [91] (although some doubt has been cast on the suitability of optical fibres for direct embedding in concrete [92]), bridges [93], tunnels [94], ships [95], lock gates [96], aircraft [97] and structures for deployment in space [98]. Figs 18 and 19 illustrate some of these applications:

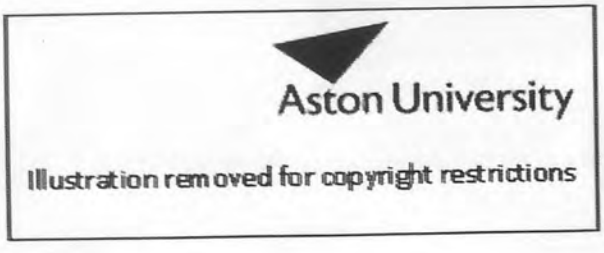

- Monitoring composites for strain and damage [100] and for cure monitoring [101].
- Shape reconstruction, in this case for endoscopy [102].
- And other applications.

2.6. Computational Algorithms

Computational algorithms are used to deduce meaning from sensory data by forming relationships between the sensory input and expected output.

2.6.1 Neural networks [103,104]

In 1943 McCulloch and Pitts suggested information processing by means of interconnected simplified neurons. After the initial enthusiasm most researchers abandoned the field when Minsky and Papert showed disadvantages of perceptron models in 1969. A renewed interest in neural networks emerged in the early eighties after some important theoretical results by Rumelhart and McClelland, and because advances in computer hardware provided increased processing capacities. This meant that neurocomputing became attractive for many applications outside computer sciences. Nowadays applications for neural networks can be

found in robotics, image processing, data and speech recognition, and increasingly in new areas of mathematics and physics [105].

Neural Networks are used to solve problems where the mathematical relationships between the inputs and the outputs of a system are not known, but a large amount of data is available so that the network itself can infer the relationships (the meaning of 'large' will be discussed later). A neural network uses training data (complete sets of input data for which the corresponding complete output data are known) to build up a model which links the input and output variables. The resulting model is consistent (in that the same input pattern will always produce the same answer) but contains no explicit rules. Neural networks can be used in applications which are too complex to model mathematically, and are also widely used in pattern recognition. [103 p8]

Traditional techniques using programmed mathematical equations are used where the exact rules linking the inputs and outputs of a system are known. The functions inferred by neural networks are non-linear and are particularly powerful for categorisation tasks. A neural network's ability to generalise means that it is able to learn from noisy or incomplete data [103 p10].

Programming Approach	Neural Computing approach
• Follows Rules	• Learns from data
• Solution formally specifiable	• Rules are not visible
• Cannot generalise	• Able to generalise
• Not error tolerant	• Copes with noise

TABLE 1. The main differences between traditional programming based software development and a neural computing approach [103 p9].

The mathematical model a neural network builds is made up of a set of simple functions linked together by weights. The weights describe the effect each simple function (or unit) will have on the overall model. The simplest type of neural network is the Multi-Layer Perceptron

(MLP) (Also called a back propagation network or a feed forward network). An MLP has a set of input units, whose function it is to take input values from the outside, a set of output units which report the final answer, and a set of processing hidden units which link the inputs to the outputs (fig 20). [103 p10]

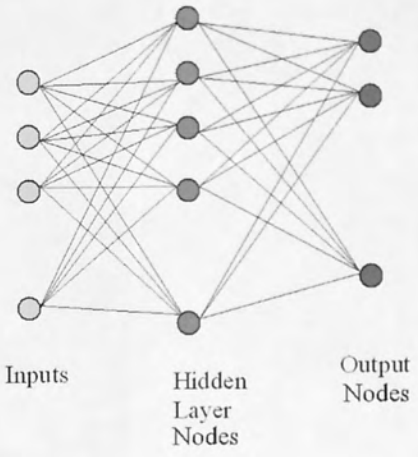

Fig. 20 Structure of Multilayer Perceptron with single layer of hidden nodes

Each node (fig. 21) is essentially a summing junction which calculates the weighted sum of its inputs, followed by an activation function (fig. 22, 23). The activation function can take a variety of forms, including linear or various kinds of threshold function. The weights, shown here as W1, W2, etc., are simple multipliers which are set up by the network during the training process and optimised.

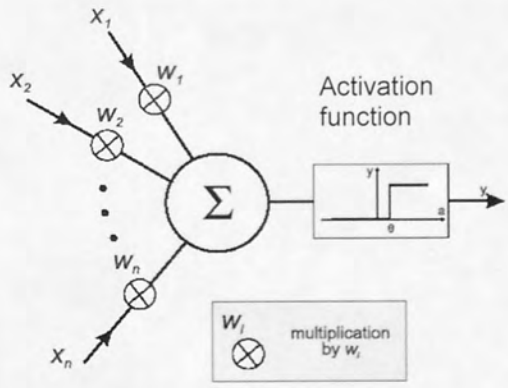

Fig. 21 Structure of Neural Network Node

The transfer function (or activation function) of a node can accept input in any range, and produces output in a strictly limited range (it has a squashing effect). Although the input can be in any range, there is a saturation effect so that the unit is only sensitive to inputs within a fairly limited range. For this reason input variables must be scaled before they are used. One of the most common transfer functions, particularly useful for classification tasks, is the logistic function (also sometimes referred to as the sigmoid function (fig 22). In this case, the output is in the range (0,1), and is sensitive to input values in a range not much larger than (-1,+1).

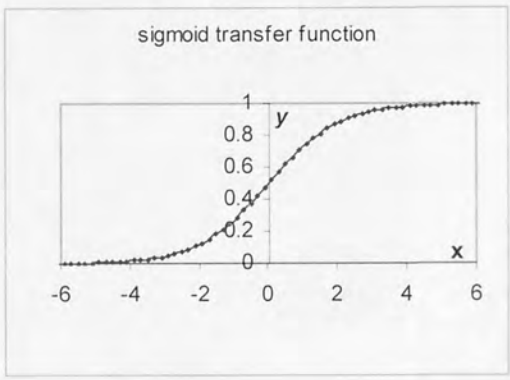

Fig. 22 Sigmoid transfer function

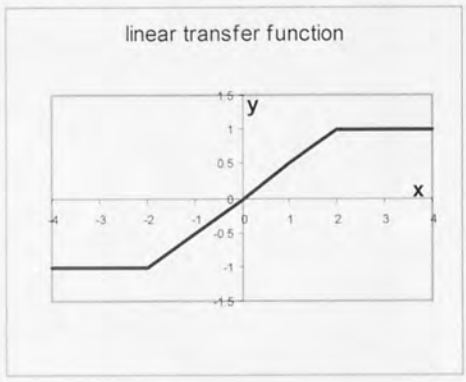

Fig. 23. Semi-linear transfer function

The function is also smooth and easily differentiable, facts that are critical in allowing the network training algorithms to operate (this is the reason why the step function is not used in practice) [106]. A semi-linear transfer function is used when a linear interpolation task is performed (fig 23).

2.6.1.1. Choosing the neural network architecture

There is no reliable system for predicting the best architecture (i.e. number of hidden layers and nodes) to use for a given problem; this has to be arrived at by training a range of networks in turn and finding out which produces the lowest residual training error.

It is generally accepted that:

- a simpler model leads to a network with better generalisation ability (ability to produce a good answer to a problem for which it has not been specifically trained) [103 p 15].
- networks with just two layers of weights are capable of approximating any continuous function mapping, providing the number of hidden units is sufficiently large [104 p116].
- there is a trade-off between building a model which generalises well, and one which is more accurate. A more general model describes a smoother curve through the training data points, missing some but resisting the effect of noise or peculiarities which might be present [103 p15].
- the number of hidden units required for a classification task increases with the number of classes in the task, i.e. the number of separate regions into which the input space must be split.
- larger networks require longer training times.
- if a data set contains noise, there is a chance the network will fit its model to the noise. Fewer hidden units decrease this chance.
- if the number of hidden units is smaller than either the number of input or output units, then the relationship inferred by the network is not the most general possible [104 p121].
- In some applications there can be an advantage in building a lot of structure into the network by using a large number of hidden nodes.
- For a given network having M hidden nodes, the residual error decreases as (1/M) as the number of hidden nodes increases [104 p132].

In the experiments described here, neural networks were 'built' with numbers of hidden nodes beginning at a number equal to the number of outputs (1, 2 or 4) and incrementing by one until the minimum error achievable began to deteriorate consistently. Typically numbers of hidden nodes from 2 to 40 were trained, although larger numbers of nodes were sometimes used.

2.6.1.2. Training a neural network

2.6.1.2.1 Collecting the data

Neural networks learn from examples of inputs and their corresponding outputs. Two sets of data are needed, some for training and some for validation. At least 20% of the total data should be used for validation. Noisy data needs a larger training data set. Training data can be derived experimentally (as was generally done in the work presented here) or artificially, for example by using a mathematical model to generate ideal sensor values for given conditions, then adding noise to those values to create a spread of data.

Training data should be evenly distributed over the signal space to be modelled, even if that means generating some data artificially, so that the neural network has examples of all possible input/output combinations.

2.6.1.2.2. The 'Curse of Dimensionality'

As the number of inputs grows, the amount of training data required to allow the network to be able to fit to the data grows exponentially.

> "If each input variable is divided into M divisions (cells), then the total number of cells is M^d (where d is the number of inputs) and this grows exponentially with the dimensionality of the input space…this implies that the quantity of training data needed to specify the mapping also grows exponentially" [104 P7-8].

The number of cases required for neural network training frequently presents difficulties. There are some heuristic guidelines, which relate the number of cases needed to the size of the network (the simplest of these says that there should be ten times as many cases as connections in the network). Also the number needed is related to the (possibly unknown) complexity of the underlying function which the network is trying to model, and to the variance of the additive noise. As the number of variables increases, the number of cases required increases nonlinearly, so that with even a fairly small number of variables (perhaps fifty or less) a huge number of cases are required. This problem is known as "the curse of dimensionality"

> "Feed-forward neural networks are much less susceptible to the curse of dimensionality, these techniques are able to exploit two important properties of real data. First, the input variables are generally correlated in some way, so that the data points do not fill out the entire input space but tend to be restricted to a sub-space of lower dimensionality. Second, for most mappings of practical interest, the value of the output variables will not change arbitrarily from one region of input space to another, but will typically vary smoothly as a function of the input variables. Thus, it is possible to infer the values of the output variables at intermediate points, where no data is available, by a process similar to interpolation." [104 p7-8]

This is true for the experiments in chapter 4 concerned with load position, but not for shape detection where interpolation between, say, a triangle and a square is not a useful concept.

2.6.1.2.3 Scaling the data

It is necessary to scale the data before training, so that every value falls within a given range. Ensuring that every variable covers the same range ensures that errors on each variable contribute the same proportion to the change in network weights. This is often achieved by is normalising each variable to zero mean and standard deviation of one. Linear scaling can also be used, but it works best when the data are spread evenly over their range. Using linear scaling on a data set which contains outliers, or an uneven spread of values, results in a large proportion of the data values being squashed into a small part of the input range, leaving most of the rest unused [103 p31]. Scaling the data also ensures that the hidden units do not become 'saturated', i.e. produce very large values which are then compressed by the activation function so that data is effectively degraded or lost.

2.6.1.2.4. Training the network

MLPs learn by a process called back propagation of error, which involves calculating the error at each output and changing the values of the weights which led to the error. The training data set and the validation data set are both sets of sensor output values for which the corresponding contact conditions (in this case) are known. These are propagated through the neural network and an error value is generated. This error value represents the difference between the neural network's output in response to the validation inputs and the actual

validation outputs. Training a neural network is an iterative process in which the values of the weights are optimised so that the training error is minimised (Fig. 24).

This process of learning is known as gradient descent. A problem associated with gradient descent is that of local minima which are dips in error space which are not the universal minimum. An algorithm designed simply to always reduce error will not be able to climb out of a local dip to continue descent to the true lowest point. The standard back propagation

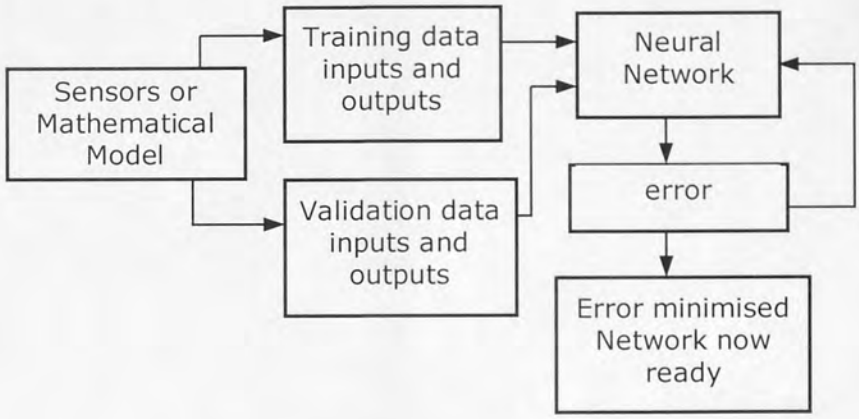

Fig. 24 Neural Network training process

algorithm makes use of two parameters which control the rate at which the leaning takes place. A momentum term, which causes the weight changes to be affected by the size of the previous weight changes, is used to avoid local minima. The learning rate tells the network how slowly to progress. The weights are updated by a fraction of the calculated error each time to prevent the network making large swings about the best values without ever achieving optimisation [103 p13-14].

There are two types of training:

(1) Train with a single pattern of data, and update weights after each pattern.

(2) Train with a whole set of data patterns and update weights after each batch or epoch. Errors are calculated and stored after each pattern, then weights are recalculated at the end of each epoch.

Batch mode is faster and calculates a more accurate weight change, but needs more memory to store the error values over an epoch. In the experiments described here batch training was used.

2.6.1.3 'Smart Surfaces' using Neural Networks

Systems using sensors and neural networks to create an 'intelligent' surface are not in themselves novel. Leung and Payandeh [107] used neural networks with an array of pressure transducers to detect the position and shape of an object; however the sensors each gave a simple two state output, '1' for a detected object and '0' for no detection, and the size of the object was much greater than the spacing between the elements of the array, so the approach could not be described as distributive.

Canepa et al [108] used an array of sensing elements made of piezoelectric polymer films to detect the onset of incipient slippage. 16 sensors were used, arranged in pairs, one transducer of each pair being sensitive to normal stresses while the other detected the shear stress along the direction of the array. A neural network was used to process the data from the sensors to detect the onset of slippage.

Pati et al [109] used a neural network to compute the solution to the inverse problem of tactile sensing, using sensor outputs as the neural network inputs and solving a linear equation. They used a second analytical equation to generate the error more usually produced from a set of validation data. The neural network continued to be trained as long as the error was above a certain (small) value. The disadvantage of this kind of use of neural networks is that the neural network has to be trained for every new set of sensor inputs. The authors found that using a very simple network (4 nodes) the training took at least 1ms, and was expected to be slower than this for most experimental data. This negates one of the most powerful advantages of using pre-trained neural networks in the traditional way, i.e. that they have a

fast execution time and so are suitable for real time sensing systems. The sensors they used were piezoresistive sensing elements embedded in an elastic substrate.

Worth and Spencer [110] used neural networks to deduce the angle of contact between a solid rod and a tactile cylindrical 'finger' having a 5 x 5 array of capacitive strain sensing elements embedded below its surface. The data used to train the neural network came from a mathematical model of a tactile sensing finger created for the Stanford DPL Hand. The pressure distribution resulting from the indentation of the finger is an ellipsoid, the shape of which changes with the radius and angle of the impinging rod. To produce the training data for the neural network, the strain in the sensor's rubber "skin" was calculated for each of the tactels in the array. The authors found that neural networks were a very successful way of dealing with this kind of data (albeit theoretically derived), and that good results for predicting the angle of the contacting rod were produced.

Watkins et al [111] used Extrinsic Fabry–Perot interferometric fibre optic sensors and a neural network to provide delamination detection for 8 ply laminated glass/epoxy composite beams. Each beam was arranged as a cantilever and excited by a piezoelectric actuator at frequencies up to 1 kHz. The first five modal frequencies of each beam were determined using the sensors. The neural network used these modal frequencies to predict the size and location of delaminations in the beams. The neural network was trained using theoretically derived data from classical-beam theory and tested using the data obtained experimentally. The average errors in predicting the size and position of the delaminations were 5.9 and 4.7% respectively.

L Zapico *et al* [112] used neural networks to assess structural damage in a 2-storey building using 15 accelerometers (outputs sampled at 1Hz) and a 5kg instrumented hammer. The Netlab neural networks software used in this thesis was also used by these authors. Training data were derived experimentally using a finite element analysis model. The inputs to the

neural networks were the natural frequencies and mode shapes of the structure, and the authors attempted to predict the type of damage sustained to the building. Results for damage at floor level were 'reasonable'.

Staszewski et al [113,114] used neural networks combined with genetic algorithms to find near-optimal sensor locations for damage detection on a composite box panel. Piezoceramic sensors were used to measure the time-varying strain at locations on the test piece and neural networks were used to determine the location and amplitude of impacts. The genetic algorithm was used to determine the optimum sensor locations, particularly for a fail-safe system (i.e. one that has a very low probability of failing to detect an impact). This work has applications in the aerospace industry.

Caiti et al [115] used a 21 x 21 array of tactels to detect the shape of an object. Each tactel detected two stress components, one shear and the other the normal stress. The array covered an area of 1cm x 1cm. The sensors were piezoelectric and made of PVDF crystals which were mounted on a rubber deformable 'skin'. Their system was able to correctly reconstruct the shape of an object with an average of 95% accuracy.

Tseng et al [116] used an artificial skin ridge made from a piece of rubber 2cm x 1cm x 1.5mm with a piece of PVDF film 1cm x 1cmx 40μm bonded to it. The PVDF acted as a single sensor, whose output was interpreted by a neural network. The system was capable of distinguishing between 7 different Braille symbols as the sensor was passed over them. The time taken per symbol was 1 second, and 2048 samples were taken over this time. A success rate of 100% correct detection was achieved.

Neural networks have also been used in sensing applications such as:

-the inspection of foundry pieces using ultrasonic sensors [117]

-accurate estimation of the shape of precision spaceborne optical systems [118]

-controlling shape memory alloy actuators [119]

-damage detection in smart structures [120]

-crack damage detection [121]

-vibration suppression [122]

-monitoring of fatigue damage, failure prognostics and service life prediction [123]

-structural damage detection in a helicopter rotor blade [124]

-semi-active control of buildings and structures for earthquake hazard mitigation [125]

-chemical sensing e.g. detection of water/ethanol/air [126] and detection of ammonia [127]

2.6.1.4. Other applications of Neural Networks

Other applications of neural networks include investment analysis [128], signature recognition [129], process control[1309], diagnosis of diesel[131] and aircraft engine faults [132], and marketing[133].

2.6.2 Other Algorithms

Neural Networks are not the only algorithms used for the solution of problems where the relationship between input and output data cannot be directly mathematically modelled : others include Genetic algorithms, Fuzzy logic and Lazy learning algorithms.

2.6.2.1 Genetic Algorithms

Genetic algorithms (GAs) are powerful and widely applicable stochastic search and optimization algorithms based on the principle of natural selection and genetic evolution [134].

Genetic algorithms are good for solving a problem where the form of the answer is known i.e. some form of mathematical relationship between the input and output variables must be assumed before a genetic algorithm can be used to solve the problem. For example, if a polynomial solution were suitable a genetic algorithm could be used to optimise the values of

the co-efficients, assuming some random starting values. These co-efficients would be encoded into binary values, the 'bits' of which would be optimised by crossover, mutation and fitness evaluation, with the 'fitter' solutions surviving to a subsequent generation of processing.

Genetic algorithms have been used with sensors and actuators in order to optimise the locations of the actuators to suppress noise transmission of a vibration plate [135]. This use of genetic algorithms is typical in that the optimum solution or solutions to a problem are found once and then applied. The computation time is then not particularly important, indeed in [135], the time required for the genetic algorithm to select an optimal model was "only 25 minutes". Genetic algorithms are usually very computationally intensive, since they search large numbers of possible solutions to a problem before arriving at a solution. In fact, for some very complex problems it is beneficial to use a network of computers in parallel to run a genetic algorithm, each computer evaluating the 'fitness' of possible solutions under the control of a 'master' computer. Using a genetic algorithm for the problem of decoding strain data from the type of smart surface described in chapter 4 may entail the algorithm finding a new solution every time the load on the plate changed, and thus would be very computationally intensive, also the time required would be unpredictable.

Genetic Algorithms can be used to solve problems such as optimising sensor locations, but are not generally used for real-time applications. Also, they have the reputation of being "very easy to lead to premature convergence, especially in multidimensional nonlinear optimisation problems" [135].

The fact remains that if a suitable form of analytical relationship is not available, genetic algorithms cannot be used. The systems used in chapters 3 and 4 are not readily analysed, indeed Lee and Nicholls [24] stated that:

2.6.2.2 Fuzzy logic

Fuzzy logic relies on a system of 'If...then' statements to control the output of such a system. Each set of training data forms such a statement, so for a 9 sensor system performing shape sensing, (as in chapter 4) the 'If' part of the statement would contain the 9 sensor output values and the 'Then' part would contain the shape information. Some of these rules may conflict, for example if the same shape resulted in a different sensor outputs for some reason. Each rule is assigned a 'degree' (priority) and 'conflicting rules' are discarded, only retaining the rule which has the highest 'degree'. The fuzzy controller learns from the remaining data and can be used to classify new input data. The computational load increases with the required accuracy of the output.

Fuzzy systems are often used when the input variables are not clearly defined values but may occupy a range, e.g. 'small' or 'large'.

The first step in developing a fuzzy analysis framework is modelling the input variables as fuzzy variables. The process of quantifying a fuzzy variable is known as fuzzification. This is done by constructing a membership function (possibility distribution) for the variable. The membership function takes on values between 0 to 1. [136] The general arrangement of a Fuzzy system is shown in fig (25). The output of a fuzzy logic system is usually a probability distribution predicting what the response of a system will be. In the case of shape recognition and other classification tasks this is appropriate, but the linear interpolation task of determining where a load is located given the input strain values is less well suited to this type

of system. Fuzzy logic systems have been successfully used in control applications e.g. vibration control in smart structures. [138].

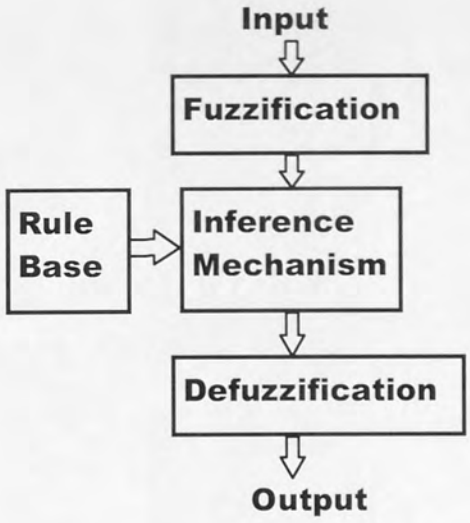

Fig. 25 General arrangement of a Fuzzy system. [137]

2.6.2.3. Lazy learning algorithms [139]

Lazy learning algorithms are characterized by three behaviours:

1. Defer: They store all training data and defer processing until queries are given that require replies.

2. Reply: Queries are answered by combining the training data, typically by using a learning approach in which (1) instances are defined as points in a space, (2) a similarity function is defined on all pairs of these instances, and (3) a prediction function defines an answer as a function of query similarity.

Flush: After replying to a query, the answer and any intermediate results are discarded.

It is the deferring aspect of Lazy learning algorithms that makes them less suitable than Neural Networks in the applications seen in this thesis, since this will make such a system run more slowly in real time.

Quiroga and Rabelo [140] compared the use of Machine Learning, Neural Networks and

Fuzzy Logic in manufacturing control applications, specifically robot motion control and basic job shop scheduling. The 3 systems all achieved over 90% success, but the Neural Network was found to be the most accurate, had the fastest execution time (once it had been trained) and achieved the best results when incomplete data was available or in the presence of noisy data.

2.7 Summary

The current developments in tactile sensing, optical fibre sensors and computational algorithms have been outlined, with particular reference to those used in the following chapters. We have examined the complexity of the human sense of touch, and looked at some of the methods by which artificial tactile sensing is achieved, with particular reference to distributive tactile sensing. We have looked at the uses of endoscopes and noted that, particularly in medical applications, touch sensitivity would be a useful advance. Optical fibre sensors of various types, their fabrication, interrogation and uses have been reviewed, and computational algorithms, particularly neural networks, have been examined. This gives the background for the work seen in the following chapters.

Chapter 3 - Experiments with 1d systems

In this chapter we investigate:

1. The suitability of FBG sensors for shape detection and reconstruction,
2. The appropriate length of a grating for use in an endoscope designed to negotiate tight bends.
3. The application of distributive tactile sensing to a one-dimensional tactile sensing system, comparing the use of FBG sensors with conventional resistive strain gauges

3.1 Introduction

The use of endoscopes for clinical investigations and minimally invasive surgery has been increasing in recent years [141]. Those used purely for visual investigations of fairly large cavities e.g. the colon have been available for many years (see section 2.3.1), but in more recent years smaller cavities such as e.g. the naso-pharyngeal cavity and spinal cord cavity [22] have been investigated; also endoscopes with greater functionality are required e.g. for taking biopsies, performing surgery etc. As a result some endoscopes need to be very slim (2-3mm diameter) and very flexible. Also there is a requirement for tactile sensitivity, since a surgeon performing minimally invasive surgery cannot use palpation as a means to derive tactile information regarding the condition of organs, tumours etc, as he is able to do during conventional surgery. A self-propelled endoscope [142] may also benefit from the addition of sensors to allow its

shape at any moment to be derived, to avoid unnecessary x rays or ultrasound scans to ascertain its position. Because of the limited space within an endoscope, the instrumentation necessary to give tactile feedback or information for shape reconstruction must be very small. The use of FBG sensors has many advantages in this application, since an optical fibre is very small (125μm diameter), and the use of wavelength multiplexing and the reflected spectrum means that only one fibre connection is needed for a number of sensors (see section 2.5.7). Also because FBG sensors are immune to electromagnetic interference they could be used in conjunction with MRI scanners where conventional sensors would not be usable.

3.2 Using a 4 grating FBG array for detecting shape changes of a steel strip.

It is often necessary in endoscopic applications to be able to reconstruct the shape of an endoscope as it is inserted into a body cavity. This can be done using x rays, ultrasound or an MRI scanner, but a much simpler system would to be to use strain readings from FBG sensors inside the endoscope itself to reconstruct the shape, and therefore the position of the endoscope. An experiment in which this was achieved was described in [102]. Twenty FBG sensors, two sensors at each of 10 points, were fixed to a flexible cylindrical substrate which was inserted into the biopsy channel of a colonoscope. One set of sensors was at 90degrees to the other around the axis of the substrate to give information in two orthogonal directions. The length of the colonoscope was 900mm. It was inserted into the colon of a live swine (anaesthetised) and shape reconstruction in 3 dimensions was possible, although the authors did not state with what accuracy.

The spacing necessary between sensors for shape reconstruction is a function of the flexibility of the substrate and the sensitivity required. The shape of the substrate can only be correctly inferred if the pattern of FBG strain readings is unique for each possible shape. If the inter-sensor spacing was too large relative to the flexibility of the

substrate, it would be possible for bends between two sensors in an endoscope to be undetected. An investigation was conducted to discover whether a particular arrangement of sensors on a substrate was suitable for shape reconstruction. Unlike the experiment with the colonoscope described above, this was done in 2 dimensions rather than 3.

3.2.1. Method

A 4 Bragg grating array was prepared and attached to a flexible steel strip 12mm wide, 30mm long and 0.38mm thick, using epoxy adhesive. The metal strip was clamped (fig 26) and bent to a variety of different shapes, and peak wavelength readings from each sensor were recorded for each shape.

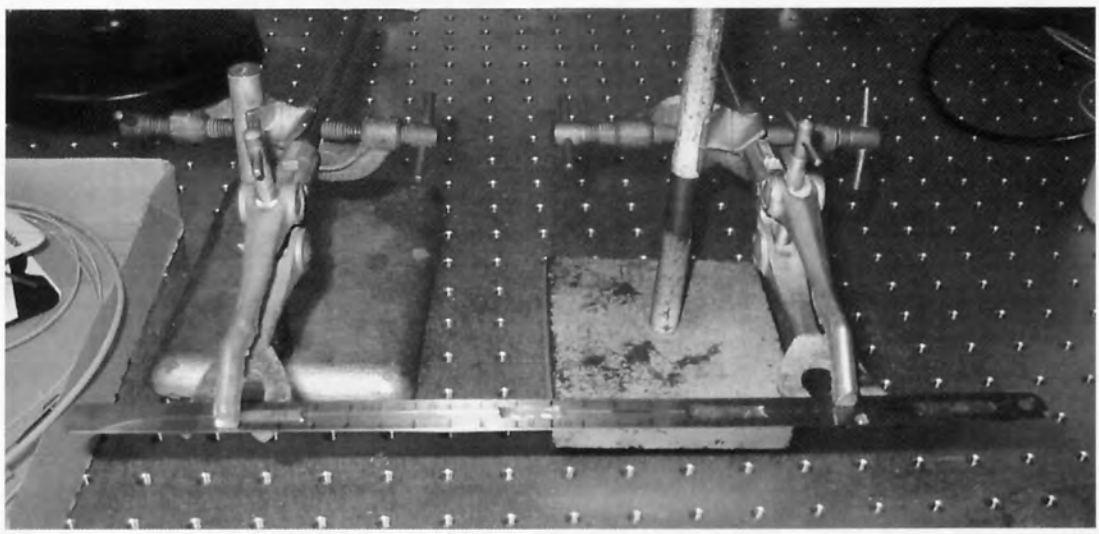

Fig. 26 Four-Grating array clamped

The following different profiles were investigated. Numbers 1 to 4 denote the approximate locations of the four gratings.

1. S-shaped, two different directions, various values of h

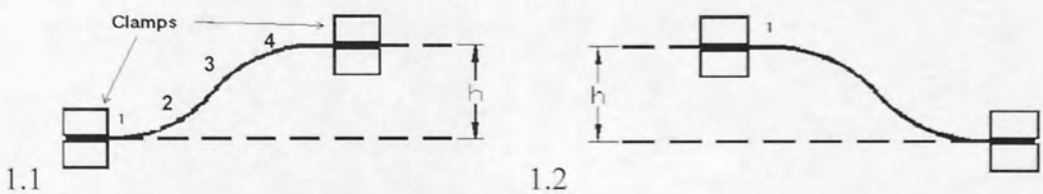

1.1 1.2

2. Double s-shaped, two different directions, various values of h.

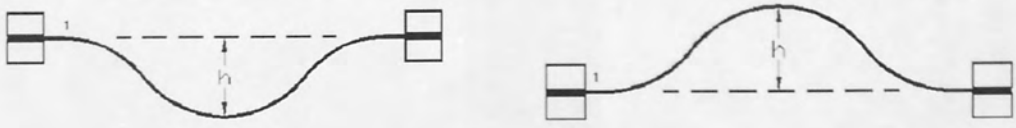

2.1 2.2

3. Simple curve, two different directions and various values of h

3.1 3.2

4. Single bend of fixed depth h but various values of bend location l:

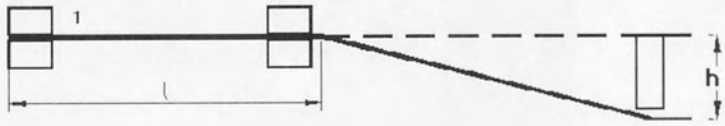

4.1

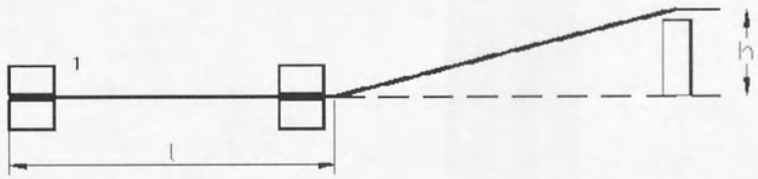

4.2

5. S-bend with curve

5.1 5.2

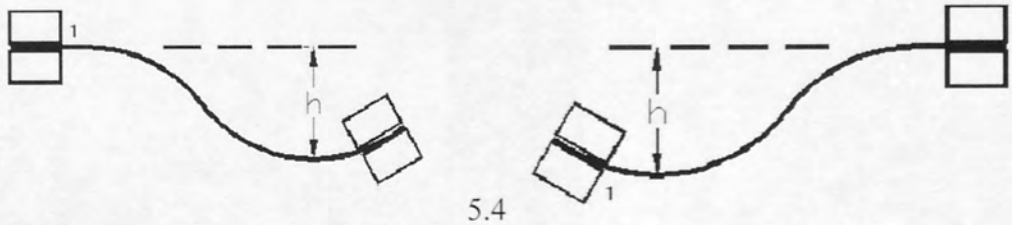

5.3 5.4

Fig. 27 Different shapes adopted by the metal strip for shape sensing experiment

3.2.2. Sensor interrogation:

Interrogation of the FBGs (fig. 28) was achieved by launching broadband light into the fibre. using an AFC Technologies BBS 1550 light source, (1520-1565nm, 25-60mW).The spectrum of the reflected light (fig. 29) was measured by an optical spectrum analyser (OSA) (Hewlett Packard 86142A) and this information was processed by a PC running Labview, which calculated the centre wavelengths of the four spectral peaks using the mean of half

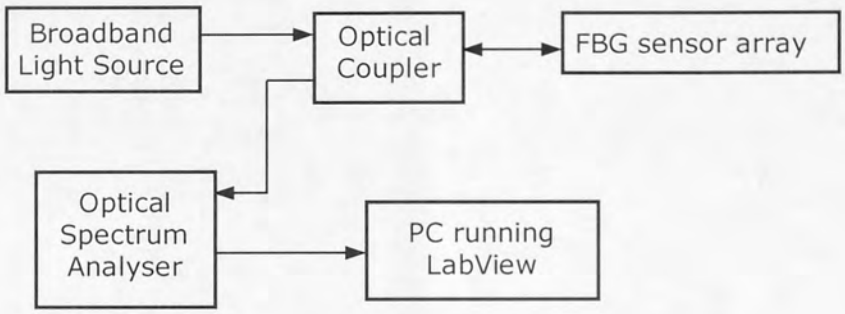

Fig. 28: Interrogation system for FBG sensors

maximum algorithm described earlier. (2.5.8.3).

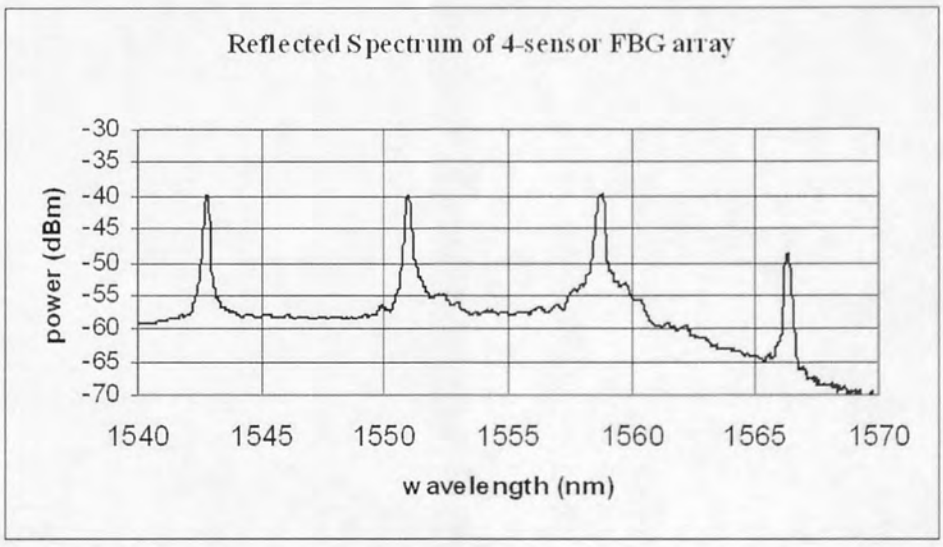

Fig. 29: Reflected spectrum of 4-sensor FBG array

These peak values were plotted against the variables (h or l) shown in the diagrams above. The graphs were substantially linear or had linear portions, and the slopes of

these graphs were calculated (to the nearest pm/mm) and appear in table 2 (for increasing h or l).

3.2.3 Results:

Profile type	Grating 1	Grating2	Grating3	Grating4
1.1	-8pm/mm	-1pm/mm	-1pm/mm	+13pm/mm
1.2	+11pm/mm	+5pm/mm	+4pm/mm	-9pm/mm
2.1	-40pm/mm	+36pm/mm	+44pm/mm	-22pm/mm
2.2	+50pm/mm	-18pm/mm	-39pm/mm	+33pm/mm
3.1	-31pm/mm	-13pm/mm	-11pm/mm	-27pm/mm
3.2	+21pm/mm	+40pm/mm	+40pm/mm	+24pm/mm
4.1	Little change	Little change, then +40pm/cm	Little change, then +50pm/cm	Little change, then –33pm/cm
4.2	-62.5pm/cm, then little change	Little change then -20pm/cm	Little change then -40pm/cm	Little change, then +115pm/cm
5.1	-29pm/mm	+13pm/mm	+25pm/cm	+75pm/mm
5.2	+27pm/mm	little change	-9pm/mm	-45pm/mm
5.3	+57pm/mm	+57pm/mm	+53pm/mm	-23pm/mm
5.4	-63pm/mm	-13pm/mm	-7pm/mm	+30pm/mm

TABLE 2 Wavelength changes for each sensor for different bend shapes

If changes below 6pm/mm are counted as zero, this table simplifies to:

	G1	G2	G3	G4
1.1	-	0	0	+
1.2	+	0	0	-
2.1	-	+	+	-
2.2	+	-	-	+
3.1	-	-	-	-
3.2	+	+	+	+
4.1 (bend near centre)	0	+	+	-
4.2 (bend near centre)	0	-	-	+
5.1	-	+	+	+
5.2	+	0	-	-
5.3	+	+	+	-
5.4	-	-	-	+

TABLE 3 Polarity of sensor wavelength change for each bend shape

It can be seen from table 3 that each shape produced a unique combination of positive, negative or zero values.

3.2.4 Interim Conclusions

The 4-grating array fixed to a stainless steel strip was able to detect a variety of different strip shapes, by producing a different combination of polarity of sensor wavelength changes for each different profile adopted by the strip. Twelve different shapes could be identified in this way. These results also show that for a substrate of a similar flexibility to the steel strip used in this experiment a sensor spacing of 70-80mm was sufficiently small to achieve correct shape detection for all the shapes investigated.

If this system were to be used as an insert to an endoscope, which bends in 3 dimensions, two sets of sensors would be required. These would need to be mounted at 90 degrees to each other as shown in fig 30. They could either be attached to a flexible rod and inserted into an instrument channel of an endoscope, or else embedded into the endoscope wall.

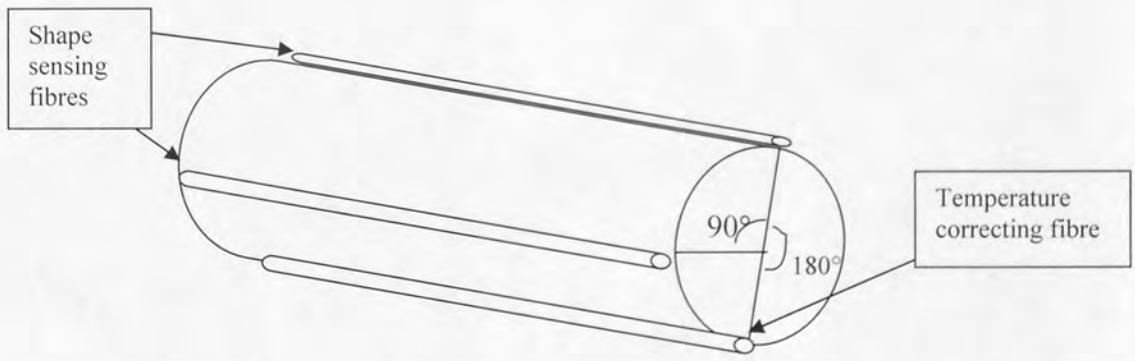

Fig 30 Suggested arrangement of fibre sensors for 3 dimensional shape detection

In order to correct for temperature changes, a third fibre, containing at least one sensor, could be attached to the endoscope, opposite one of the other two fibres as shown in fig.30. By comparing the wavelengths reflected by the sensors in the two fibres opposite

each other, any drift in wavelength which is common to both sensors will then be due to temperature, since a shape change would always result in wavelength changes of opposite signs in these two sensors. Providing there is no temperature gradient across the substrate between the three fibres, temperature correction can then be achieved. This approach also compensates for any axial strain, which, like temperature changes, would affect all three sensors equally.

3.3. Optimum length of Bragg grating for use in Endoscopy

3.3.1 Introduction

During the experiments described in 3.2 above it was noticeable that as the metal strip was bent the spectral peaks from the sensors sometimes became distorted (see fig. 31). Fig. 31 was recorded during the 'double s-bend' test, at a point when the deflection h exceeded 10mm (see section 3.2.1). At this point sensors 2 and 3 showed broadened spectral peaks, which became double peaks as the deflection increased still further. This is because the sensors were each 10mm long and experienced varying values of strain along their lengths.

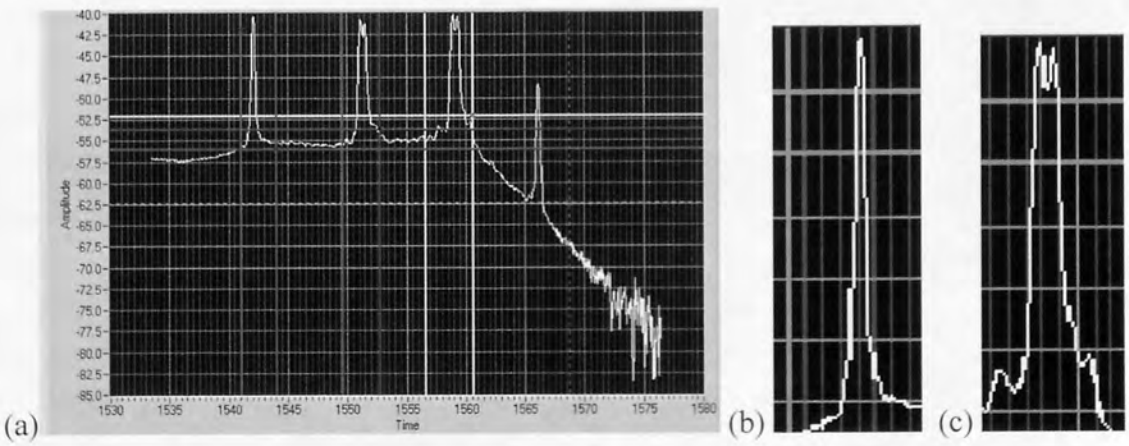

Fig. 31 (a)Typical Labview screen (b) undistorted and (c) distorted spectral peaks

The spectral broadening observed above could be modelled if the curvature at all points along the length of the grating (and thus the strain) was known, however the assumption

would have to be made that the strain was evenly and accurately transferred from the steel substrate to the grating. This was not necessarily the case for the sensors in this experiment. In practice the range of strain and thus the spectral broadening depends not only upon the strain distribution in the substrate along the length of the FBG but also upon the characteristics of the adhesive and the adhesion distribution along the length of the grating, which is very difficult to quantify.

The double peak shown in fig 31(c) would have been produced by a grating experiencing two distinctly different values of strain. The unstrained wavelength of this grating (shown in fig 29) is 1558.95nm, which is the wavelength of the first of the two spectral peaks (with the lower wavelength). The second spectral peak has been produced due to part of the grating experiencing a higher strain.

Fig. 32 Location of grating with double spectral peak on steel strip.

The gratings were attached to the upper surface of the steel strip, so it may be deduced that the grating was located at point P in fig. 32.

Distorted spectral peaks such as this are not desirable when FBG sensors are used to measure strain, because they can compromise the accuracy with which the wavelength of the spectral peaks are measured. Using a peak detection algorithm on a double spectral peak such as this would yield an average value of reflected wavelength which would not reflect accurately either of the actual strain values experienced by the grating.

3.3.2 Experiments

Clinical endoscopes are usually cylindrical and smaller in diameter than the metal strip used in the experiments above. Endoscopes with diameters as small as 2.7mm are being developed for use in spinal cord endoscopy [22]. They are also flexible in more directions than the metal strip used above, and sensors running along the core of such an endoscope would be very near to the neutral bending axis. A consequent requirement for a sensor is that it is capable of bending in any direction. FBG sensors are not inherently sensitive to bending and need to be bonded to a flexible substrate so that they monitor the strain in the substrate as it bends. In order to assess whether FBGs could be used in such an arrangement, a single FBG sensor, 15mm long, was fixed to the groove running along a length of twin figure-of-eight electrical PVC cable 30mm long (fig 33) using epoxy adhesive.

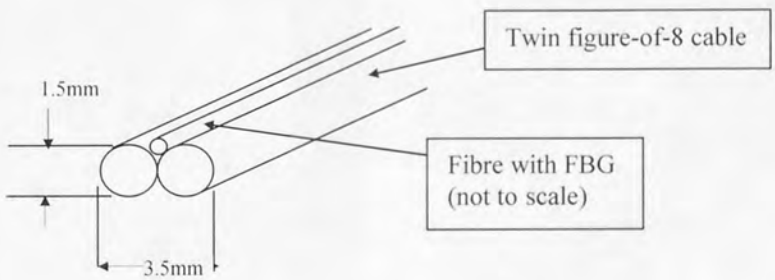

Fig. 33 Arrangement of FBG sensor on figure-of-8 cable, epoxy adhesive not shown

It was found that the variations in the central wavelength of the spectral peak as the cable was curved in any direction were large enough (up to 1nm) for use in this application (see fig 34). The spectral peak from the grating also experienced considerable broadening (fig. 35), so that the spectral width of this peak could also potentially be used as a measure of curvature in this application. These measurements were made at 12dB below the peak amplitude of the signal.

The spectral peak reflected by the grating became distorted as the wire was bent, partly the adhesive with which the grating was attached to the wire did not flex evenly, and also because the wire itself did not bend evenly due to the epoxy adhesive making the

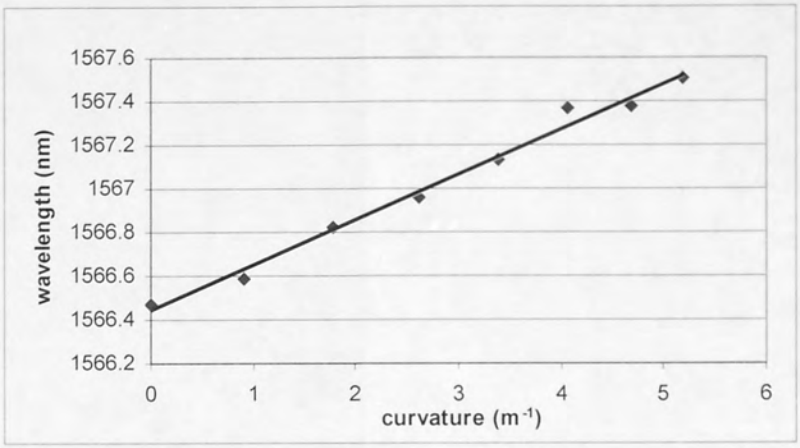

Fig. 34 Average wavelength of spectral peak at 12dB below peak versus radius of curvature

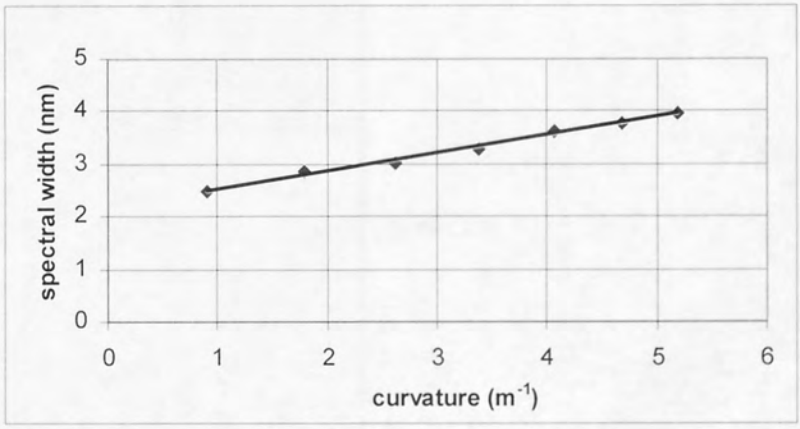

Fig. 35 Spectral width at 12dB below peak vs. radius of curvature

wire unevenly stiff. Spectra for FBGs of different lengths for different radii of curvature (compression and extension) are seen in figs 36-40.

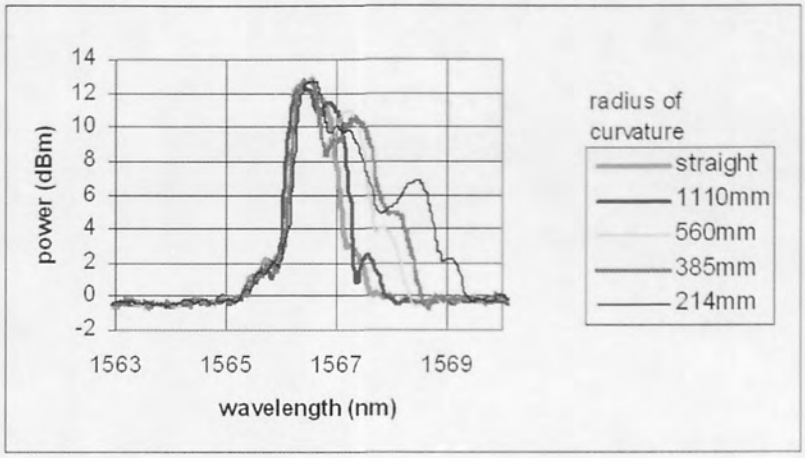

Fig. 36 Reflected spectra from 10mm FBG for different radii of curvature in extension (power levels normalised)

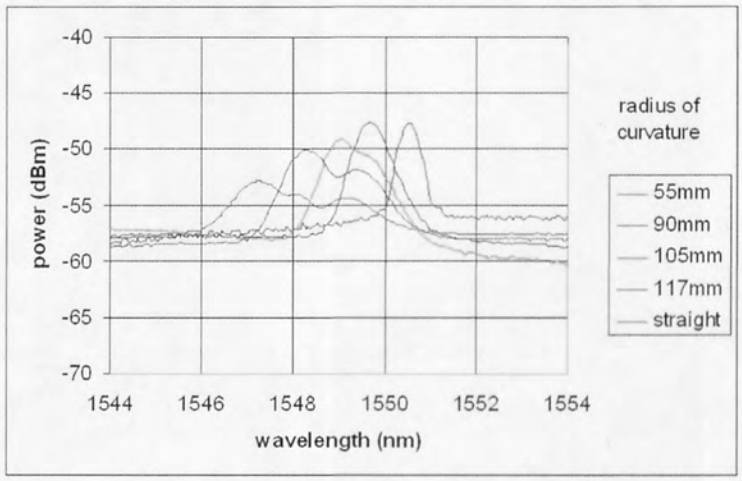

Fig. 37 Reflected spectra from a (different)10mm FBG for different radii of curvature in compression

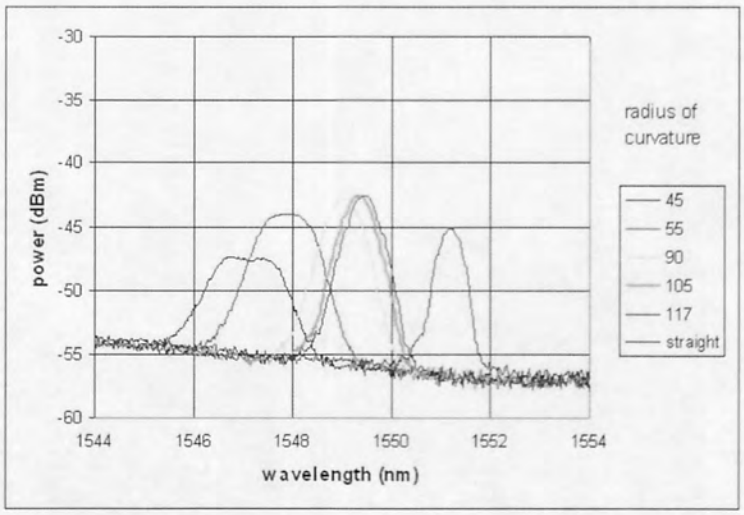

Fig. 38 Reflected spectra from 2.5mm FBG for different radii of curvature in compression

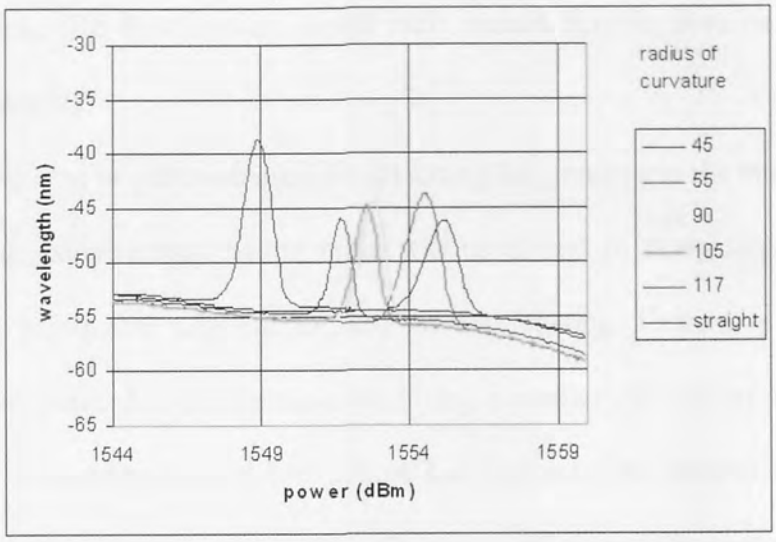

Fig. 39 Reflected spectra from 2.5mm FBG for different radii of curvature in compression

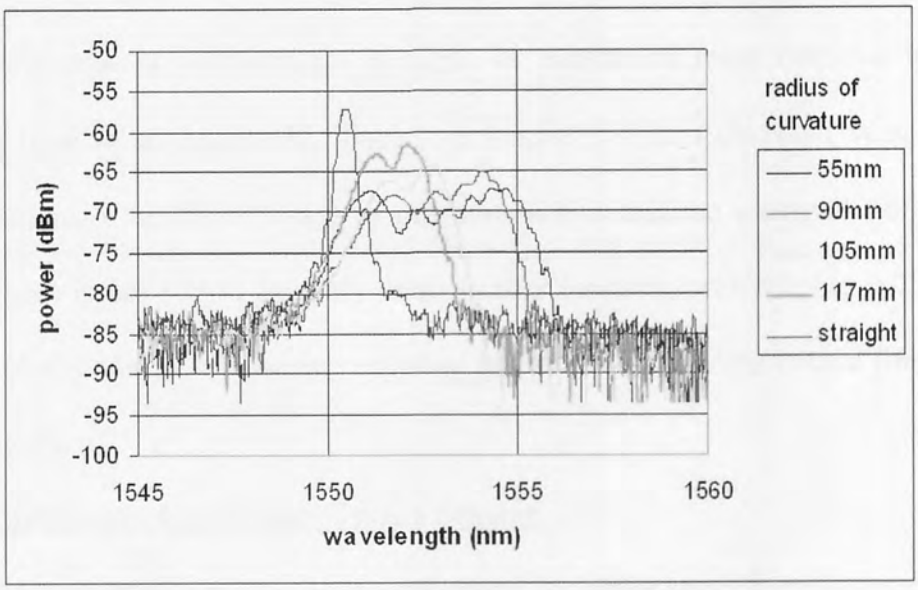

Fig.40 Reflected spectra from 7.5mm FBG for different radii of curvature in compression

3.3.3 Interim Conclusions

Curvature of the wire substrate produced considerable broadening of the FBG reflected spectrum. The predominant cause of spectral broadening in the experimental work was uneven strain distribution along the grating due to uneven bending of both the substrate and the adhesive. Considerable distortion in the spectral peak was experienced for 10mm (figs 36 and 37) and 7.5mm (fig 40) gratings, however this was much reduced for the 2.5mm grating (figs 38 and 39). It shows that FBG sensors for use in endoscopes,

particularly those that bend around small radii, would benefit from being short (less than 5mm in length).

The issue of the type of adhesive used for attaching the gratings to the endoscope is also raised. In these experiments araldite rapid was used, and in fairly large quantities in order to obtain reasonable adhesion to the PVC wire coating. There may be other types of adhesive better suited to this application. Using a smaller quantity of adhesive would almost certainly have improved this situation, but may not have been sufficiently robust to maintain contact between the optical fibre and the wire. The material used as a substrate to which the fibre would be attached within an endoscope would also affect the bonding process. Furthermore it might be considered more practical to use an uncoated fibre in an endoscope, since it is smaller (125μm uncoated versus 250μm coated) although the disadvantage of this approach is that the uncoated fibre is more brittle. These issues would certainly merit further research, preferably in collaboration with a manufacturer of endoscopes showing interest in introducing optical fibre sensors into its products.

3.4 FBG sensors in Distributive Tactile Sensing

One of the most commonly used types of sensor for tactile sensing applications, and for distributive tactile sensing in particular, is the electrical resistance strain gauge. In order to determine the suitability of FBG sensors for use in a distributive tactile sensing regime, we conducted a direct comparison between FBG sensors and electrical strain gauges. This comparison was performed on a one-dimensional system, which was developed as a step towards the ultimate aim of providing an endoscope with tactile sensitivity [49].

3.4.1 Comparison with electrical resistance strain gauges

3.4.1.1 Sensor Locations

The locations of these sensors had previously been optimised using a genetic algorithm which selected the sensor positions which would give the maximum values of the first four principal components of the sensor outputs [46]. The sensor locations had been optimised for displacement sensors using a beam of length 400mm which was simply supported at both ends (fig. 41). The distance between the upper surface of the sensors and the lower surface of the beam was limited to a range of between 1 and 4mm, which was the operating range of the sensors

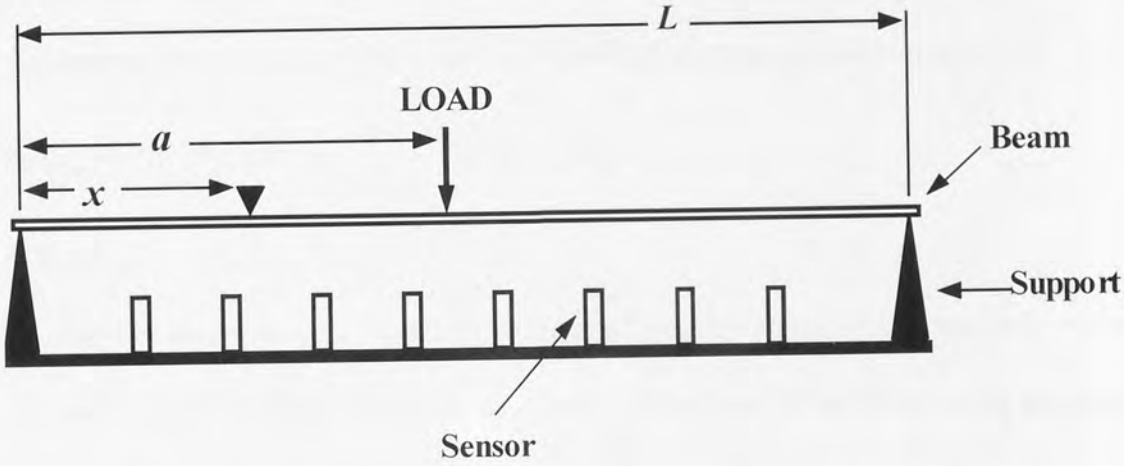

Fig. 41 Experimental arrangement used to optimise sensor locations (L=400mm).

The deflection y at position x in response to an applied load W at position a on a simply supported beam of length L is given by [143]

$$y = \frac{W}{6EI}\left[\frac{(2L-a)(a-L)ax + (L-a)x^3}{L} - \left((x-a)^3\right)\right] \qquad 0 \le x \le a$$

where E and I are Young's modulus and second moment of area of the beam, respectively. The following assumptions apply: (a) the beam is straight and of uniform cross section (b) the beam is constructed from homogeneous material (c) the load applied will not exceed the elastic limit of the material (d) the deflections induced by the load are small compared to the length.

So a point load at the centre of the beam gives a deflection pattern as shown in fig 42:

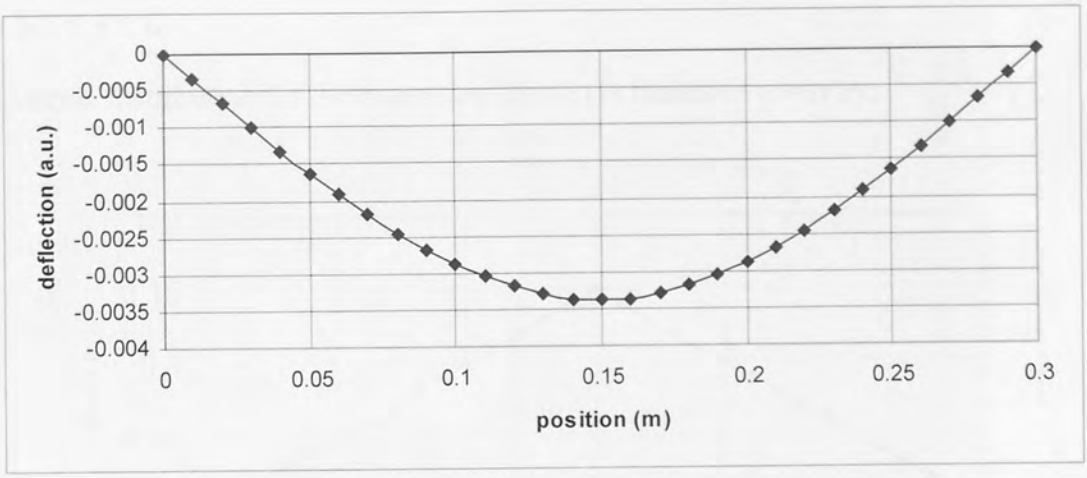

Fig. 42 Deflection v distance along a beam simply supported at both ends with a point load at its centre

To compare the deflection pattern in fig. 42 with the strain distribution along the same beam, we use the identity $\frac{M}{I} = \frac{\sigma}{t} = \frac{E}{R}$, [144] _____ (2)

Where:

M= bending moment, I= second moment of area, σ= stress, t=distance from central axis (= half thickness of beam), E= Young's Modulus, R= bending radius to central axis of beam.

The bending moment for a beam that is simply supported at both ends, is given by [143]:

$M(x) = \frac{-Px}{2}$ for $0 \leq x \leq L/2$, and $M(x) = -\frac{P(L-x)}{2}$ for $L/2 \leq x \leq L$

The second moment of area for a rectangular beam is given by, $I = (bt^3)/12$

Where b=width and t=thickness of the beam.

We see that both I and t are constant regardless of the position of the load on the beam, so from equation (2), strain, σ is directly proportional to M, so:

$\sigma \propto Wx$

for $0 \leq x \leq L/2$

and $\sigma \propto W(L-x)$ [143 p180-181]

for $L/2 \leq x \leq L$

The strain distribution for the beam (see fig. 43) is therefore given by:

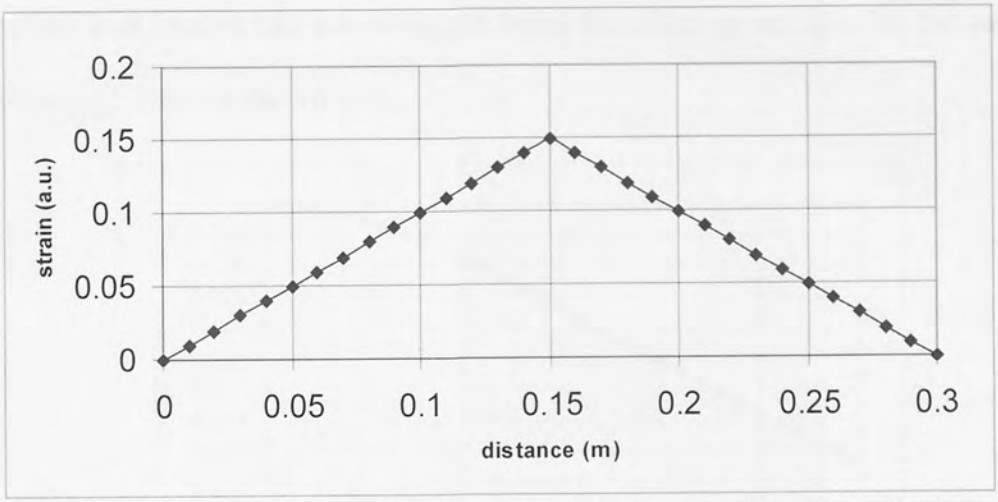

Fig. 43 Strain v distance along a beam simply supported at both ends with a point load at its centre

It can be seen from the two graphs above that the distributions of strain and deflection are different. Therefore it is not possible to say that the optimised positions for the sensors obtained using deflection measurements are also optimal for an arrangement of strain sensors.

Differences are also found in the case of a cantilever beam as shown in fig 44

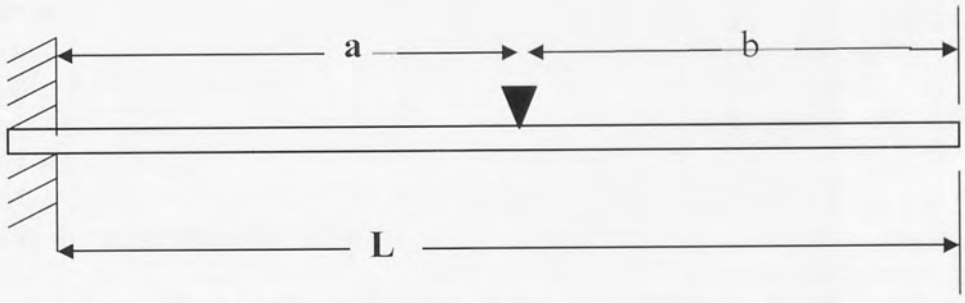

Fig. 44 Cantilever beam with load at distance a from the clamped end

The deflection y of the beam at a point x along the beam due to a point load W at distance a from the clamped end is given by [143 p 184-5]:

$$y = \frac{Wx^2(3a - x)}{6EI} \quad \text{for } 0 \leq x \leq a$$

$$\text{and } y = \frac{Wa^2(3x - a)}{6EI} \quad \text{for } a \leq x \leq L$$

Where E and I are the Young's modulus of the beam material and the second moment of area respectively.

For a point load located half way along the beam this gives the relationship between deflection and distance shown in fig. 45.

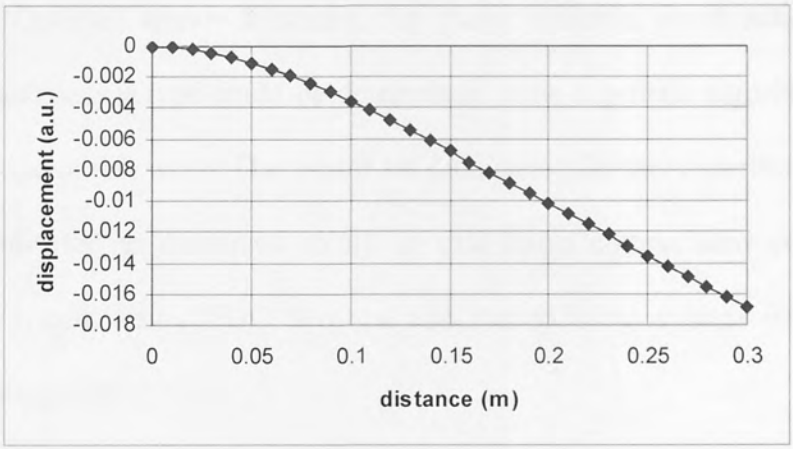

Fig. 45 Displacement v distance for a cantilever beam with a load as shown in Fig. 44

The displacement pattern is a curve until the position of the load is reached, after which the displacement becomes a linear function of distance.

Using the same principles as for the simply supported beam the strain distribution is given by

$\sigma \propto Wx$ for $0 \leq x \leq a$ and

$\sigma = 0$ for $a \leq x \leq L$

This is shown graphically in fig 46

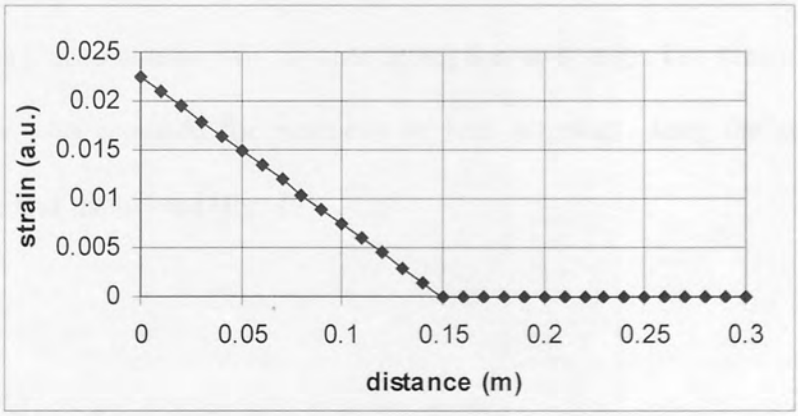

Fig 46 Strain v distance for a cantilever beam with a load as shown in Fig. 44

The implication of the relationships shown above is that although the sensor locations had been optimised for displacement sensors monitoring a beam simply supported at both ends, these sensor locations were unlikely to have been optimal for either strain sensors in a similar beam arrangement or for either type of sensor in a cantilever arrangement. Optimal sensor locations for these different combinations of beam arrangement and sensor type could be determined using a genetic algorithm but this is outside the scope of this work. The sensor locations used for this experiment were those previously optimised as described solely so that direct comparisons could be made between the system using FBG sensors and the existing system using electrical resistance strain gauges.

3.4.1.2 Experimental arrangement

Two identical steel strips were prepared, with sensor locations as shown in fig. 47. The FBG sensors were multiplexed, having four different reflective wavelengths so that they were contained within one fibre with a single connection (fig. 48a). A second identical steel strip had four resistive strain gauges fitted to it in the same positions, having 8 connecting wires (fig. 48b). Each steel strip was clamped at one end in a cantilever arrangement. (fig. 49)

The grating array was interrogated as described previously (3.2.2). The resistive strain gauges were interrogated using a D.C. bridge circuit and electronic amplifiers. A load of mass 2.4g was placed at a known distance along the steel strip. The sensor outputs were recorded. This was repeated for positions at 1cm intervals along the strip and for a single, double and triple load (fig. 49).

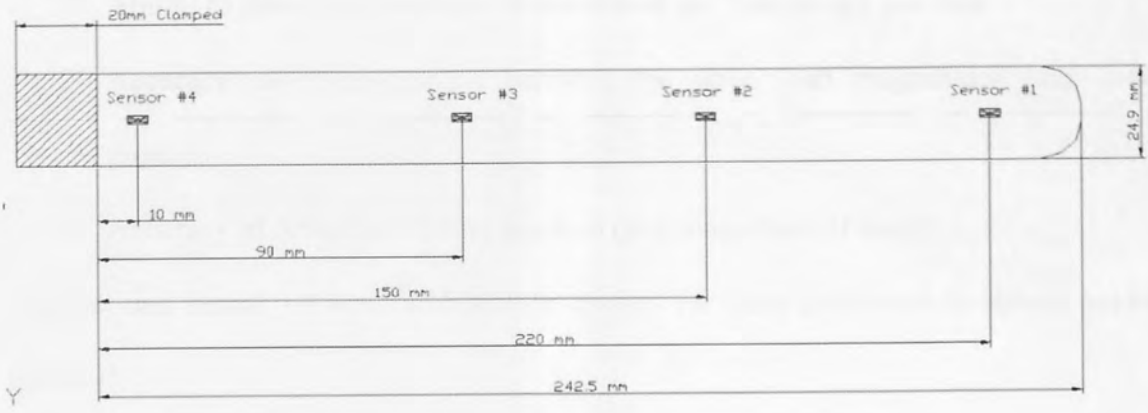

Fig. 47: Sensor layout on 1-D tactile sensing strip. (0.38mm thick)

Fig. 48a: Steel strip with FBG sensors.

Figure 48b: Steel strip with electrical resistance strain gauges

Multiple sets of sensor data were recorded for each load position and each load size (a total of 351 sets). The sensor output data were randomly allocated into three sets, for training, validation and testing respectively. This was repeated for the second steel strip so that the performance of the systems using the two different sensor types could be compared.

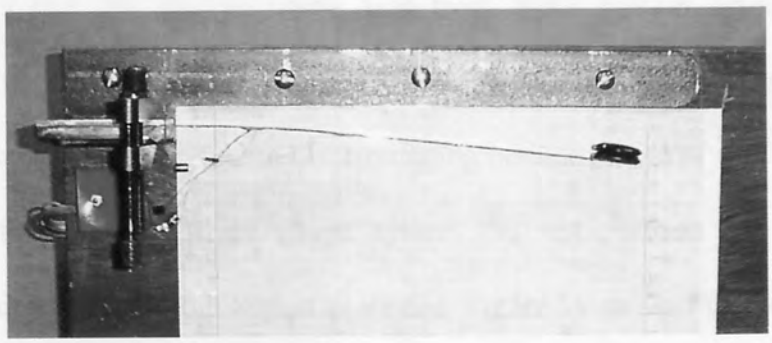

Fig. 49: Clamped steel strip with double load on one end

The performance of the two sensor types was assessed in 3 ways.

1. Ability to detect the presence or absence of any load at any position.
2. Accuracy of distinguishing between the three load magnitudes (any load position).
3. Accuracy of detection of load position (any magnitude of load).

The optimal neural network architecture chosen for each parameter is shown below (table 4).

Type Of Neural Network	Type of Output	Optimal No. Hidden Nodes
Linear (4 Inputs)	Position (FBG)	15
Logistic (4 Inputs)	Contact Present (FBG)	45
Softmax (4 Inputs)	Load Magnitude (FBG)	10
Linear (4 Inputs)	Position (Strain)	5
Logistic (4 Inputs)	Contact Present (Strain)	60
Softmax (4 Inputs)	Load Magnitude (Strain)	15

TABLE 4 – Neural Network architectures chosen for one-dimensional system

3.4.1.3 Results

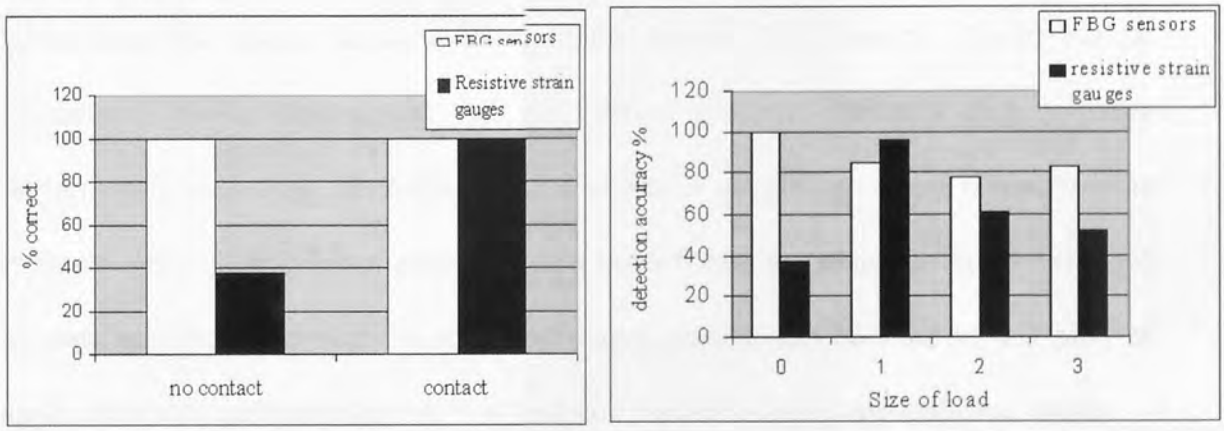

Fig. 50: Comparisons of (a) contact and (b) load magnitude detection

Fig. 50 shows that the system using data from FBG sensors achieved a higher percentage accuracy than the system using data from resistive strain gauges in both contact/non contact detection and in discriminating between 3 out of 4 of the load sizes. In particular the resistive strain gauge system did not perform well in unloaded conditions, which it tended to interpret as loaded. Figure 51 shows that the system using FBG sensors was able to detect the position of the load to within 2cm of its actual position more than 50% of the time. The system using resistive strain gauges achieved

less than 40% in the same test. The rms error for the FBG sensors was actually slightly larger because of a few highly inaccurate results (6.1cm, vs. 4.5cm for the resistive strain gauges).

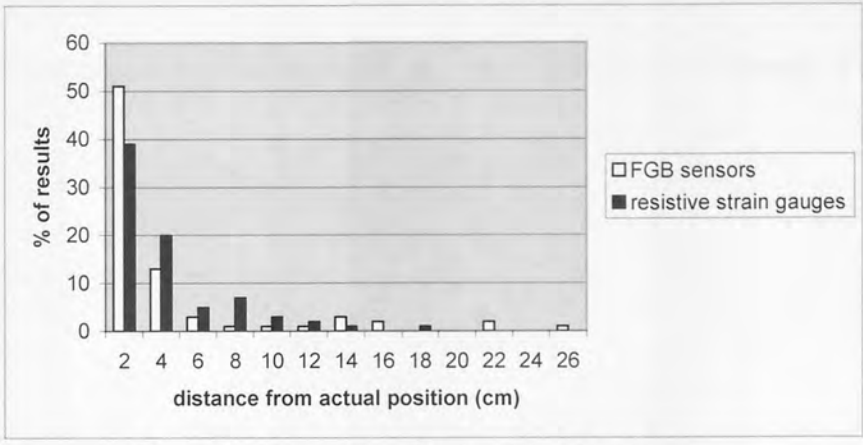

Figure 51: Comparison of load position detection

3.4.1.4 Conclusions

Although these results show that the system using the FBG sensors generally performed better than the system using resistive strain gauges, this outcome should not be generalised into an assumption that FBG based systems inherently display better performance than those containing electrical strain gauges. A direct comparison is difficult, since the sources of noise and drift in each case are rather different. What we do conclude from this study is that FBG based sensors can be used in this kind of application with performance that is at least comparable to more conventional sensors.

3.5 Summary

In this chapter we have seen that FBG sensors attached to a flexible substrate are suitable for use in a 1-D distributive tactile sensing system such as may be used to provide an endoscope with tactile sensitivity. This arrangement would also allow the shape of an endoscope to be reconstructed if necessary. The length of each FBG should be short, preferably 5mm or less, in order that the shape of the reflected spectrum does not become distorted where the bend in the endoscope are tight. We have compared the

use of FBG sensors with electrical resistance strain gauges in an experimental arrangement and found their performance is as good or better than the strain gauges. This work has shown that FBG sensors would be a good choice for using to instrument and endoscope, particularly since they have added advantages for this application since they are small, electrically neutral and need only one connection for a group of sensors.

Chapter 4 - Two-Dimensional Tactile Sensing Surface

4.1 Introduction

This chapter presents a two dimensional tactile sensing surface using FBG sensors. The surface was used to identify the position and shape of a contacting load, and also to identify other load characteristics. A similar surface has been the subject of work by Pensiri Tongpadungrod [47]. The surface she used was the same size as the one used here, but used infrared displacement (proximity) sensors mounted beneath the surface (see fig. 52) rather than optical fibre sensors. This enables direct comparison of the results from the systems incorporating the two different types of sensors. This chapter also includes work identifying the difficulties encountered during this study, solutions to some of these difficulties, and describes a second, larger sensing surface with possible applications in podiatry.

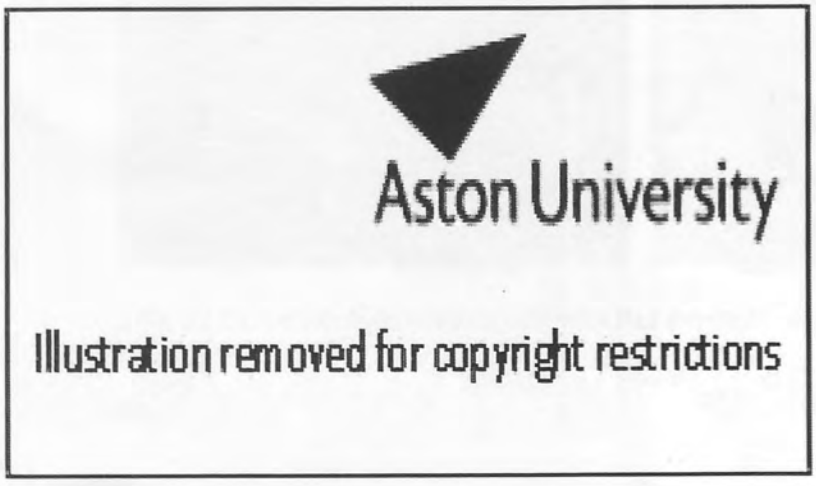

4.2 Construction of Surface

The FBG sensing surface comprised a plate, 430mm x 330mm, which was supported by

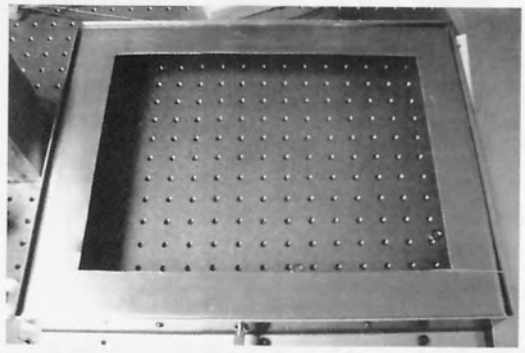

Fig. 53 Supporting structure for tactile surface

framework (fig. 53) which allowed the plate to deflect downwards when a load was applied, and retained the plate within the framework. The plate was therefore 'simply supported' from an analytical viewpoint.

4.3 Analysis

The displacement ω of any point *x,y* on a simply supported surface (fig. 54) in response to a concentrated load P at point A is given by the formula [145]:

$$\omega = \frac{Pa^2}{\pi^3 D} \sum_{m=1}^{\infty} \left(1 + \beta_m \coth \beta_m - \frac{\beta_m y_1}{b} \coth \frac{\beta_m y_1}{b} - \frac{\beta_m \eta}{b} \coth \frac{\beta_m \eta}{b} \right)$$

$$\times \frac{\sinh \frac{\beta_m \eta}{b} \sinh \frac{\beta_m y_1}{b} \sin \frac{m\pi\xi}{a} \sin \frac{m\pi x}{a}}{m^3 \sinh \beta_m}$$

for $y \geq \eta$ $\quad \beta_m = \frac{m\pi b}{a}, \quad y_1 = b - y$

for $y < \eta$ $\quad y_1$ is replaced by y and η by $\eta_1 = b - \eta$

$$D = \frac{Et^3}{12(1-v^2)}$$

where E is the Young's Modulus, t is the surface thickness and v is the Poisson's ratio.

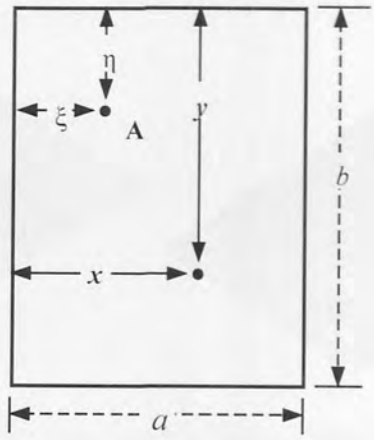

Fig. 54 Diagram for derivation of plate deflection under a concentrated load. [145]

Using this equation to plot the displacement in response to a load of 1.5N at x=70mm, y=110mm gives the pattern shown in fig 55.

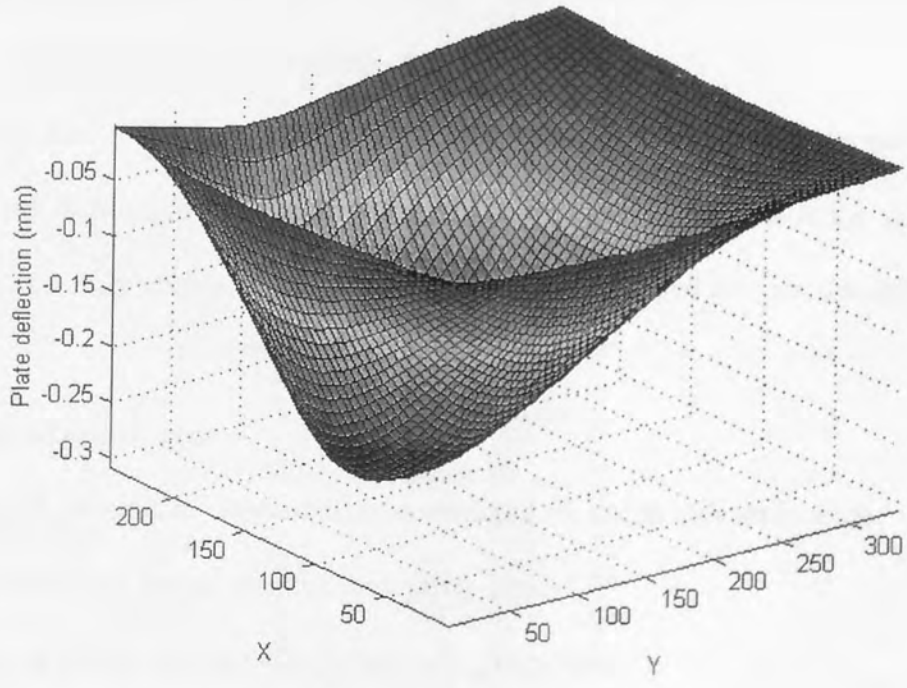

Fig. 55 An example of simulated surface deflection [47] (used with permission)

The analysis of deflection for the plate was used to optimise the sensor locations in the design shown in section 4.1. However fibre Bragg gratings measure strain, which is much more complex to deal with analytically, not least because strain is a vector quantity. The normal way of analysing strain is to use finite element analysis and resolve the strain into two orthogonal components (see fig. 56).

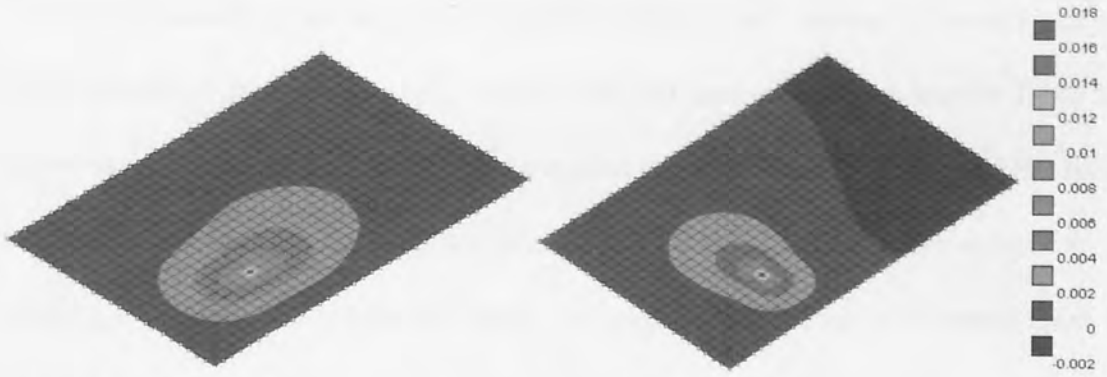

Fig. 56 Strain patterns (N/mm^2) for same plate size (240 x 340mm) and load conditions as in fig. 55, resolved into two directions, y (left) and x (right). Analysis performed using SAM-LEAP5 software.

While the patterns seen in fig. 56 are similar to the displacement pattern, they are not identical, indeed it is interesting to note that the darker region furthest from the load in the x plot indicates negative strain. This was found to be the case experimentally, and does not correspond to a negative deflection in fig. 55.

The optimal sensor locations for the displacement sensors were found to be very close to the evenly distributed case, so for the initial experimental surface here the sensors were spaced evenly (except in the case of horizontally arranged sensors, see section 4.6).

4.4 Choice of sensor type

Two types of optical fibre sensors were considered for use in this application.

(1) Fibre Bragg grating sensors measuring strain

(2) Long period grating sensors measuring curvature.

Type of sensor	Sensitivity quoted
Corrugated LPG [146]	18.5nm m^{-1}
LPG written with CO_2 pulses [147]	7.7nm m^{-1}
LPG in D-shaped fibre [148]	12.6nm m^{-1}
LPG in eccentric core fibre [149]	10nm m^{-1}
Pair of LPGs [150]	18.2nm m^{-1}

TABLE 5 bend sensitivities of different types of LPG sensors

LPGs are inherently sensitive to curvature but FBGs are not. Several different kinds of LPGs have been used as curvature sensors [146-150] and sensitivities seen in Table 5 below have been measured. Although the central reflected wavelength of an FBG is not inherently sensitive to bending, if it is bonded to a substrate which is then subject to bending, the sensor will experience strain, the magnitude of which will depend upon the degree of curvature of the substrate.

4.4.1 Calculation of sensitivity of FBG when fixed to a plate which is subject to bending

Suppose an FBG of length l is mounted directly onto a surface of thickness t which is then curved to a radius of r. (fig 57)

Unstrained length of FBG=l

Strained length of FBG = l_s

$$\frac{l}{2\pi r} = \frac{l_s}{2\pi(r + t/2 + t_f/2)}$$

where t_f it the diameter of the fibre.

$$\text{so } l_s = \frac{2\pi l(r + t/2 + t_f/2)}{2\pi r}$$

$$l_s = \frac{l(r + t/2 + t_f/2)}{r}$$

The strain measured by the FBG is defined as extension/original length

$$\text{Strain} = \frac{l_s - l}{l}$$

$$= \frac{\frac{l(r + t/2 + t_f/2)}{r} - l}{l} = \frac{t + t_f}{2r} \qquad (1)$$

So the response of the FBG is dependent not only on the curvature but on the distance of the fibre core from the neutral bending axis of the material.

For a material thickness of 1mm (for example) and deflection of 1mm at the centre of the smart surface, which has a distance between supports of 340mm (see fig 71), assuming the deflection causes the shape of the plate to describe an arc of a circle, we can construct the following geometry:

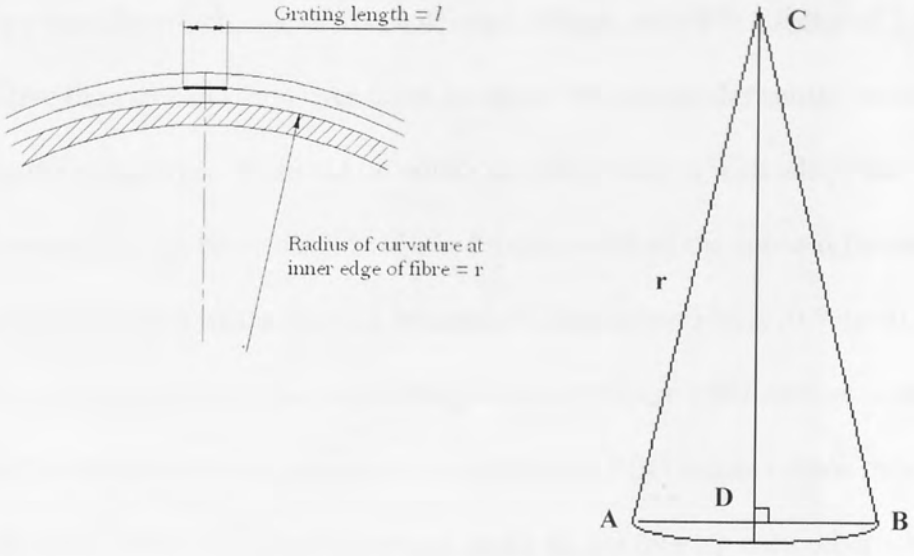

Fig. 57 Geometry of FBG sensor on curved plate

The arc AB represents the curved plate (between the supports) which is assumed to be of a constant curvature, while the line AB represents the undeformed plate. C represents the centre of curvature and CD is a line through C which is the perpendicular bisector of AB.

Using the triangle ADC, $r^2=AD^2+DC^2$ (Pythagoras)

AD=170mm, DC= r-1mm

$r^2=170^2+(r-1)^2$

$r^2=170^2+(r^2-2r+1)$

$$r=\frac{170^2+1}{2}=14.45\text{m}$$

using equation (1) above with a standard uncoated fibre diameter of 125μm gives

$$strain=\frac{1mm+0.125mm}{14.45m\times 2}=39\mu\varepsilon$$

For silica fibre, the wavelength–strain sensitivity at 1550nm has been measured as 1.15 pm/με, [61] so the expected response from an FBG would be a 45pm wavelength change.

A typical value of curvature sensitivity for LPGs from Table 5 is 10nm/m^{-1}, which would give a wavelength change of 10/14.45nm = 692pm, which is a factor of 15.4 more sensitive than an FBG, however there are other factors besides sensitivity involved in choosing the sensor type. It should be noted that the precision with which the resonant wavelength can be measured is linked to the width of the spectral feature, and LPGs tend to have much wider spectral features (5-20nm) than FBGs (0.5-1nm). Practically it was considered to be more straightforward to use FBG sensors in this application (a) because it is much easier to multiplex the FBG sensors when they are used in reflection, since the reflected spectral peaks do not overlap each other when the gratings are written at different wavelengths and (2) because LPG sensors written in standard optical fibre are much more sensitive to temperature than FBG sensors. LPGs fabricated in standard telecommunications optical fibre exhibit temperature sensitivities in the range 30pm / °C to 100pm/°C[73].This is up to an order of magnitude larger than the sensitivity of FBG sensors (13 pm/deg C [61]). LPGs written in Photonic Crystal fibre have much lower temperature co-efficients, typically a few pm/°C [176], but this type of fibre is currently expensive and problematic to use. Also LPG sensors would require more connections since they are used in transmission rather than in reflection (18 connections instead of one for 9 sensors).

4.5 Sensor fabrication and interrogation

Nine Fibre Bragg grating sensors, each with a reflectivity of 15dB and bandwidth of approximately 1nm at half maximum were mounted onto the underside of a PMMA plate. Each sensor was 10mm long, written in hydrogenated standard SMF-28 fibre

using a 244nm laser and a phase mask. The phase mask used allowed gratings at 5 different wavelengths (1535.9nm, 1543.7nm, 1551.7nm, 1559.6nm and 1567.6nm) to be written. Gratings at wavelengths other than these were achieved by stretching the fibre during exposure so that the resulting unstretched sensor had a lower reflective wavelength than would otherwise have been achieved. Interrogation of FBGs (fig. 58) was achieved by launching broadband light into the fibre using an AFC Technologies BBS 1550 lightsource, (1520-1565nm, 25-60mW). The spectrum of the reflected light (fig. 59) was measured by an Optical Spectrum Analyser (OSA) (Hewlett Packard 86142A, resolution bandwidth 0.2nm) and this information was processed by a PC running Labview, which calculated the wavelengths of the spectral peaks.

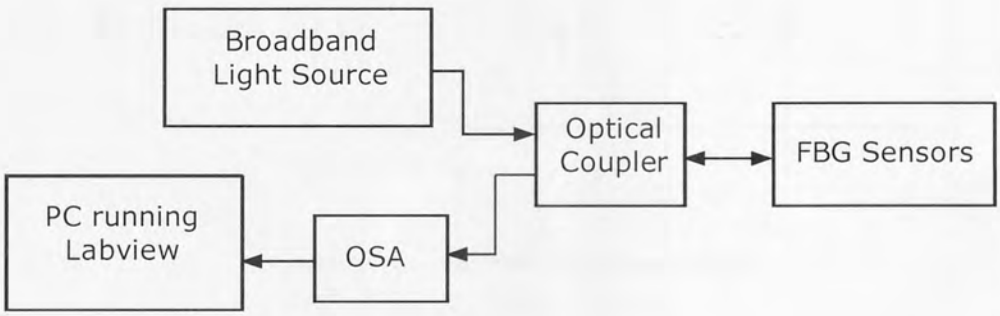

Fig. 58. Interrogation system for FBG sensors.

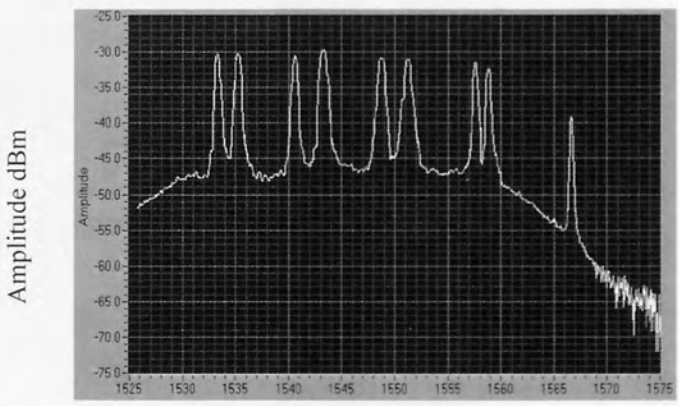

Fig. 59 Reflected spectrum of 9-sensor array.

4.6 Sensor layout

3 different layouts were assessed with vertically (fig. 60), horizontally (fig. 61) and radially (fig. 62) arranged sensors respectively. The sensors were mounted onto the plate with epoxy adhesive (fig. 64).

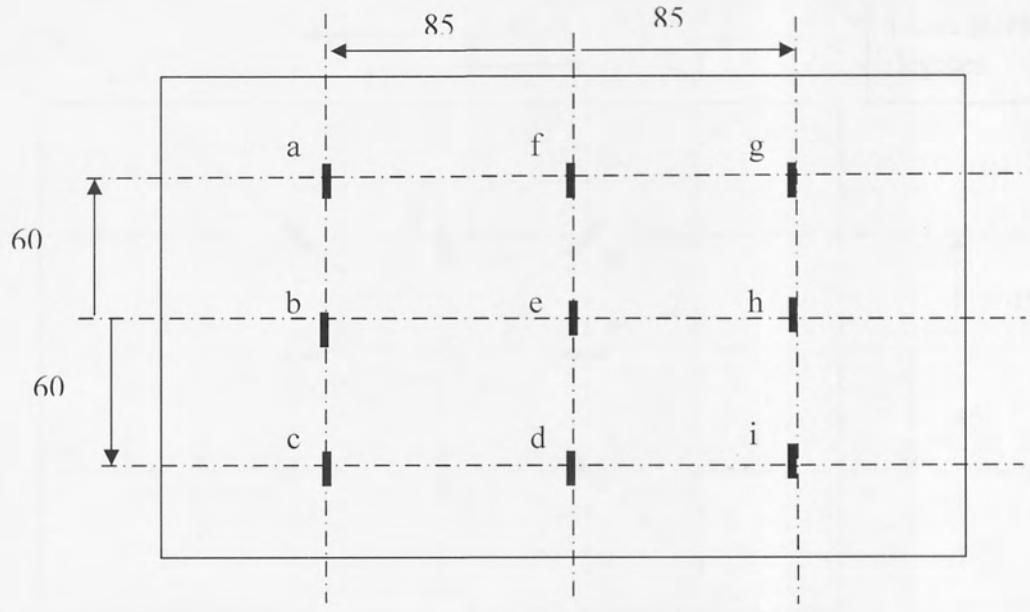

Fig. 60. Layout with vertically arranged sensors

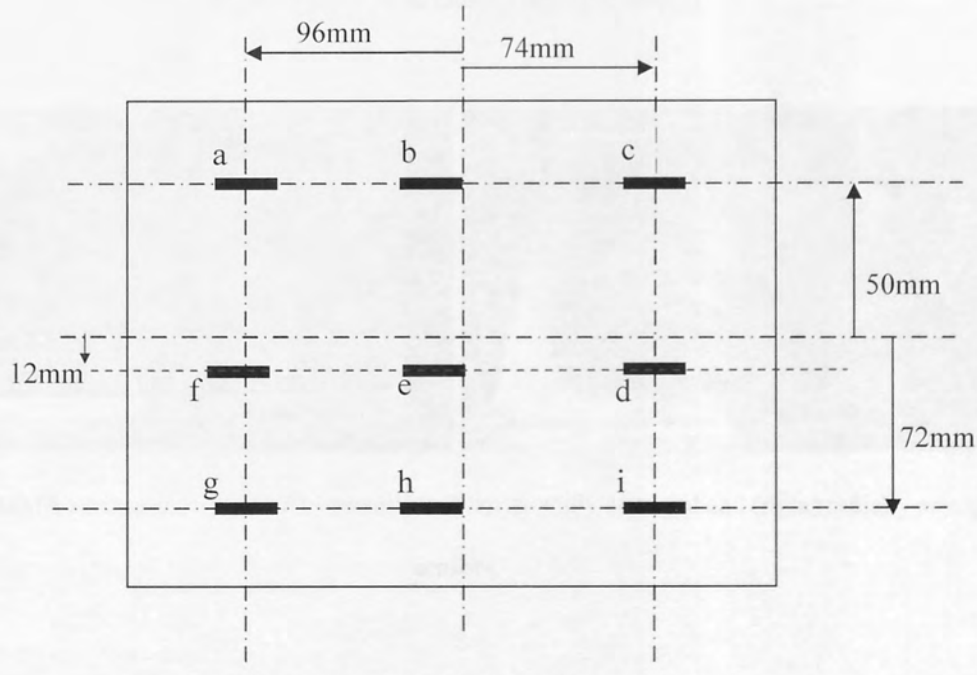

Fig. 61 Layout with horizontally arranged sensors

The slightly asymmetric arrangement in fig. 61 was necessary because horizontally and vertically arranged sensors were mounted on a single surface (see fig 63) and sensors cannot physically intersect, so the vertically arranged sensors were evenly spaced on the surface and the horizontally arranged ones were fitted around them.

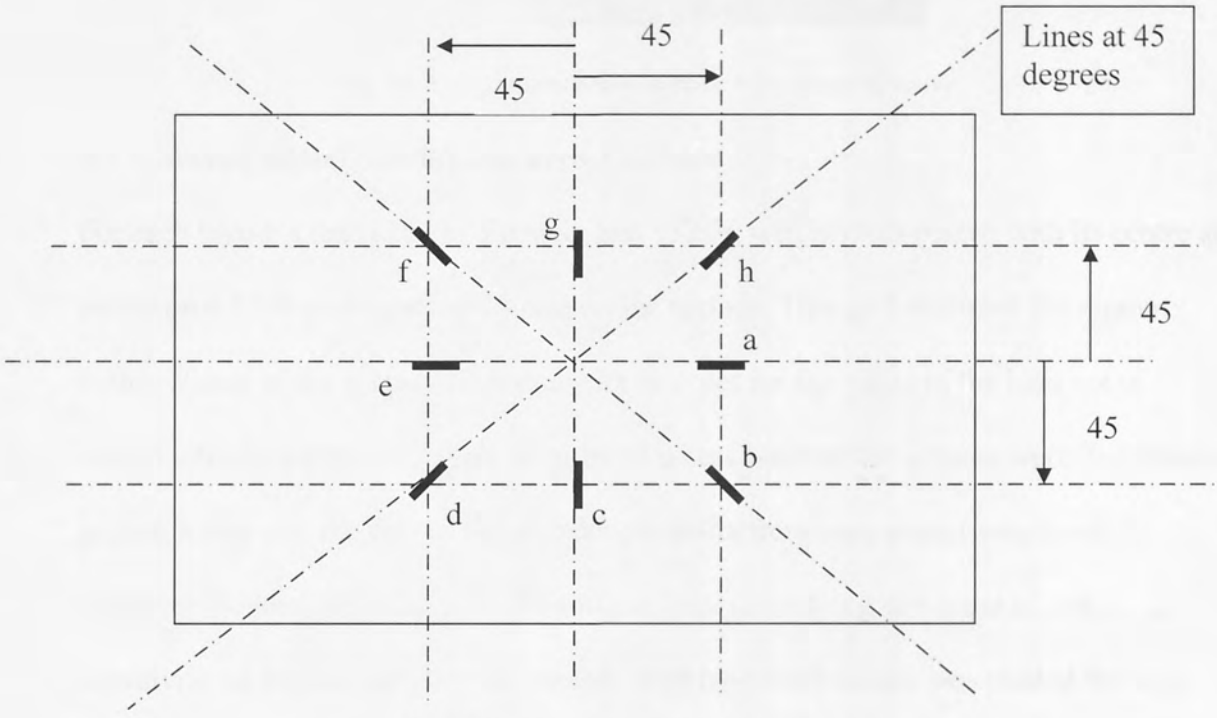

Fig 62. Layout with radially arranged sensors

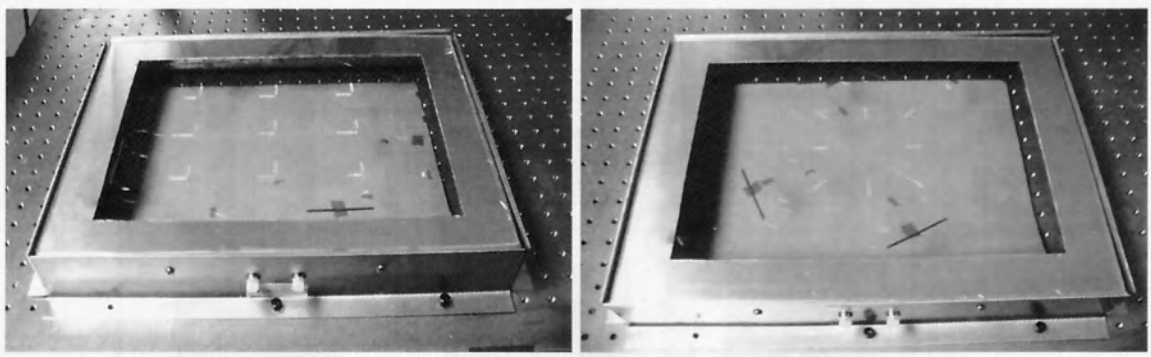

Fig.63 PMMA surface showing (left) vertically and horizontally arranged and (right) radially arranged sensors.

Fig. 64 A sensor attached to surface with epoxy adhesive.

4.7 Assessing signal distribution across surface

For each layout a load (38mm diameter and 132.7g weight) was placed with its centre at points on a 13x9 grid (spacing 20mm) on the surface. This grid excluded the region within 20mm of the supporting framework in order for the edges of the load not to extend into the supported region. In order to assess whether the sensors were distributed in such a way that the sum of the wavelength shifts from each sensor was equal wherever the load was placed on the surface (thus identifying any areas of low sensitivity on the surface), the wavelength shift from each sensor was plotted for each load position on the 13x9 grid. The total wavelength shift from all sensors was also plotted on the same grid. This was done for each sensor layout.

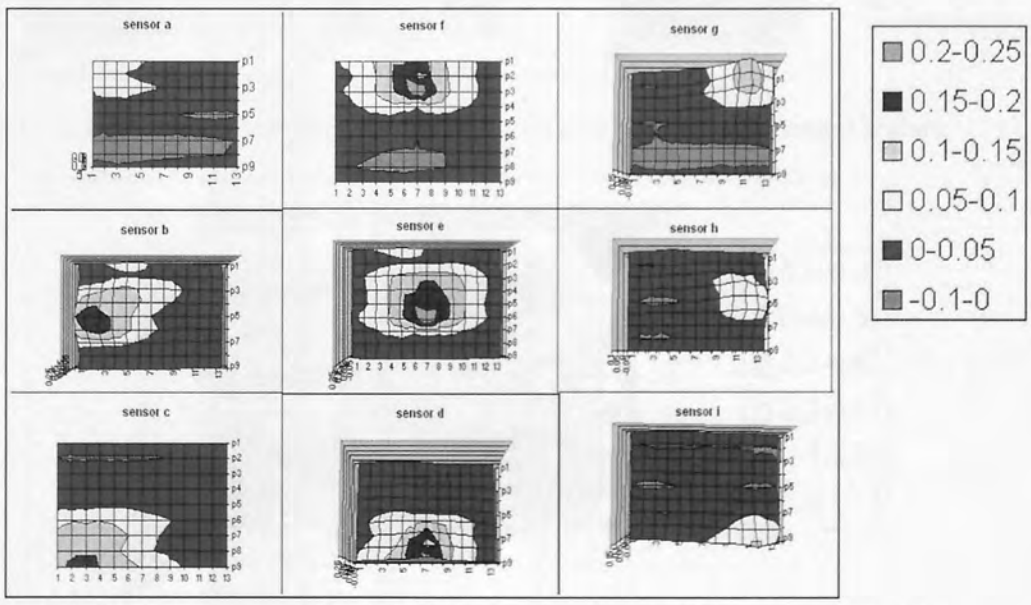

Fig. 65 Individual sensor wavelength shifts (nm) v location, vertically arranged sensors.

The results can be seen in figs 65 and 66 (vertical sensors), figs 67 and 68 (horizontal sensors) and figs 69 and 70 (radial sensors).

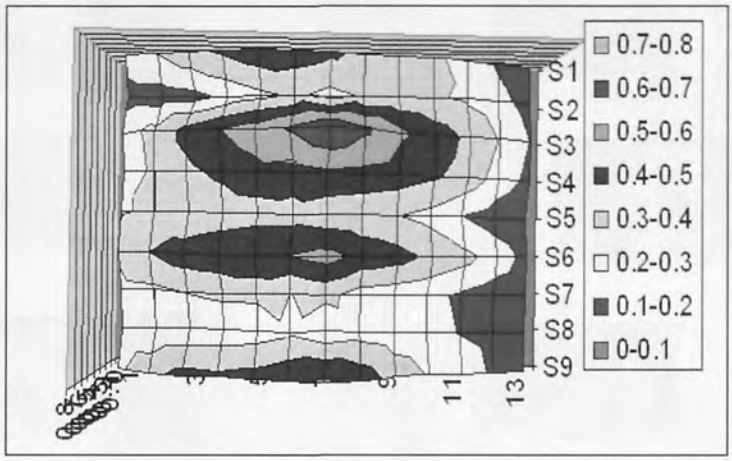

Fig.66.Combined wavelength shift (nm) for all sensors v position of load, vertical sensors.

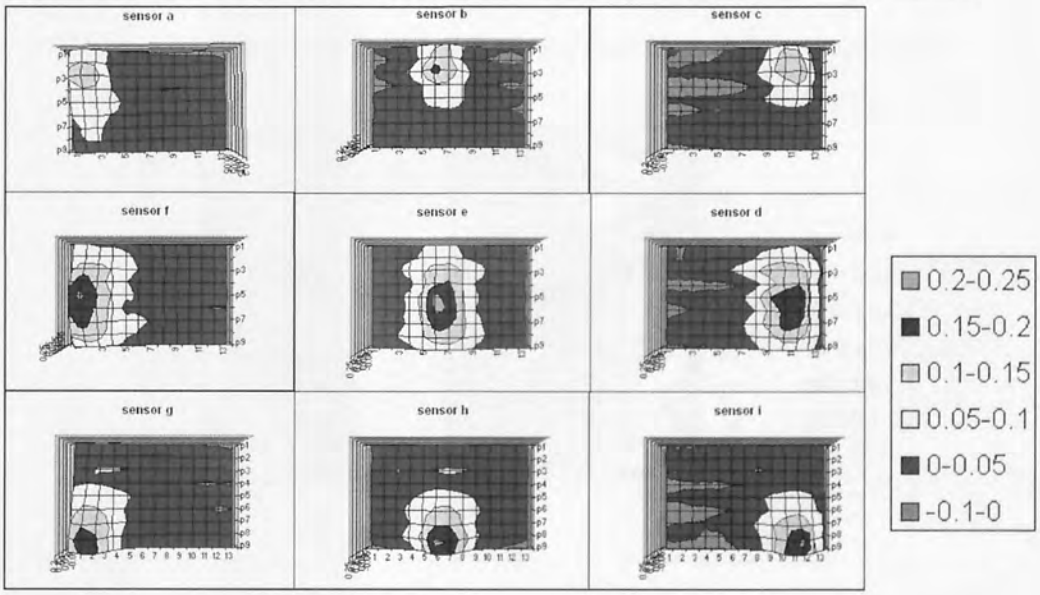

Fig. 67 Individual sensor wavelength shifts (nm) v location, horizontally arranged sensors.

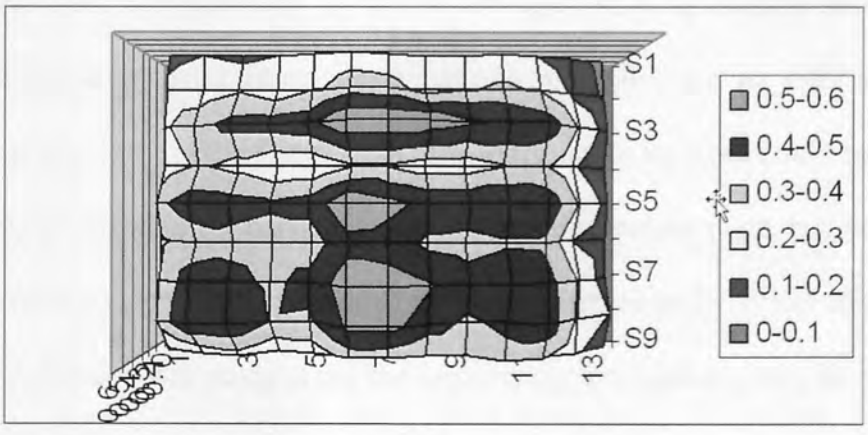

Fig.68.Combined wavelength shift (nm) for all sensors v position of load, vertical sensors.

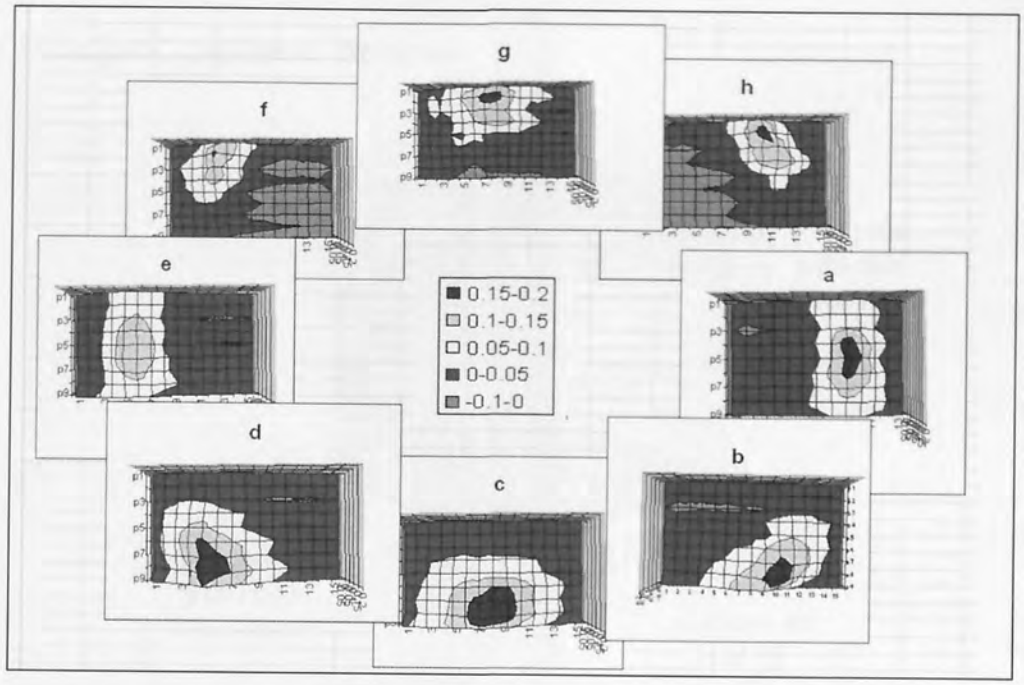

Fig. 69 Individual sensor wavelength shifts (nm) v location, radially arranged sensors

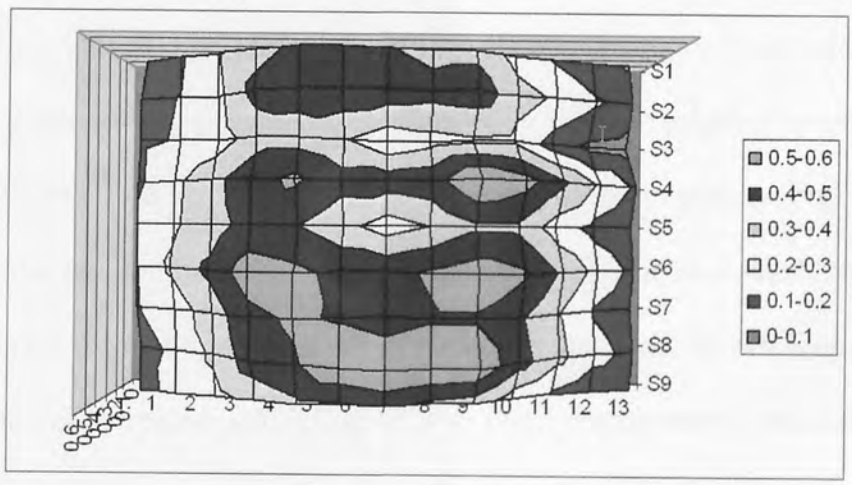

Fig.70.Combined wavelength shift (nm) for all sensors v position of load, radial sensors.

It can be seen from figs 66,68 and 70, that the arrangement in fig 68 gave the most even coverage of sensitivity, with the smallest areas of low sensitivity at the right and left ends of the plate. Some of the variation in sensitivity across the plate could be attributed to the quality of the adhesive bonds between the gratings and the plate, but the 'end effects' are common to all three sensor configurations so are probably not adhesive related. The decision was made to use the horizontally arranged sensors, but with future layouts arranged symmetrically.

4.8 Principal Components Analysis

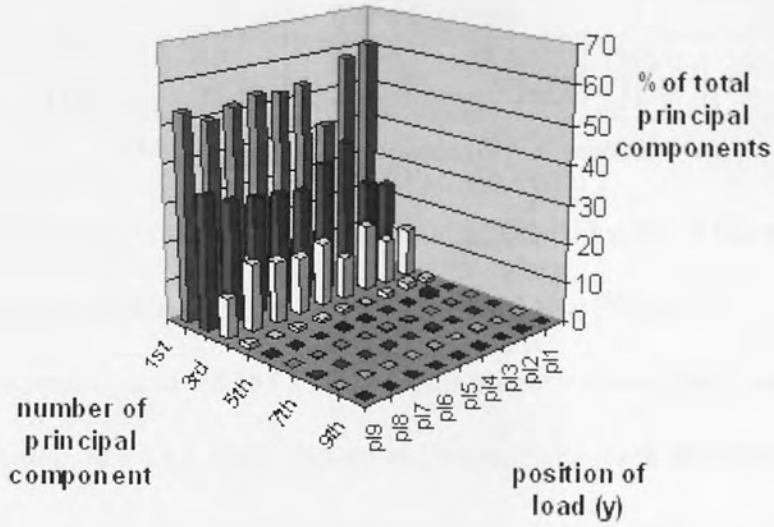

Fig. 71 Results of principal Components analysis of data from horizontal sensors

Pensiri Tongapadungrod [47] found that principal components analysis suggests that fewer than 9 sensors are necessary to account for 99 % of the principal components of the data collected from her 'smart surface' using displacement sensors. Fig. 71 shows that this is also true for the sensor arrangement used here. The most significant principle components are the first 4, and analysis of the numerical values shown here graphically (components calculated using MATLab) shows that 5 components account for at least 99% of the principle components, implying that only 5 sensors are theoretically required.

4.9 Preliminary Results

4.9.1 Position sensing

The data collected from each smart surface were processed using neural networks to assess the accuracy with which the system could predict the position of the load (see Table 6). For these results x represents the short side of the surface, y represents the long side of the surface.

Sensor arrangement	Average x error (mm)	Rms x Error (mm)	Average x error %	Average y error (mm)	Rms y error (mm)	Average y error %	rms r error (mm)	No. of hidden nodes
vertical	1.8	2.5	0.7	2.3	3.3	0.7	4.2	23
horizontal	7.4	10.0	3.1	7.6	10.0	2.2	14.2	23
radial	11.2	15.1	4.7	13.1	18.1	3.8	23.6	9

TABLE 6 – Results for detection of load position

Percentage errors were calculated based on the unsupported length of the surface (as used to calculate percentage errors in [47]) see fig 14, 240 x 340mm.

For each of these results a set of 585 sets of sensor output wavelengths were recorded, 5 sets in each position on a 13 x 9 grid spaced at 20mm. Each block was divided into 3 and used to train, validate and test a neural network. In a sense the results above reflect primarily the internal consistency of each block of results. The 'acid test' of this system is to use a completely separate set of data, collected independently of the training and validation data, with which to test the neural network. Three such blocks of data were collected, each of 585 results (one for each arrangement of sensors).

Sensor arrangement	Average x error (mm)	Rms x error (mm)	Average x error %	Average y error (mm)	Rms x error (mm)	Average y error %	Rms r error (mm)	No. of hidden nodes
Vertical	245.4	262.9	102.3	111.8	147.6	32.9	301.5	23
Horizontal	129.0	159.4	53.7	259.3	286.2	76.3	327.5	23
Radial	85.7	105.5	35.7	86.8	116.5	25.5	157.2	9

TABLE 7 Results for detection of load position using independently collected test data

The results shown in Table 7 show a very low accuracy, and the reasons for this are discussed in section 4.10. The distribution of the error across the surface is shown in fig. 72.

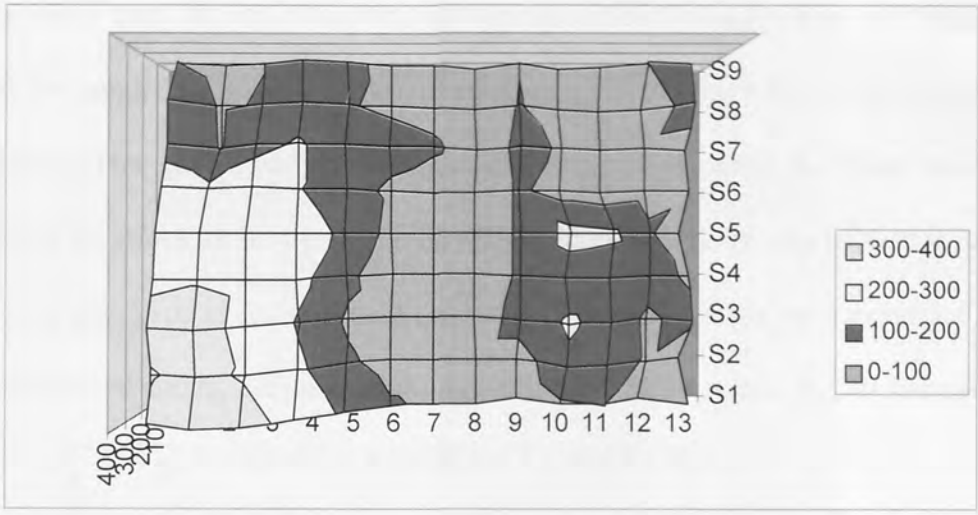

Fig.72 Plot of x errors (mm) v position, horizontal sensor arrangement

4.9.2 Shape, size and orientation sensing

One technique for expanding a data set for use with neural networks is to add randomly generated numbers with the same mean and standard deviation as the original dataset to obtain sufficient data to train, validate and test a system. This simulated data is however probably less representative than experimentally derived data, in that it probably contains less variability than would be obtained experimentally. The following results were obtained using a small experimental dataset artificially expanded in this way. The mean and standard deviation of the experimental sensor data were calculated, then Microsoft Excel's random number generation function was used to produce extra values to add to the data set.

4.9.2.1 Shape

The surface with radially arranged sensors was used to implement shape sensing, with 4 loaded shapes of equal area and weight and constant orientation: circle, square, equilateral triangle and rectangle. Initially the shapes were placed at the centre of the surface. A neural network was trained and gave 100% correct shape detection. This network had 19 nodes, with a softmax activation function i.e. performing a

categorization task. 10 sets of sensor data were recorded for each shape, and these 40 sets were expanded to 300 sets as described above, 100 of which were used for testing. The same surface gave a correct shape sensing rate of 97% when the shape was placed in one of 6 positions as shown in fig. 73. (19 hidden nodes). 10 sets of sensor readings were taken per shape at each of the 6 positions (240 sets), which were expanded to 720 sets as described above. This gave training, validation and test data of 240 sets each.

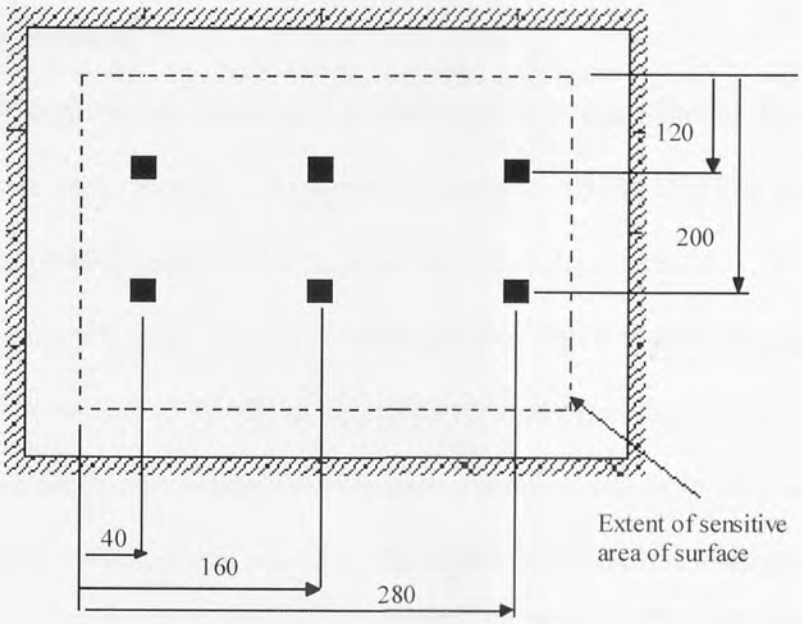

Fig. 73 Location of 6 load positions used in 4.9.2.1

4.9.2.2 Size and shape

Five sets of 4 shapes, each of different sizes (see Table 8), were placed in turn at the centre of the surface, and the data were used to train and test neural networks to recognise (a) the size, irrespective of the shape and (b) the shape, irrespective of the size. The results were 100% correct for size and 88% correct for shape. A constant load of 291g was used each time. 15 data sets were recorded per shape for each size, giving 300 sets in all. 100 sets were used for training, validation and testing respectively. No artificial expansion of the data set was necessary.

Size	1	2	3	4	5
Area	400mm^2	1225mm^2	2500mm^2	4225mm^2	6400mm^2
Square (side)	20mm	35mm	50mm	65mm	80mm
Triangle (side)	30.3mm	53mm	76mm	98.6mm	121.3mm
Rectangle	26x15.4mm	45.5x22.2mm	65x38.5mm	84.5x50mm	104x61.5mm
Circle (radius)	22.6mm	39.4mm	56.5mm	73.3mm	90.3mm

TABLE 8 Dimensions of shapes used for size and shape sensing.

4.9.2.3. Orientation

Using the triangular and rectangular shapes (size 3), in the centre of the surface, sensor output values were recorded for angular positions at increments of 15 degrees. These data sets, artificially expanded, were used to predict the orientation of a load. The results are shown in Table 9. For the rectangle five data sets were recorded for each orientation, expanded to 30 sets as described previously, giving 120 sets each for training, validation and testing. Correspondingly fewer sets were used for the triangular shape because the number of possible orientation positions was 8 rather than 12.

	Average error (degrees)	Rms error (degrees)
Triangle	2.4	3.3
Rectangle	5.0	8.5

TABLE 9 Accuracy of orientation sensing

A second set of independently collected data for the triangular shape was then used to test the neural network. The errors produced are shown in table 10

	Average error (degrees)	Rms error (degrees)
Triangle	49.1	61.3

TABLE 10 Accuracy of orientation sensing using independently collected data.

Considering the symmetry of the shape, the maximum orientation angle is 120 degrees, so these results are not much more accurate than random guesswork, which would give

an average 60 degrees error. This trial used 4 sets of independently collected data for testing the neural network, each set comprising 5 sets of sensor readings per orientation. These results are not as accurate as had been expected, given the results achieved in [27], and the causes of the low accuracy were investigated. It was found that the sensor readings for the same load in the same position were not always the same, and this lack of repeatability was investigated further.

4.10 Repeatability

4.10.1.Quantification of repeatability problem

In order for accurate sensing of the parameters of a load on the surface, it is desirable that each time the same load is placed in the same position on the smart surface, the sensors react in the same way. Any differences in sensor outputs for the same load should be substantially smaller than differences measured when different loads (those we are attempting to distinguish from each other) are applied.

It was found that in practice the repeated application of the same load produced variations as shown in fig 74. Variations in loaded sensor output of up to 60pm can be observed.

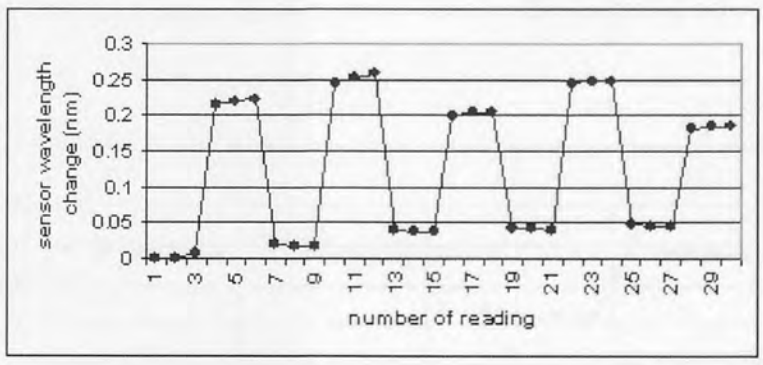

Fig.74 Typical response of sensor to repeated application of load.

The effects of this lack of repeatability are particularly apparent when collecting data for different shaped loads of the same area and weight, where the differences in sensor

signals between the different shaped loads are smaller than the inconsistencies shown above.

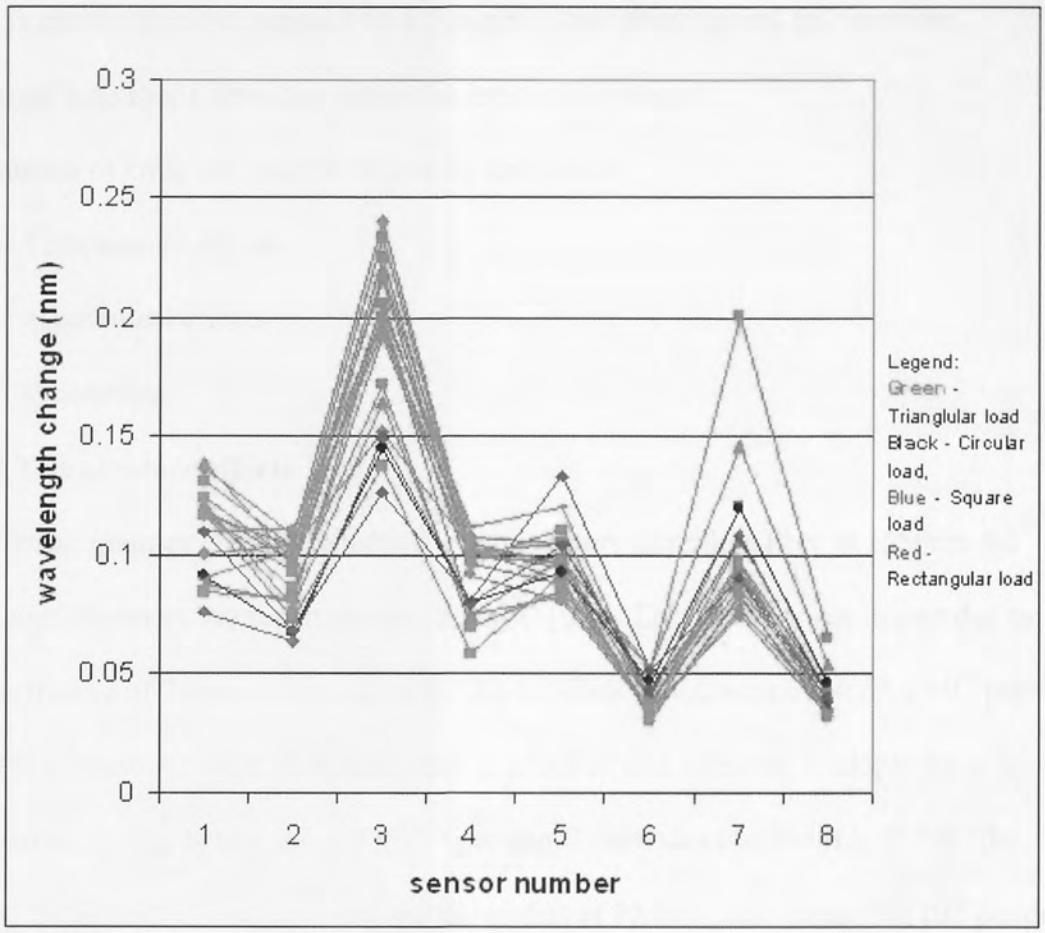

Fig. 75 Comparison of sensor outputs for different load shapes

Fig 76 shows that there is a variation of at least 50pm in the output of sensor 3 for a triangular load.

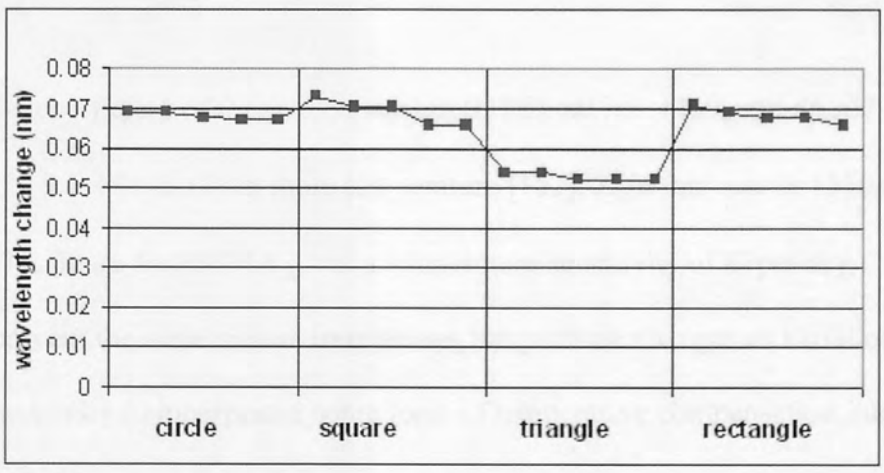

Fig 76. Response of a typical sensor to different load shapes

Fig. 76 shows that the difference in a typical sensor output between the different load shapes is 10-20pm. The fact that the variability of a sensor output for the same load shape is greater than the response to a change in load shape means that accurate, consistent load shape detection cannot be expected to occur.

The sources of error fall into the following categories:

1. Temperature effects
2. Mechanical effects
3. Processing

4.10.2 Temperature effects

Fibre Bragg gratings are very sensitive to temperature (for silica fibre at 1550nm the wavelength-temperature sensitivity is 13 pm/°C [61]). This figure arises in part due to the Coefficient of Thermal Expansion (CTE) of Silica Glass, which is 0.55 x 10^{-6} per °C [151,152]. However when an optical fibre is attached to a substrate it adopts the CTE of the substrate [152], in this case 50 x 10^{-6} per deg C for a sheet of PMMA. [153]. The CTE of the adhesive used was very similar to that of PMMA, also being 50x10^{-6} per deg C [154].

The wavelength-temperature sensitivity of an FBG is given by

$$\frac{\Delta\lambda}{\Delta T} = \lambda_0 \left(\alpha + \frac{1}{n_0} \frac{\mathrm{d}n_0}{\mathrm{d}T} \right) \quad [152]$$

where α is the coefficient of thermal expansion (CTE), $n0$ is 1.4469, and $\mathrm{d}n_o/\mathrm{d}T$ is approximately 9.1 x 10-6 .C^{-1} at room temperature [152]. λ_0 in this case is 1550nm. Using the CTE figure for PMMA gives a temperature sensitivity of 87pm/deg C.

In order to prevent the system from interpreting temperature changes as variations in strain, it is necessary to incorporate some form of temperature compensation into the system to track the environmental temperature changes. The experiments conducted in

part 2 above took place in an air-conditioned room, but the variations in sensor readings as the temperature varied (15pm) were still large enough to be comparable to the difference in sensor readings recorded for different shaped loads (typically 10-20pm)(see figure 77).

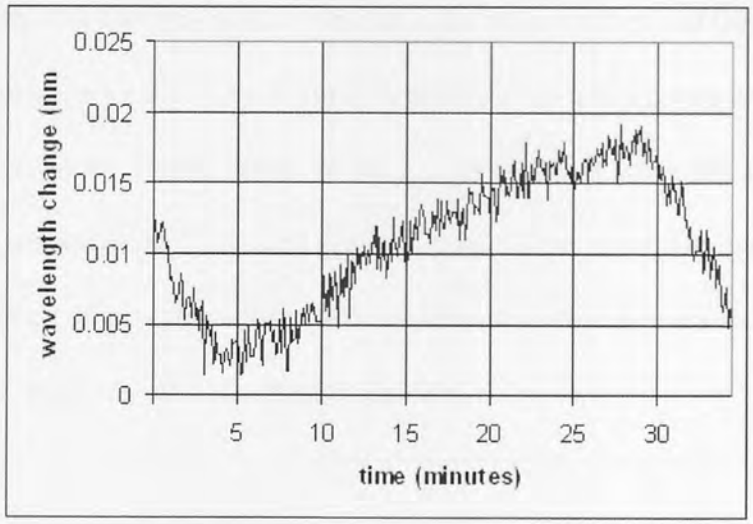

Fig. 77 Temperature induced wavelength change for one sensor.

The system initially adopted during data collection was to record unstrained sensor values immediately before taking strained values, then subtracting the unstrained values from the strained values. The maximum number of strained values taken was 10, so that the maximum time lag between the unstrained value and the last strained value was about 10 seconds (the OSA refresh rate is approx 1 sec). However it was found that the large metal loads being used in these experiments appeared to be causing cooling when they were applied to the surface. Although this was probably an illusion (everything in the air-conditioned room had time to reach an equal temperature) it could be a problem in a real-life situation if objects of a different temperature made contact with the smart surface. The temperature change experienced by the sensors due to a higher or lower temperature load would be interpreted as a change in strain so may cause errors in sensing load parameters, particularly load weight. Two solutions were used to combat this problem (a) the loads had a 1mm thick (approx) layer of cork applied to their

underside to thermally insulate the load from the surface and (b) unstrained values were recorded after the strained values (rather than before) so that any temperature effect due to the application of the load to the surface remained during the recording of the unstrained values. Felt (4mm thick) was also assessed as an insulating medium, but it was found that the thickness of the felt obscured the shape of the load (see fig.78). Outside the laboratory setting, a more suitable approach to temperature compensation would be to insert an unstrained sensor in the system so that it was subject to the same temperature variations as the 9 strained sensors. It would be important that this extra sensor was attached to the same substrate material as the other sensors so that it would be subject to the same effects of thermal expansion.

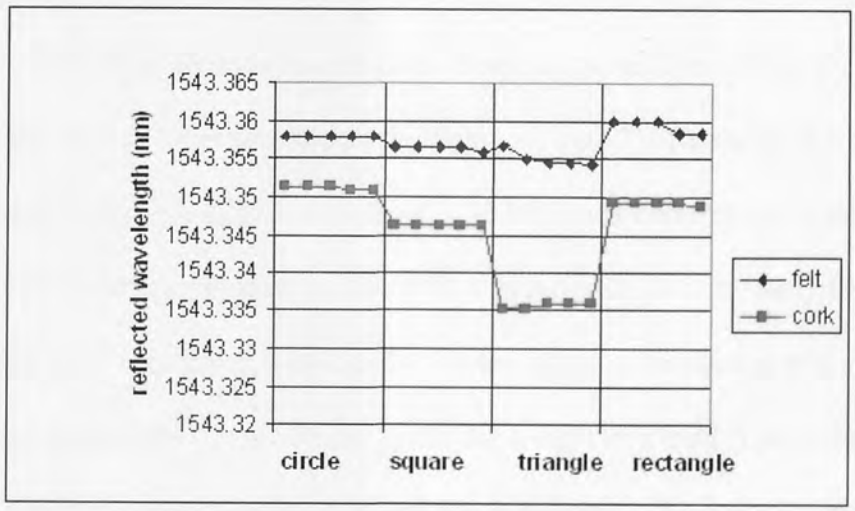

Fig. 78 Comparison of felt and cork as insulating materials (single sensor)

4.10.3 Mechanical effects

4.10.3.1.Material Creep

Material creep when a load is applied to the smart surface is not negligible. Fig. 79 shows FBG sensor readings as a function of time for glass, stainless steel and PMMA. Stainless steel was chosen for subsequent designs as the substrate for the smart surface, since it exhibits low material creep.

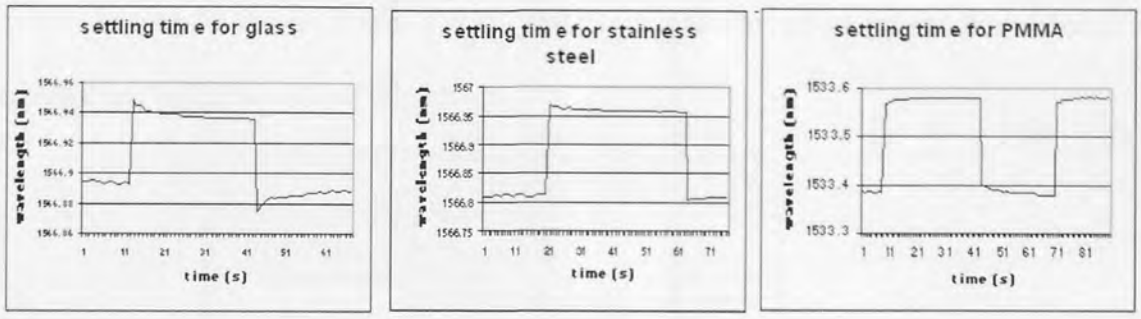

Fig. 79 Sensor output vs. time for 3 different materials.

Eliminating the effects of creep when recording training and validation data was achieved by allowing a few seconds delay between applying the load to the surface and recording the sensor data. However the effect of material creep in a real-time system is to give errors in the load position (or shape detection) when the load is first applied to the surface, which combined with the OSA refresh rate means that the system takes several seconds to settle to a consistent value. Some of the creep is due to the adhesive with which the sensors were attached to the smart surface. 3 different epoxy adhesives (Araldite Rapid 2-part epoxy adhesive, Epotek 353ND heat cured epoxy and SP Systems sp320 2 part epoxy) were assessed for this purpose; unfortunately the one which produced the least creep was found to be too brittle to be used in this application since it cracked when the surface flexed under the weight of a load. The other two exhibited a similar degree of creep, and Araldite Rapid was used due to its quick drying time and ready availability.

4.10.3.2 Play

A second mechanical issue arises from the fact that the surface was simply supported and therefore had some 'play' within its retaining structure. This might mean that the surface did not return to exactly the same position each time after loading and unloading. An experiment was conducted to compare the strain values experienced by the sensors if the surface was screwed to the supporting framework instead of being

simply supported. It was found (fig. 80) that the magnitudes of the sensor strain changes in response to identical load conditions

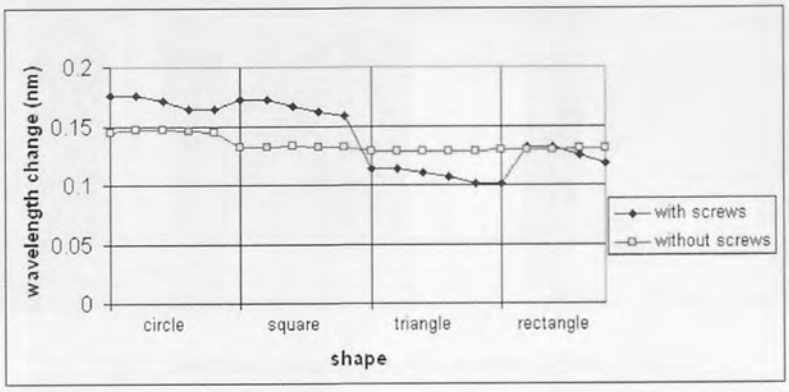

Fig. 80 Single sensor output for different plate support arrangements

compared favourably with those for the simply supported arrangement, and subsequent designs used a screwed down plate.

4.10.3.3 Position of load on base shape

Data for the preliminary results (section 4.8) were taken using a thin wooden base shape with a heavy metallic load placed on it (fig 81). Whenever the shape was moved, the position of the load on the base shape was adjusted. It was felt that this may affect the position of the centre of gravity of the load, and four mild steel blocks (see fig 82) were specified to eliminate this possible source of error. Each block was 82mm high, the square was 50mm along its edges, the circle was 56mm in diameter, the triangle (equilateral) was 76mm along its edges and the rectangle was 38mm x 65mm, so that the base area and weight of each block was the same.

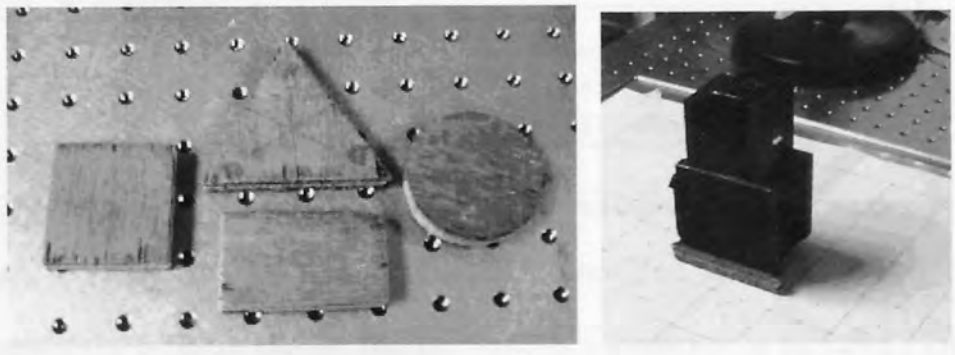

Fig. 81 Wooden base shapes (left) on surface with metallic loads (right)

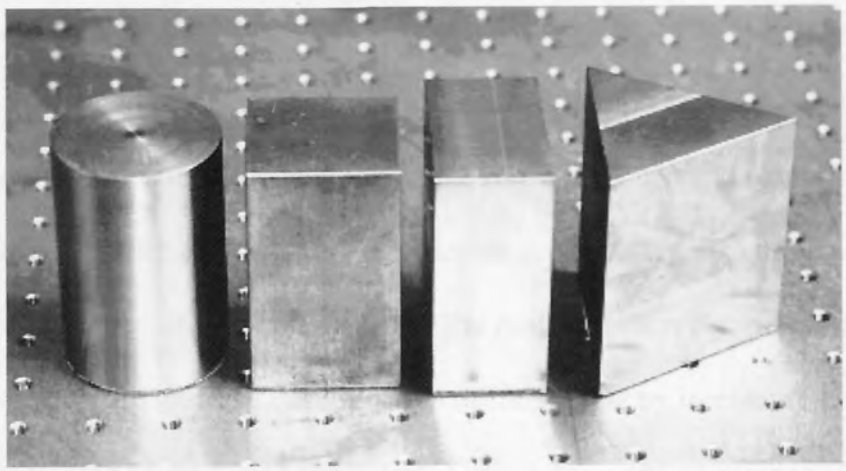

Fig.82 Steel blocks used to replace arrangement in fig. 82

4.10.4 Processing.

Because of the small deflections involved when a load was applied to the surface, the wavelength shifts measured by the OSA were between 20pm and 120pm, depending on the proximity of the load to a given sensor. The differences in wavelength due to different load shapes were sometimes as small as 3pm. This led to repeatability problems because of wavelength variations due to other factors e.g. the OSA measurement accuracy, temperature

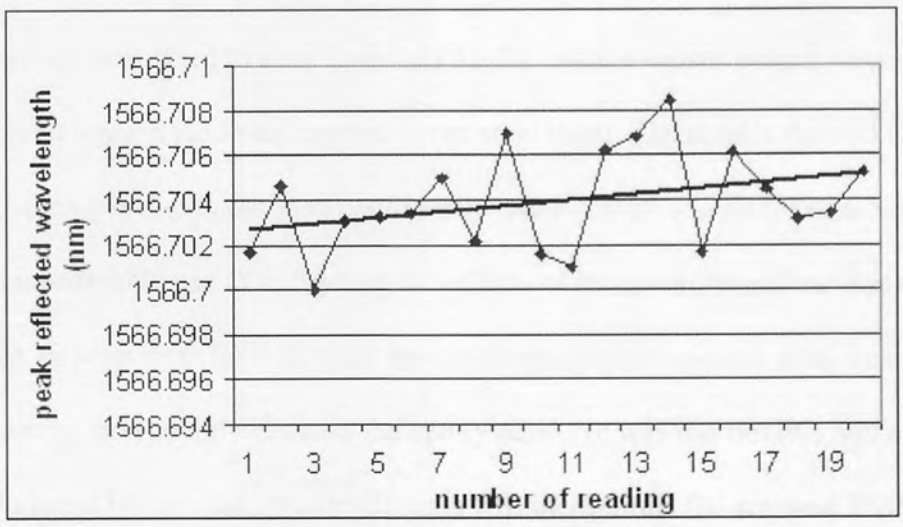

Fig. 83 Output of temperature correction sensor over 20 readings (approx. 1 min.) with trend line (linear)

effects and noise affecting the peak detection algorithm. The OSA had to be set to a sweep bandwidth of 50nm in order for data from all 9 sensors to be included. However

this meant that each spectral peak was only described by a few data points, and the addition or subtraction of a data point within a peak as the spectrum altered in response to a load had a significant effect upon the output of the peak detection algorithm. Fig 83 shows the slow upward trend caused by temperature changes but also the random noise produced by the combination of the OSA and the peak detection algorithm. It was not considered desirable to increase the deflection of the surface by increasing the weight of the load because this might have permanently distorted the surface material The reason the wavelength shifts were so small was that the FBG sensors are effectively mounted very close to the neutral bending axis of the sheet material; the PMMA only being 1.5mm thick. One solution to this problem was to attach a second layer of a material with a much lower Young's modulus beneath the smart surface, and attach the sensors to this lower layer so as to increase the distance between the sensor and the neutral bending axis of the surface.

Two layers of PMMA, each 1.3mm thick were applied to a steel sheet 0.5mm thick, similar to the PMMA one described above, using (a) epoxy adhesive and (b) screws. One FBG sensor was fixed to each layer of PMMA and the sensor output wavelengths were measured when a load was applied to the steel sheet. The results showed that the wavelength changes due to the load could be increased by up to a factor of 6.5, which will be of considerable use in mitigating the effects of temperature and mechanical creep. It can be seen from table 11 that the use of epoxy glue was not as successful as screw mounting, presumably because the epoxy adhesive was too flexible and absorbed the strain induced by the load. Future designs will incorporate the screwed PMMA layers. Adding the layers of PMMA to the underside of the steel sheet is not expected to alter the bending characteristics of the surface significantly because the Young's Modulus of Steel (190-210GPa) is so much higher than that of PMMA (3-4GPa) [153].

The PMMA will also serve to insulate the sensors from any temperature change caused by an applied load.

No. of Layers of PMMA	Wavelength change Glued (nm)	Wavelength change Screwed (nm)
0	0.19	0.19
1	0.23	0.58
2	0.14	1.23

TABLE 11.Using PMMA Layers To Enhance Sensor Response

4.10.5 Conclusions and choice of material

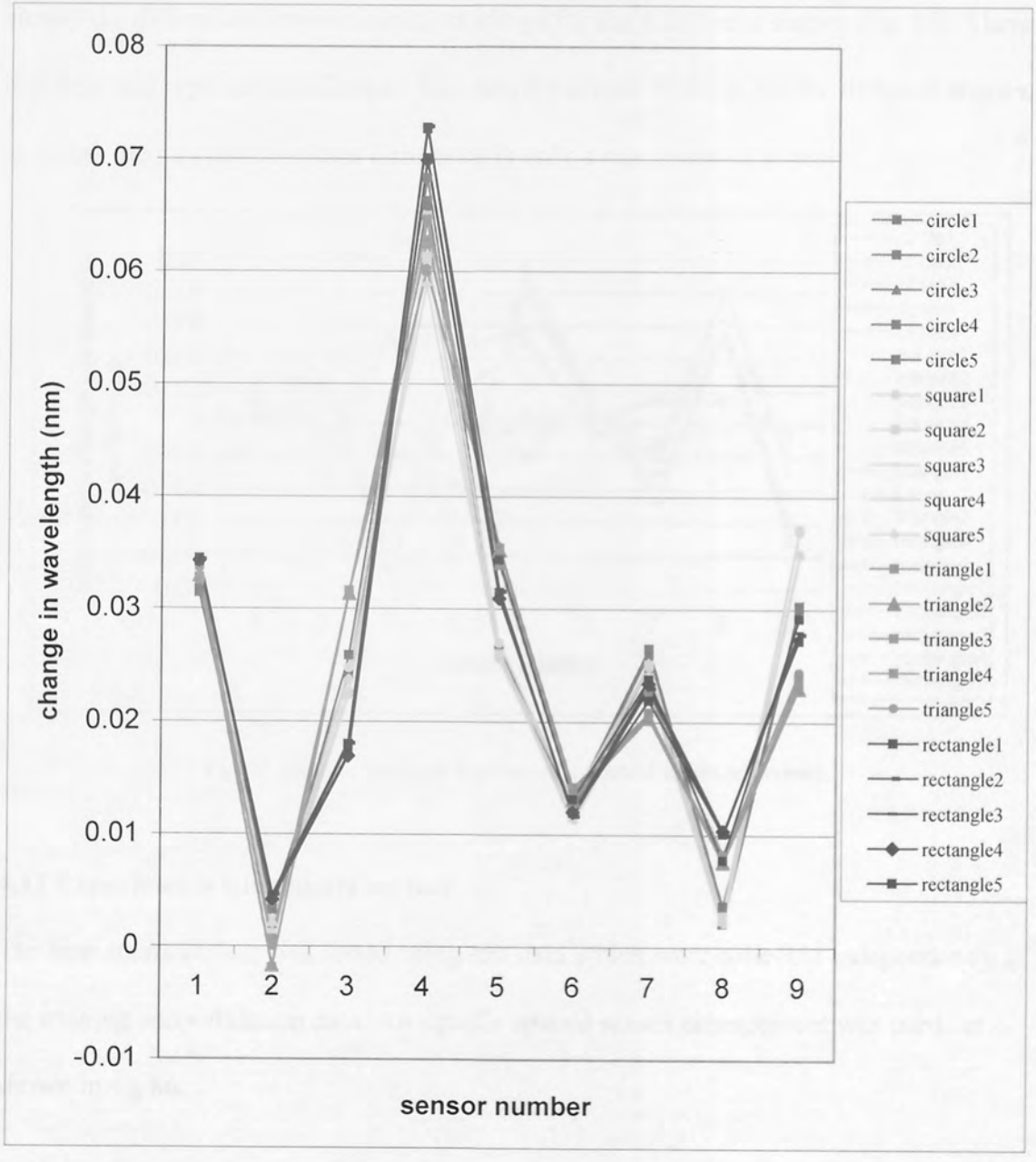

Fig 84 Sensor outputs for different shapes after modifications (compare with fig. 76)

After all the modifications and changes of material described above had been included in the design, the smart surface was tested with 4 different shapes (in one position), to see whether the different shapes occupied different areas of signal space. Fig. 84 above shows that there was now small but significant separation between the various shapes which compares favourably with fig. 75 (section 4.10.1) in which there was no separation.

Plotting the same values as in fig. 84 but relative to the circle1 results shows more clearly the difference between sensor readings for the 4 different shapes (fig. 85). There is a clear and repeatable difference between the sensor readings for the different shapes, although the magnitude of this difference is only a maximum of 10pm.

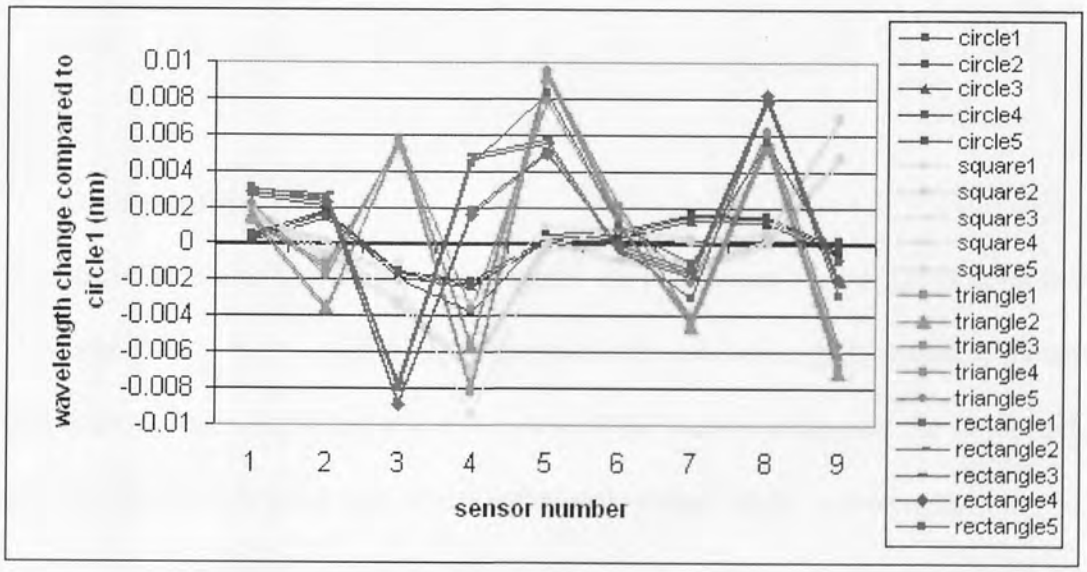

Fig. 85 Change in sensor wavelengths relative to circle1 values.

4.11 Experiments with smart surface

The new smart surface was tested using test data which were collected independently of the training and validation data. An equally spaced sensor arrangement was used, as shown in fig 86.

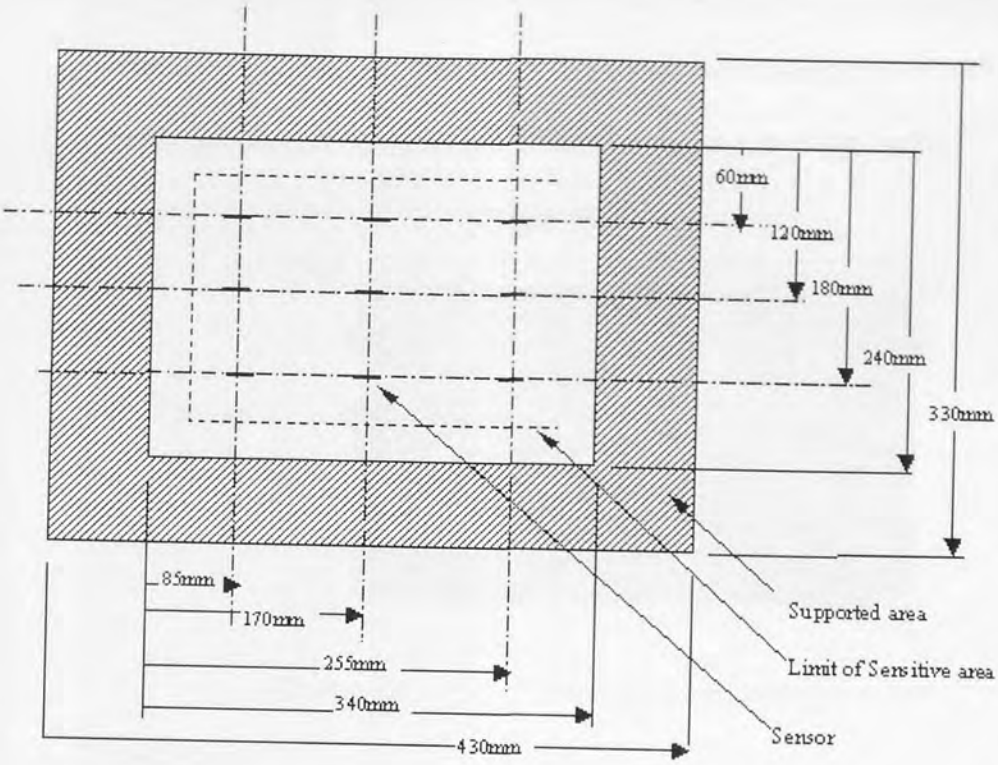

Fig. 86 Layout of sensors on 2 Dimensional tactile surface

4.11.1 Load position

The smart surface was first trained to recognize the position of a load placed upon it. A load was applied to the plate at all possible positions on a 20mm grid, avoiding the area within 40mm of the supporting structure to avoid the loads overlapping the supported edge of the surface. At each load position the peak sensor output wavelengths were recorded. Three sets of data were recorded at each load position, for training, validation and testing respectively. Neural networks with numbers of hidden nodes between 9 (the number of inputs to the networks) and 50 were trained.

The surface was able to detect the load position with an rms error of approximately 11mm (2.7% of full scale). The largest errors were generally found to be around the edges of the surface (fig. 87), possibly because fewer of the sensors were significantly active when the load was close to the edge of the plate. By comparison a similar arrangement using 16 infrared displacement sensors [47], shown in section 4.1 had an

average error of 4.5%, and confined the position of the centroid of the objects used to a 'sensitive area' of dimensions100mm x 150mm at the centre of the surface.

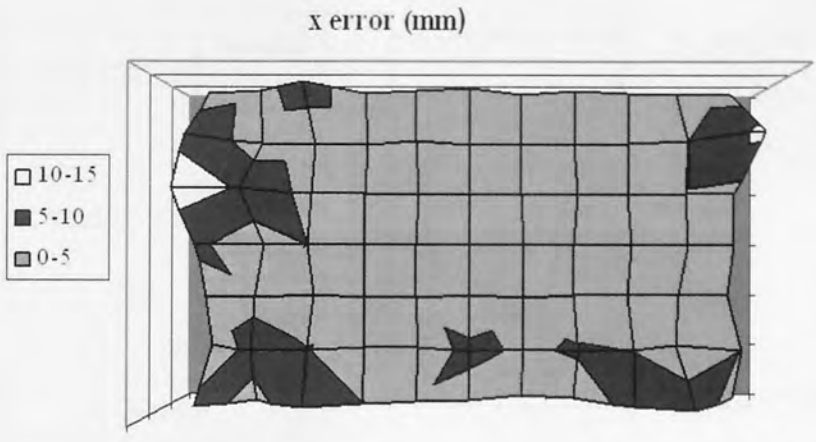

Figure 87. Map showing RMS error (mm) in load position detection

4.11.2. Load Shape

Next the system was trained to recognize the shape of a load (at a constant orientation), using four shapes of equal area and weight. Initially the load was placed at a set position, and the shapes were distinguished successfully 100% of the time. Then the range of positions on the surface at which the load was placed was increased until the entire sensitive area of the plate was used. The shape of a load at any position, with the position known, was detected with an accuracy of 91%. The shape of a load at any position, with the position unknown, was detected with 89% accuracy.

4.11.3 Simultaneous shape and position detection

There are two possible approaches to simultaneously detecting 2 different types of parameters using neural networks (in this case a continuous measurement of position and a shape classification task), since it is not possible to use a single network to perform both a linear regression task and a classification task. One is to use a parallel arrangement, where one network processes the data and predicts the load position while another predicts the load shape (fig. 88a). The second approach is to use a cascaded arrangement where one network determines the load position and then that information

is fed along with the sensor information into a second neural network which determines the shape (fig. 88b).

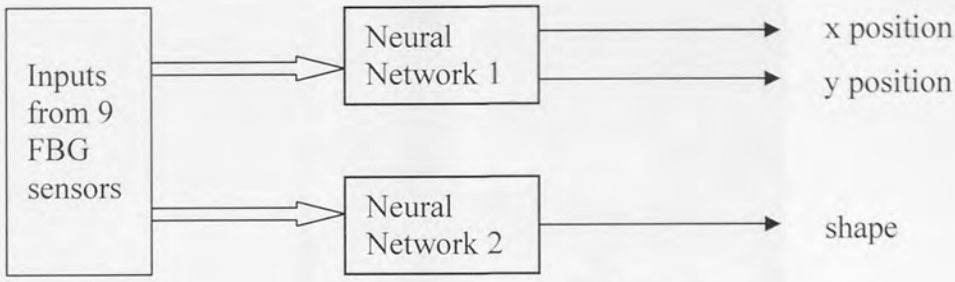

Figure 88a: Parallel Networks

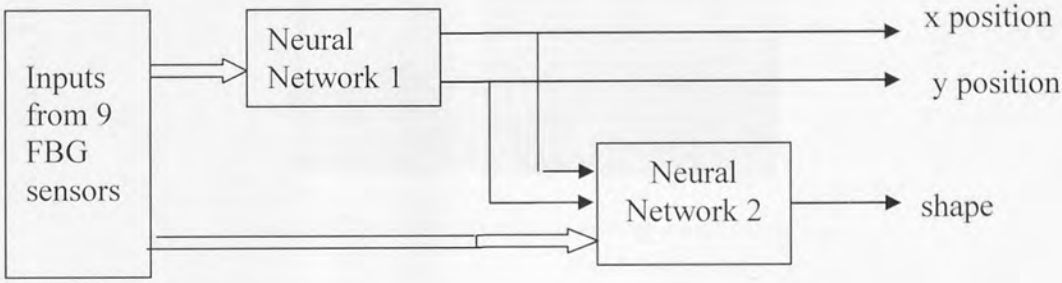

Figure 88b: Cascaded Networks

The result above (89% shape detection accuracy) is effectively from the parallel arrangement. The cascaded arrangement gave a shape detection accuracy of only 85%. This shows that the neural network is capable of detecting the shape of a load without the additional information regarding the load position. It is likely that the decrease in accuracy in the second case is due to the errors in detecting the load position causing a decrease in load shape detection accuracy.

4.11.4 Two Load Detection System

The sensing surface was trained to recognize the position of two identical loads placed simultaneously on the surface (fig. 89). The neural networks were trained using data collected with the two loads at every possible combination of positions on a 5x7 grid at intervals of 40mm in both directions. The success rate was 100% for detecting correctly the number of objects on the surface (0, 1 or 2) and there was an rms error of 19mm (4.8%) for detecting the position of each object

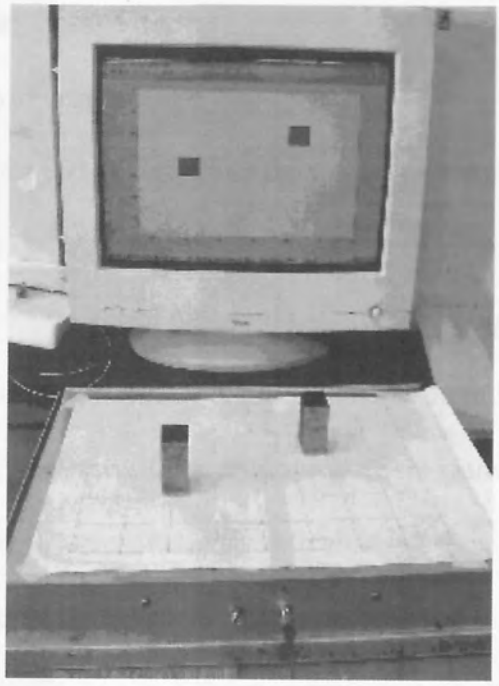

Figure 89 Two load detection operating close to real time

4.12 Footplate

4.12.1.Scaling up the smart surface

Although the steel sheet used above could have withstood a load of over 20kN before its elastic limit was exceeded, and the maximum load for the footplate, being made of thicker material, would be greater than this, a limit to the allowed deflection of the footplate when under load was defined as 2mm, since it is undesirable for a user to detect a significant deflection while stepping onto such a device. A steel sheet was used with a 4mm layer of Perspex attached with screws to the underside of the steel sheet. The size chosen for the sensitive area of the footplate was 480 x 390 in order to accommodate typical foot sizes, adding 50mm all round for supports gave an overall size of 580 x 490mm.

The thickness of the steel sheet was 2.5mm. The design of the footplate can be seen in Appendix 1.

4.12.2 Experiments using Footplate

4.12.2.1 Sensor output variations

I stood on the footplate (fig 90) to determine the average sensor wavelength changes and to assess whether the deflection of the steel plate was large enough to feel unsafe. It was found that the deflection was not perceptible and the average sensor wavelength change was only 120pm (max 180pm). I decided that although I am not the heaviest potential user of the footplate it would be an improvement if the steel plate were thinner and deflected more so that the sensor wavelength changes were larger and the signal to noise ratio improved. The thickness of the plate was changed to 1.5mm. This made the average wavelength change 260pm and the max 800pm. This was considered to be a suitable level of flexibility since there was the possibility that if the Perspex plate bent too much the epoxy adhesive would become detached from it and the sensors would no longer function.

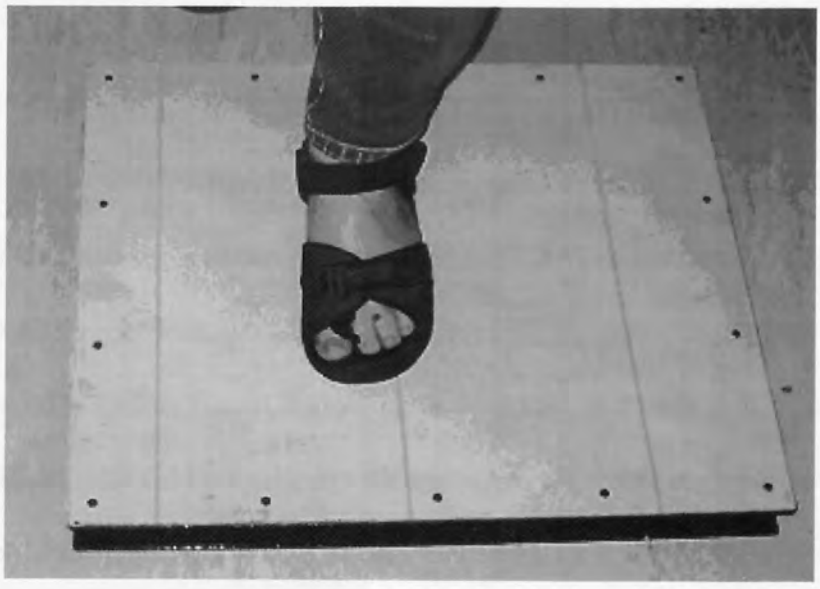

Fig. 90. Footplate

4.12.2.2. One or two feet

As a simple evaluation of the possibilities of the footplate I stood on the footplate either on one foot or on two feet, in a variety of positions and orientations on the

board to see whether the system could be trained to distinguish between these two options. This was done twice, once using a network with two softmax outputs (7 hidden nodes) and once using a network with a single logistic output (14 hidden nodes). Both the networks were found to be capable of distinguishing between one and two feet 100% of the time.

4.12.2.3 People of different weights

Four people of different heights and weights (Table 12) stood on each foot in turn on the footplate, in different positions and orientations. The loaded sensor wavelength shifts for the 4 people were used to train neural networks with softmax activation functions, to discover whether the neural networks were capable of distinguishing between people.

Person	Shoe size	Height	Weight
User 1	8	1.68m	67kg
User 2	12	1.93m	110kg
User 3	7	1.65m	60kg
User 4	6	1.63m	66.5kg

TABLE 12 Heights, weights and shoe sizes of footplate users

It was found that a neural network with 7 hidden nodes could be trained so that it was capable of distinguishing between these individuals 100% of the time.

4.12.2.4 Left and right feet.

A single user stood on one foot at a time on the footplate in a variety of positions and orientations in order to find out whether the system could distinguish between right and left feet. The success rate was 100% for one user and 97.7% for four users wearing a variety of footwear (17 hidden nodes).

4.12.2.5 Different footwear

A single user stood on their left foot in two opposing orientations on the footplate wearing 3 different forms of footwear- sandals, trainers, and socks. A neural network

with 7 hidden nodes was found to be able distinguish correctly between the types of footwear 100% of the time.

4.12.2.6 Weight distribution

One user stood on the footplate on their left foot in a single orientation on the footplate, but in 5 different positions. In each position sensor readings were recorded for 5 different situations: weight on centre of foot (normal), weight towards heel, weight towards toes, weight on right of foot, weight on left of foot. A neural network with 9 hidden nodes was able to distinguish 99% of the time where the user had their weight. Although the user adopted quite exaggeratedly imbalanced positions for the purpose of this trial, this was an interesting result because it indicates that this type of system might be useful in the study and diagnosis of balance and gait disorders and in podiatry.

4.12.2.7 Individuals

Two individuals (users 3 and 4) of similar height and weight and wearing identical footwear stood on the footplate in a variety of orientations. A neural network was trained to distinguish between the two individuals 100% of the time. This implies that this system may have applications in security systems

4.13 Future work and possible applications.

The smart surfaces described above are useful prototypes for assessing the potential applications of distributive tactile sensing systems incorporating optical fibre sensors. Further work necessary before a useful product could be made includes making the system cheaper and more portable (eliminating use of an OSA for example) and making the system quicker. As previously mentioned (section 4.10.2) a temperature correction sensor is necessary.

Possible applications for the smaller smart surface include pick and place systems, where the shape, size or orientation of an object could be detected before a robotic

manipulator attempted to pick it up. The footplate has applications in gait analysis and podiatry, as mentioned above (section 4.11.2.6) and in security systems (4.11.2.7). At present gait analysis systems either incorporate large numbers of sensors, e.g the Gaitrite system (see fig. 91, left) incorporates over 16,000 sensors, or use complex imaging systems (fig. 91, right). Further development in collaboration with medical professionals would be necessary to identify the potential applications and study the markers for medical conditions that may be detectable using this type of system.

Gait analysis also has applications in veterinary and agricultural fields. Dairy cattle are prone to a variety of different foot conditions: hard and soft feet, foot rot, heel erosions, laminitis, digital dermatitis, and sole ulcers. Each of these can lead to lameness, which involved expensive veterinary care and can lead to having a valuable animal destroyed. Often the way the animal distributes its weight on its hoof can be a sign of hoof problems. For example if the hoof horn becomes overgrown the body weight shifts and the bulbs of the heel come into contact with the ground. The bulbs are sensitive, and some cows with excessively long toes develop lameness because of bruising of the bulbs of the heel [177]. This type of footplate is slim and can be made rugged, so it

could be recessed into the ground of a farmyard or milking parlour, rather like a weighbridge, and give warning of bovine foot problems.

Gait analysis is also used to help athletes, both human and equine, to improve their performance, and it is possible that this type of system could be used in these areas too.

4.14 Conclusions

FBGs perform at least as well as infrared displacement sensors in a distributive tactile sensing surface. They can be used to detect the position, shape and other attributes of a load. The surface was able to detect the load position within 2.7% of full scale, the shape of a load in a known position 91% of the time (89% if the position was not known), and the positions of 2 identical loads within 4.8% of full scale. There are several difficulties to be overcome in this type of sensing system, some of which are specific to FBG sensors (temperature related effects and adhesive properties) and others (such as mechanical creep of the surface) which are general to all sensor types. This latter issue may be important when this work is extended to dynamic signals. In the work described in this chapter it was possible to allow time for the surface to reach a steady state before taking sensor readings. In other applications of this system, such as gait monitoring, dynamic signals would be monitored. The advantage of using Neural Networks to interpret the sensor data is that it may be possible for a Neural Network to extract information from sensor data in spite of 'noise' caused by effects such as mechanical creep and adhesive characteristics. Further research and a large quantity of experimental data is required to establish whether this is true. A second surface used as a footplate which could have applications in podiatry or gait monitoring has been constructed using 9 FBG sensors. This was capable of being trained to distinguish left from right feet, different types of footwear being work by the same person, and different patterns of weight distribution over the area of the foot by a single user. These

parameters were detected with 99-100% accuracy. The use of FBG sensors in gait monitoring applications when compared with the infrared displacement sensors used in [47] has the advantage that a more compact system is feasible, with the possibility of a compliant mat construction as used in [155].

Chapter 5 - Low Cost Interrogation System for FBG Distributive Tactile Sensing System

5.1 Introduction

All the experiments in Chapters 3 and 4 were conducted using a broadband light source and an Optical Spectrum Analyser to interrogate the sensors. Both these items are very expensive. They are also physically large items and the data acquisition rate is low. In order for the distributive tactile sensing systems described to be used in medical or industrial settings a cheaper and more compact form of interrogation system is desirable. The system described here was implemented with my colleague Andrew Main and was presented at the 18th International Conference on Optical Fibre Sensors [157] in Cancun in October 2006. It builds on work described in [158] in which a low-cost system of identical chirped grating interrogation was devised, particularly aimed at the measurement of very large strains. That system used two identical chirped FBGs, one as a sensing grating and the other as a blocking or receiving grating, as shown in fig. 92. When the sensing grating was unstrained all the light reflected by the sensing grating was blocked by the receiving grating so no light reached photodetector D1. As the strain on the sensing grating was increased more light reached D1. D2 was used to compensate for any source fluctuations. A certain amount of temperature compensation was inherent in this system since an

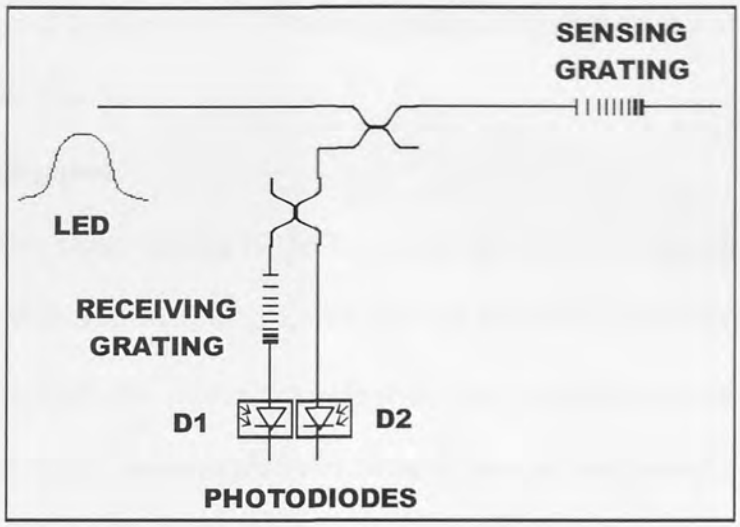

Fig. 92 CFBG interrogation system used in [158]

increase in temperature would cause the reflection spectra of both the sensing and the blocking grating to shift in wavelength simultaneously, provided (a) the thermal conditions for both sensors were the same and (b) assuming the source spectrum was flat over the wavelength range covered by the two FBG spectra. However the first of these conditions is unlikely to be true if this system were implemented in a practical sensing situation since the sensing grating would probably be mounted remotely from the blocking grating. Also the sensing grating would be bonded to the structure it was monitoring whereas the blocking grating would be mounted within the detection system. The amount of temperature induced spectral change experienced by the sensing grating would be dependent upon the thermal expansion of the structure and the bonding material as well as the air temperature (see 4.10.2). The system presented in this chapter has all the gratings mounted on the surface being monitored and thus has improved inherent temperature correction.

The system in [158] had one blocking grating per sensing grating, whereas in the system described here all the gratings both sense and block, so that the total number of gratings is halved. Also the extended system described in [158] used 8 optical couplers and 8 photodiodes to interrogate 4 sensing gratings. In our study only 4 optical couplers and 5

photodiodes are used to interrogate 7 sensing gratings, a further saving in terms of hardware and potential cost.

5.2. System Description

Seven Chirped fibre Bragg grating (CFBG) sensors, fabricated using a direct write system at 1554nm, each with a bandwidth of 1.5nm and 6db reflectivity were fixed to a stainless steel sheet. Each CFBG was written at an identical wavelength, but sensors which were required to reflect higher wavelengths were fixed to the steel surface while under strain. The mechanical arrangement was identical to that described in Chapter 4.11, so that the results are directly comparable. Principal Components Analysis (section 4.8) suggested that fewer than 9 sensors are necessary to extract all the information concerning a load on the surface, so 7 sensors were used in this case (fig 93).

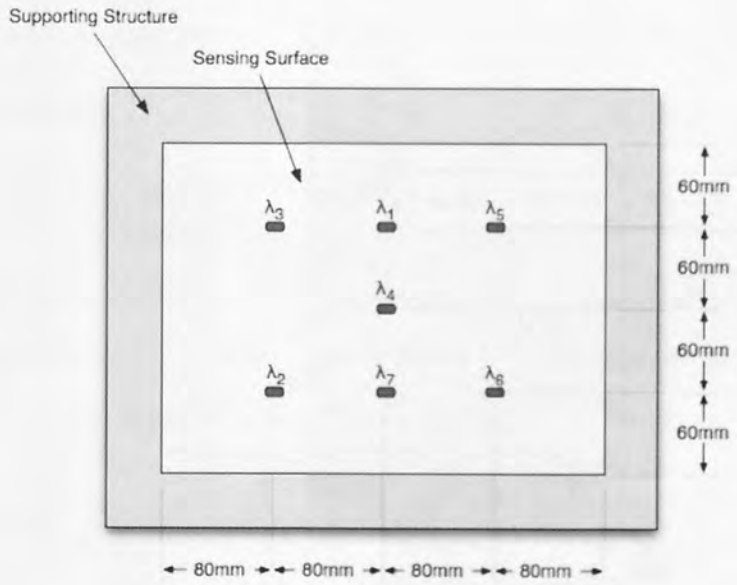

Fig. 93 Layout of sensors for low cost interrogation system

Five photodiodes were used to detect the light from the gratings, the photodiode output signals being encoded by a USB A to D data capture card (National Instruments NI-9201 DAC) which provided data to a PC running Labview (fig. 94). There was thus no wavelength interrogation, instead the power level of each output was measured. This has the advantage of having a much faster potential readout rate – a typical photodiode has a

response time faster than 1μs [179], so readings could be taken at a rate in excess of 1MHz.

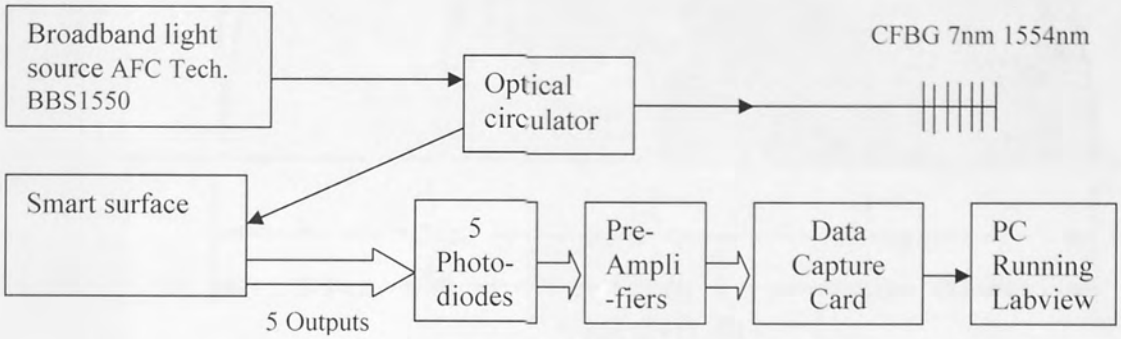

Fig. 94 Low cost interrogation system.

The light source for the smart surface (light reflected by a 7nm CFBG from a broadband light source) was chosen to represent approximately the output from a low cost multimode diode laser. The intention is to use the latter type of device in future systems in order to further lower the cost of the system.

5.3 Method of operation

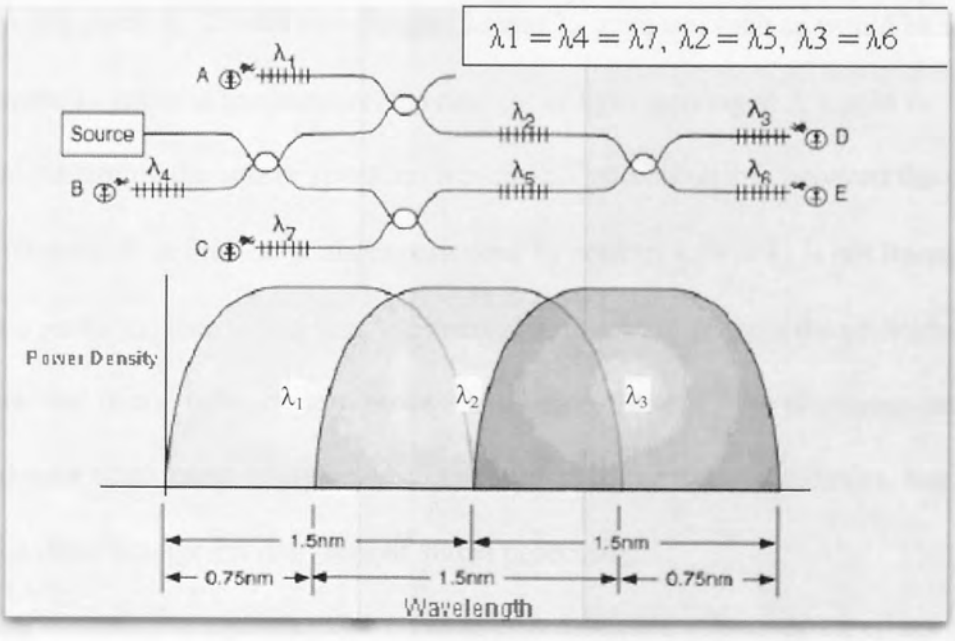

Fig. 95 Fibre Bragg grating sensing network based on overlapping chirped fibre Bragg gratings.

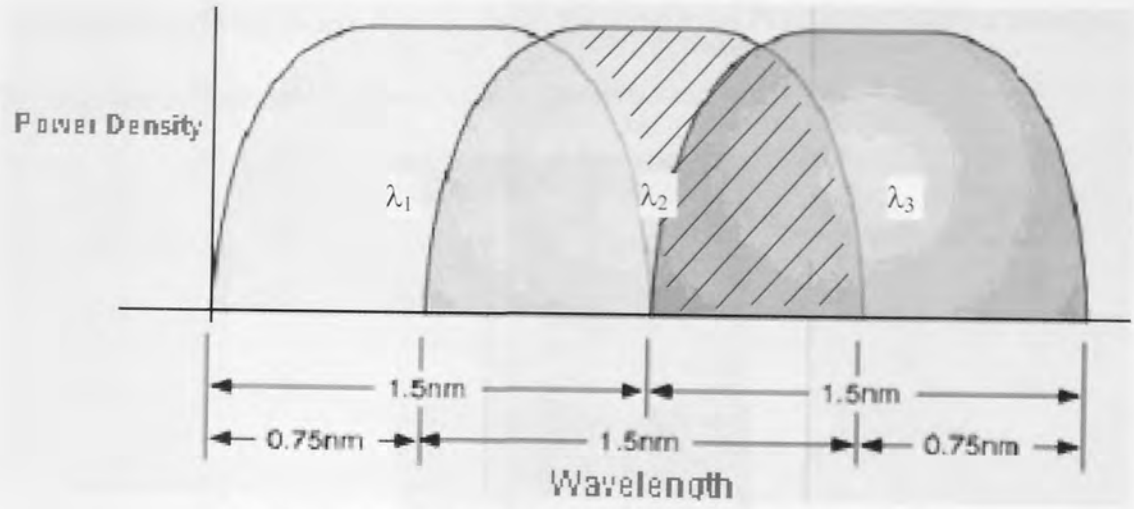

Fig. 96 Detail of fig. 95 showing overlapping spectra of chirped gratings

Consider sensors λ_1 and λ_2 in Fig. 95. When the surface is not loaded, light from the source is reflected by sensor λ_2 towards sensor λ_1. Some of the light is reflected back by sensor λ_1, but the remainder, equivalent to the spectral region shaded in fig 96 arrives at photodiode A. If sensor λ_1 only is strained, the wavelength λ_1 will increase so that the amount of light arriving at A will decrease. If sensor λ_2 only is strained wavelength λ_2 will increase and more light will reach A. If both wavelengths λ_1 and λ_2 increase, such as would be caused by an increase in ambient temperature, the amount of light arriving at A would be unchanged (assuming the source spectrum was flat). The relationship between the output signal of photodiode A and the strain experienced by sensors λ_1 and λ_2 is not linear, but this is not a problem since this system uses neural networks to process the photodiode output data, and neural networks can process and indeed benefit from nonlinear data. There is a high degree of cross-coupling between the outputs of the five photodiodes, but again this is not a disadvantage for this form of signal processing.

5.4 Testing

In order to verify the operation of the system two tests were performed; position sensing, and simultaneous recognition of shape and orientation. As in section 4.11, four steel blocks

were used, of different shapes but each with the same mass (1.6kg) and surface area (fig. 97). Only the cylindrical block was used for position sensing.

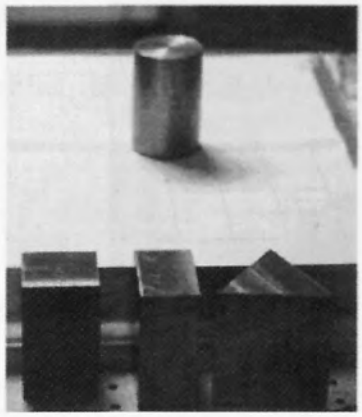

Fig. 97 Cylindrical block on smart surface

Neural networks with a range of numbers of hidden nodes were evaluated to establish which gave the best predictions in this application. Using a neural network with a single hidden layer of 49 nodes, an absolute position accuracy of 7.0mm (rms) was achieved. This is considerably better than the sensor spacing of 60 mm, and is also a significant improvement over the system used in 4.10, which achieved an accuracy of 11 mm (rms). The distribution of position error (mm) as a function of position can be seen in Fig. 98.

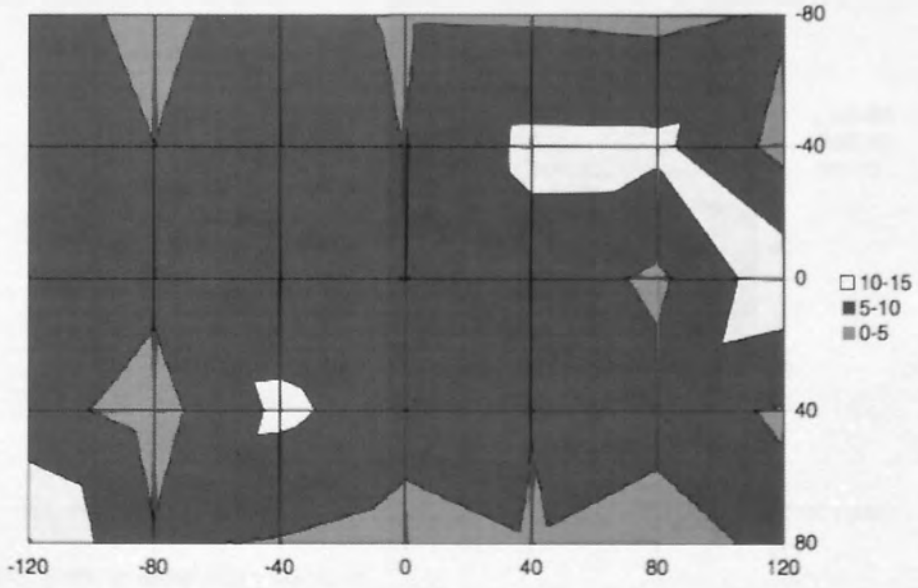

Fig. 98 Distribution of error (mm) on surface

For the shape recognition the objects were each placed at the centre of the surface. It was found that by using parallel trained neural networks (see 4.11.3) it was possible to simultaneously identify the shape (square, circle, triangle or rectangle) with 100% accuracy, and detect the orientation to within 7 degrees for the square, triangular and rectangular objects.

5.5 Stability Verification

It is important to establish how immune to external influences this system is. The two most significant of these are ambient temperature fluctuations and variations in source power.

5.5.1 Ambient temperature fluctuations

The position test was repeated at different times with different ambient temperatures over a range of 5°C. The retrained network returned a resolution of 23.4mm (rms) when exposed to ambient temperature changes of 5°C. The distribution of position error (mm) as a function of position can be seen in Fig.99.

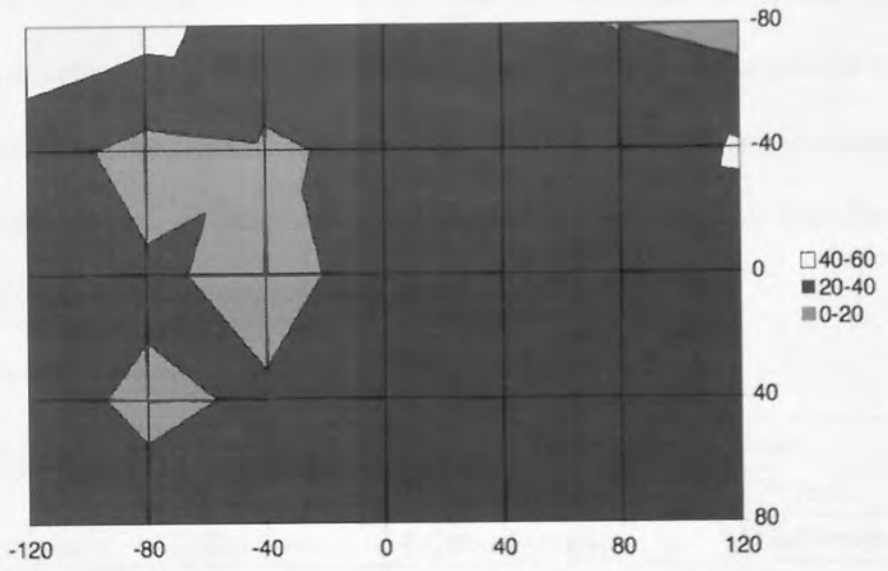

Fig. 99 Distribution of position error with ambient temperature fluctuations (mm)

5.5.2 Source Power level fluctuations

The effect of source power fluctuations is particularly important, since susceptibility to such variations is a common problem with intensity based optical interrogation schemes.

The same neural network as used in 5.4 (49 hidden nodes) was retrained using sensor data obtained with source power fluctuations of in excess of 50%. The position error obtained under these circumstances was 27.4mm (rms). The distribution of position error (mm) as a function of position for this case can be seen in Fig. 100

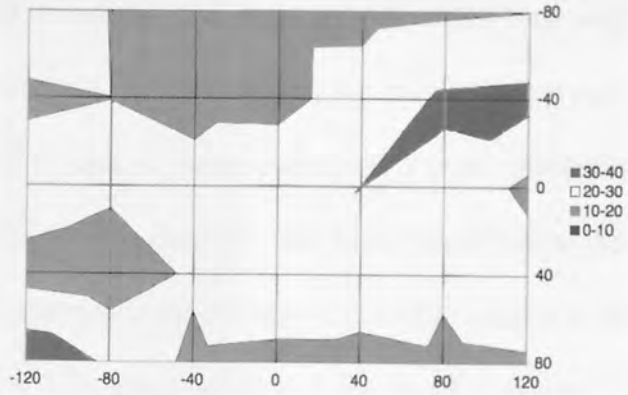

Fig. 100 Distribution of position error with source power fluctuations. (mm)

This represents a 3 to 4 fold deterioration in the accuracy of position detection, but is still much smaller than the inter-sensor spacing (60mm, fig. 93). This work is not yet complete and further work is necessary to optimise and train the neural network to deal with these effects. It is expected that a greater amount of training data recorded at a wider range of source output power and ambient temperatures, and a more comprehensive assessment of different neural network architectures would yield improved accuracy. Significant improvements upon these results are anticipated.

5.6 Comparative costing

Laboratory Interrogation system		Low Cost Interrogation system	
OSA	£20,000	5 Photodiodes	£15 each
1 optical coupler	£22 (Newport)	4 Optical couplers	£88 (Newport)
		1 Optical circulator	£633 (Newport)
		5 Preamplifiers	£10 each
USB GPIB card	£200[159,160]	USB DAC card	£100
Light Source	£3000	Multimode Diode laser	£200
TOTAL:	£23,222	TOTAL:	£1,146

TABLE 13: Comparative costs of interrogation systems

Table 13 shows a price comparison between this system and the one used in Chapters 3 and 4.

The optical circulator used in this study was used to increase the signal levels available at the photodiodes. It was not strictly necessary, and was responsible for most of the cost in the low-cost system. If it was replaced by an optical coupler this would decrease the total for the low-cost system to £413. It is clear that the costs of this system are much lower than the previous laboratory system. It is also considerably more physically compact. Another advantage of this system is its scalability – the total optical bandwidth occupied by the seven sensors is 3nm, whereas in the system described in chapter 4 nine sensors occupied 34nm. (fig.59 in section 4.5). It is possible to fabricate FBG sensors with narrower spectral peaks than those in chapter 4 (0.5nm is typical), but they still need to be spaced more than 1nm apart because the wavelength shift of one sensor under strain (for a strain of 870με) would be 1nm, and the spectral peaks of each individual sensor should not overlap each other significantly because the peak detection algorithm could then misinterpret the spectra. Thus 7 sensors written at different wavelengths will occupy at least 10.5nm of bandwidth (1.5nm per sensor). Scaling the system up to use more sensors would result in a linearly increasing bandwidth (and would require an increasingly sophisticated and expensive light source) However with the low cost system this need not be the case, since the 3 wavelengths used with the 7 sensors in this arrangement can be reused with other sensors, while the number of photodiodes increases linearly.

This system also has an inherent speed advantage over an optical spectrum analyser, which sweeps the required spectral width, analysing the optical power density in each discrete wavelength band. InGaAs photodiodes have response times of 1μs or better [179] and neural networks, once trained, are very simple algorithms and could be implemented, for

example, in a Field-Programmable Gate Array running at a speed of 50MHz. This arrangement could potentially have a response speed of a few microseconds or less.

5.7 Summary

A low cost arrangement of CFBG sensors has been demonstrated, in which seven gratings were used, with some gratings filtering the light reflected from one or more of the other gratings. The signals from photodiodes monitoring the filtered, reflected light were successfully used to train neural networks to recognise the position, shape and orientation of a load on the sensing surface. The accuracy of this system was comparable to or better than the arrangement used in Chapter 4. The cost of this arrangement was £1,146 (£413 without the optical circulator) compared with an estimated £23,222 for the conventional laboratory system (2008 prices).

Further work is needed to optimise the grating placements in order to improve the accuracy of the system and to find the optimum neural network architecture to improve the system's insensitivity to ambient temperature changes. The use of a cheaper light source (such as a multimode diode laser) is under investigation in order to achieve the costings in Table 13. It is particularly important that improved insensitivity to source intensity fluctuations be realised, and to this end a flatter source spectrum, possibly shaped by a grating, may be helpful.

Chapter 6 - Surface profile sensing using FBG sensors

6.1 Introduction

The artificial sensing of surface profile (or surface texture) is of great interest to industries such as road surfacing, [161, 162] textiles and abrasives, and in the area of machined finishes, as well as having potential applications in minimally invasive surgery. Fine surface finish information for machined surfaces (on the scale of 0.2 – 5 μm)[163] is commonly measured using optical methods such as interferometry. Larger surface details (0.1 – 5mm) are not easily characterised in this way. The human finger is a very good sensor of surface texture on this scale, using structures called Pacinan corpuscles and Meissner corpuscles for this purpose (as discussed in chapter 2.2). Attempts to emulate the human system have used polyvinylidene fluoride films [164,165] vertical sampling pressure probes, [166] strain gauges [167] two accelerometers and a force sensor [168] and a piezoelectric microphone [169]. Many tactile sensors capable of detecting small scale profile details consist of arrays of many sensors, which present problems in terms of connection for information retrieval and require computationally intensive signal processing. Holweg and Jongkind [34] used a 256 element tactile sensor array with neural network processing to detect the shape of a contacting object approximately 10mm in width.

Some of the sensor types described above are either too large, expensive, slow or complex to be suitable for applications such as minimally invasive surgery. Some are unable to

withstand the medical requirement of being sterilised. The sensor described in this chapter has one embedded Fibre Bragg Grating sensing element with a single optical fibre connection. In addition to the advantages of reduced connectivity requirements, it requires no electrical power at the sensor point and is immune to electromagnetic interference which would be advantageous in many environments. The experimental work described here aimed to establish whether this sensor could function as a tactile sensor to detect a pattern of 1mm ridges in a profile block, and if so whether it could also distinguish between different shaped 1mm ridges. A second aim was to establish whether changing the length of the grating used in the sensor had any effect on the sensing achieved. Both static and dynamic tests were performed.

This work was conducted in collaboration with Dr Tom Allsop and Dr John Williams, and was presented at the SPIE Europe International Congress on Optics and Optoelectronics, 16 - 19 April 2007, Prague [170]. It is also the subject of a patent application [171].

6.2 Preliminary work with Long Period Grating sensors.

Long period gratings were considered as the first choice of sensor type for this work, because it was considered that small-scale bending would be taking place in response to surface profile changes. LPGs are generally more sensitive to bending than FBGs (section 4.4). LPGs in progressive three-layered fibre are insensitive to the refractive index of the medium surrounding them [172] and it was expected that the refractive index of the silicone rubber encapsulation material might not have been homogenous. Such inhomogeneity surrounding a normal LPG may have caused the spectral peaks to become distorted and made interpreting the sensor spectral response more difficult.

A long period grating (LPG) sensor was embedded in a circular domed Poly Siloxane polymer (Methyl Vinyl Silicone rubber) silicone pad approximately 120mm in diameter

and 8mm in height (fig 101). The fibre used was supplied by Fibrecore Ltd [173], its specification is shown in table 14.

Layer	Refractive index	Thermal Expansion Coeff (C^{-1})	Strain-optic Coeff	Thermo-op tic Coeff (C^{-1})	Radius (m)	Material composition
Core	n1= 1.4555	$4.1x10^{-7}$	0.27	7.98x10-6	2.5x10-6	GeO_2 /SiO_2
inner cladding	n2=1.4438	$6.5x10^{-7}$	0.24	9.4x10-6	45.0x10-6	SiO_2
outer cladding	n3=1.4143	$2.5x10^{-7}$	0.23	8.7x10-6	62.5x10-6	$SiO_2/F/P_2O_5$

TABLE 14 Typical parameters of fibre used to make LPGs (data supplied by Fibrecore Ltd).

The fibre was hydrogenated at a pressure of 120bar at room temperature for a week, and fabricated using a FreD Argon Ion laser (244nm) (spot size ~10microns) using a point by point technique. The total exposure time for each grating was 15s and the laser power was 80mW.

Two sensors were made using different LPGs but the same encapsulation technique:

AV12 - Length 59.60 mm, period 387microns, power 80mW, Velocity 0.24 mm/second.

AV5 - Length 66.85 mm, period 382microns, power 80mW, Velocity 0.23mm/second.

Embedding the sensor in silicone both protected the fibre from mechanical damage and provided a flexible medium through which the stresses due to the variations in surface profile could be transmitted to the fibre. The embedding of the sensors was done by Matthew Fisher of Aerovac Systems Ltd, Keighley [174].

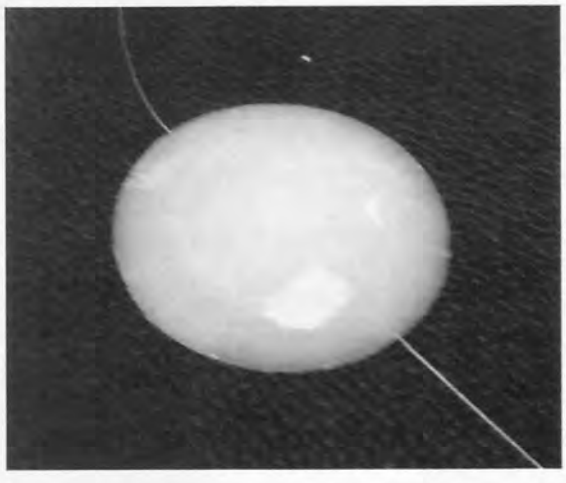

Fig. 101 Sensor embedded in polymer

In order to establish whether these silicon-embedded sensors exhibited any tactile sensitivity, some basic tests were conducted to discover whether the wavelengths of their attenuation bands changed in response to the magnitude or angle of an applied load.

6.2.1 Response to load

The LPG (AV12) transmission characteristic had an attenuation feature (cladding mode resonance) at 1490nm. A load was applied perpendicular to the base of the sensor (see fig 102). The wavelength of the attenuation feature was recorded for various values of load.

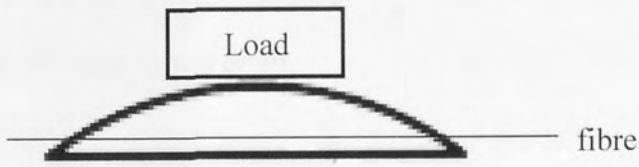

Fig. 102 sensor under load

It was found that the wavelength of the attenuation feature increased with the applied load (fig. 103).

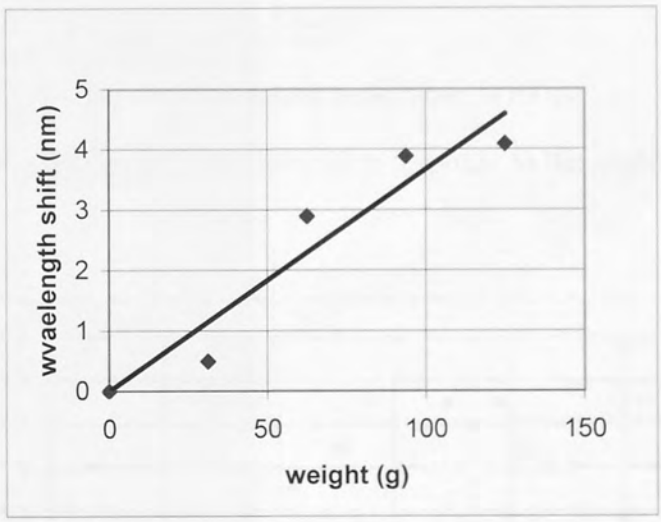

Fig. 103 Wavelength sensitivity to load magnitude of attenuation feature of LPG AV12

6.2.2 Response to angle of applied load (tilt test)

Sensor AV5 had an attenuation feature at 1430nm (fig 104).

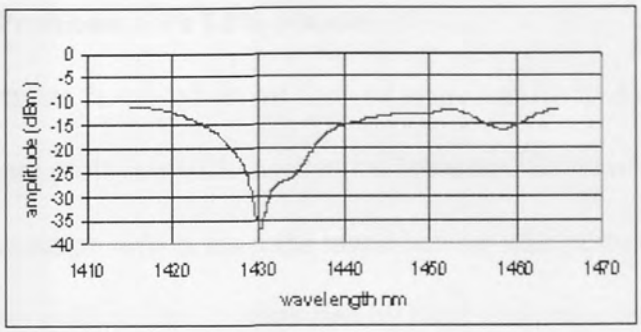

Fig.104 Attenuation feature of LPG AV5 at 1480nm (unloaded)

A rectangular block (mass 336.9g, length 155mm) was placed on the sensor, perpendicular to the axis of the fibre, and its angle was changed by adjusting a depth gauge (fig 105). The block was horizontal when distance h was 8mm.

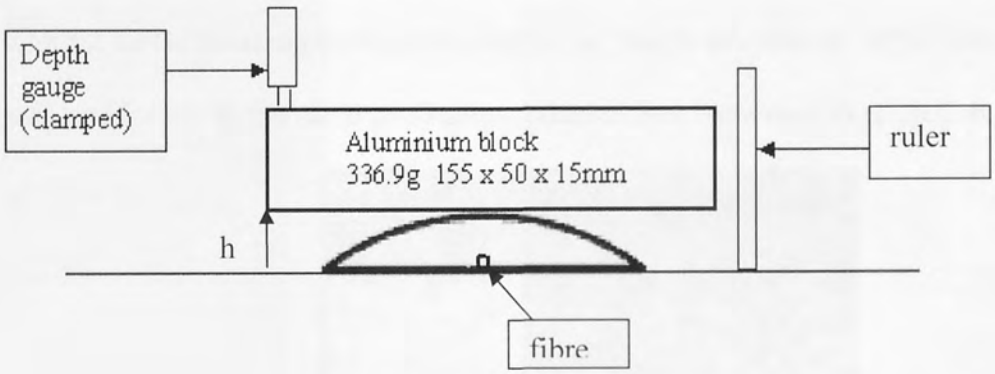

Fig. 105 Experimental arrangement for tilt test

The wavelength of the feature at 1430 changed in response to the angle of the load (fig106):

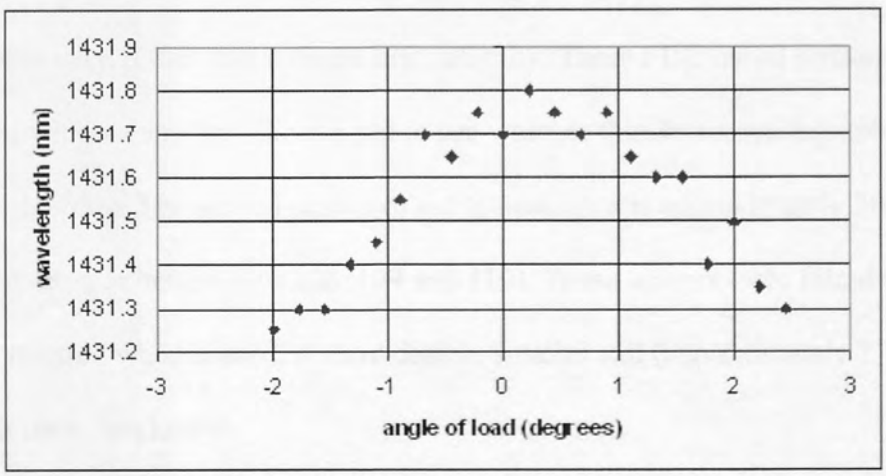

Fig.106 Response of LPGAV5 attenuation feature to load angle

6.2.3 Mechanical Problems with LPG sensors

Although the LPG sensors described above showed some sensitivity to load magnitude and angle, there were severe problems with mechanical breakage. Some of the sensors were found to be discontinuous on arrival from the manufacturer who performed the embedding, although they had been collected and transported by hand and protected well in transit. Others broke while under no stress in the laboratory. It was deduced that the stresses which develop within the silicone during curing are sufficient to fracture the uncoated fibre. Fig 107 shows the location of such a fracture, which appeared as a glowing area when light from a helium neon laser (at 633nm) was directed along the fibre. Because of the problems with the LPGs breaking during manufacture or shortly afterwards, some FBGs were assessed for use in the same application, since if they were used in reflection, they would

Fig. 107 Broken LPG with Helium Neon laser showing position of fracture.

still be useable even if they had a single discontinuity. These FBG based sensors were encapsulated within a smaller silicone pad to see whether this decreased the stresses imposed on the fibre. The second design of encapsulation was approximately 50mm in diameter and 6mm in height (figs 108, 109 and 110). These sensors were found to be intact and did not fracture when loaded. A third design, smaller still (approximately 25mm diameter), is under evaluation.

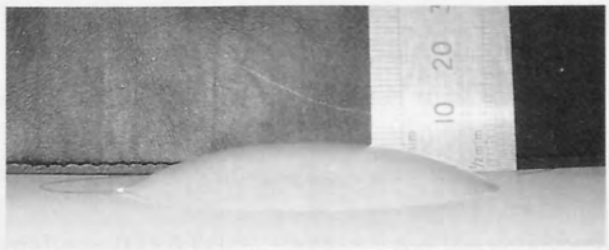

Fig. 108 Sensor with smaller encapsulation design, side view.

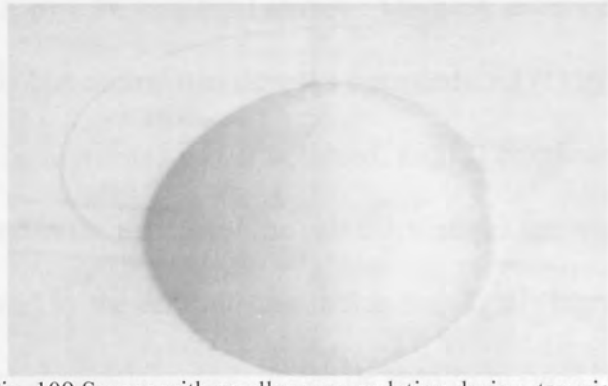

Fig. 109 Sensor with smaller encapsulation design, top view

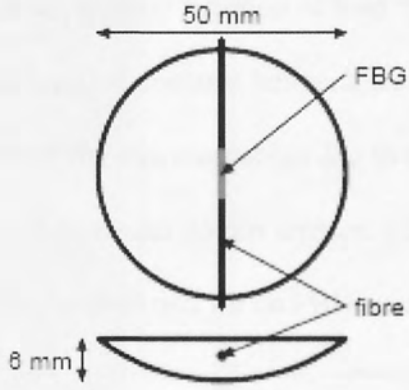

Fig. 110 Dimensions of smaller sensor.

6.3 Tests using FBG based sensors

Three FBGs were fabricated in standard single mode optical fibre, previously hydrogenated (at 120bar at room temperature for a week), using a 244nm Argon Ion laser and a phase mask. FBGs of lengths 2.5mm, 10mm and 25mm were fabricated, at a laser power of 92mW and speeds of 0.01mm/s, 0.25mm/s and. 0.75mm/s respectively. The inscription wavelength was approximately 1545nm. After fabrication they were annealed at 80°C for 24 hours before encapsulation in the polymer.

6.3.1 Load Test

Various loads were applied to the centre of the 10mm sensor, perpendicular to its base. The sensor was interrogated using a broadband light source (AFC Technologies BBS 1550) and an Optical Spectrum Analyser (OSA) (HP 70004A) and the reflected spectrum was recorded from the OSA by a PC running Labview. The peak reflected wavelength was recorded for each load. The central wavelengths were deduced (1) by simply recording the wavelength at which the maximum power occurred, and (2) calculating the centroid of the spectral peak. The trend in the results for the two calculations was very similar, although the wavelengths returned by the centroid calculation are slightly higher, reflecting the asymmetry of the spectral peak (fig. 112). It can be seen from fig. 111 that the strain experienced by the grating was not a linear function of load. Since the response of an FBG to strain is linear (in the elastic limit) at constant temperature [175], this must be due to nonlinearity in the compression of the silicone rubber due to the device geometry. Similar results were recorded using the 2.5mm and 25mm sensors. Comparing these results with those for the LPG sensors, it can be seen that for an FBG sensor, 100g gave a wavelength

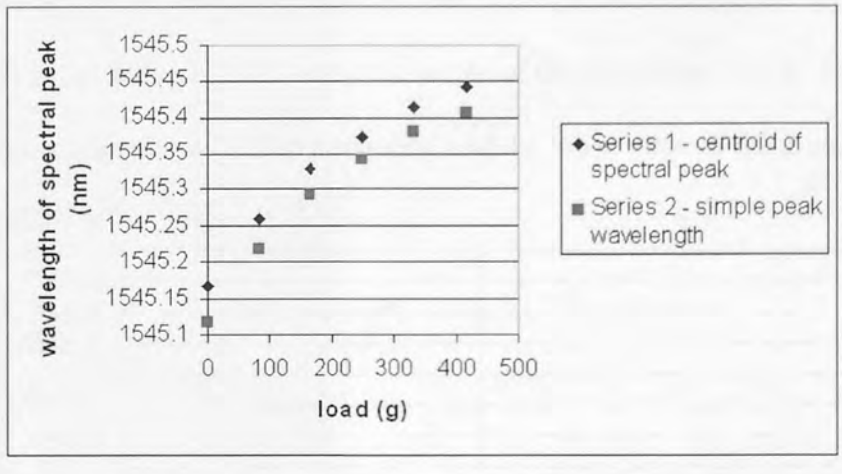

Fig. 111. Peak wavelength vs. load for 10mm sensor.

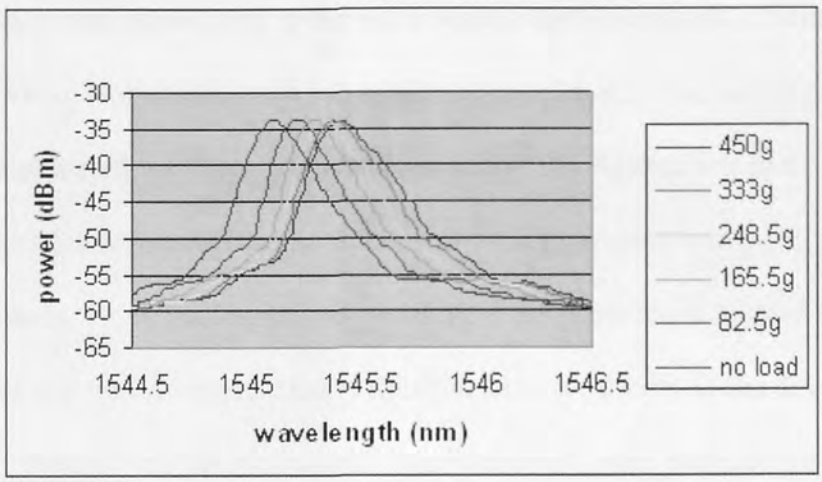

Fig. 112. Reflected Spectrum from FBG sensor under different loads

change of approximately 0.1nm (fig. 111), whereas the LPG sensor in section 6.2.1 (1490nm attenuation band) gave a wavelength change of approximately 3.5nm, so the LPG was 35 times more sensitive to load magnitude. However because the LPG attenuation feature has a much greater spectral width than the FBG, it is not possible to measure its central wavelength with as great a precision as the FBG spectral peak.

6.3.2 Tilt Test

Next the 10mm sensor was subjected to a constant load of 3.37N at different angles in a plane perpendicular to the axis of the optical fibre. The apparatus shown in fig. 106 was used, the depth gauge being used to adjust the angle of the aluminium block. The tilt angle was defined as the angle between the horizontal and the lower edge of the aluminium

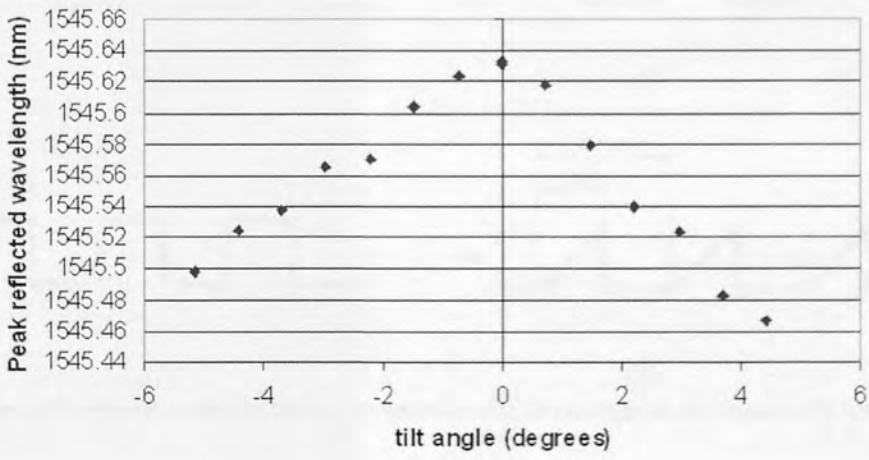

Fig. 113 Reflected wavelength vs. tilt angle for 10mm sensor

block. The sensor was interrogated in the same way as for the load test. The centroid of the spectral peak was calculated for each value of load. (see 2.5.8.2) The relationship between load angle and reflected wavelength can be seen in fig. 113 Asymmetry in the response could be due to inhomogeneities in the silicone rubber or experimental inaccuracies, particularly uncertainty in reading the height of the edge of the block (shown as h in fig. 106). Both load and tilt test results clearly illustrated the sensitivity of the device to the magnitude and direction of the applied load. Similar results were recorded for the 2.5mm and 25mm sensors. A comparison with the LPG sensor used in 6.2.2 showed a maximum wavelength change during the tilt test of approximately 550pm for 2 degrees tilt. The equivalent value for the FBG sensor was approximately 150pm for 4 degrees tilt, so the LPG sensor was 7 times more sensitive to load angle. However because of the mechanical problems with the LPG sensors described earlier the decision was made to continue using FBGs for the remainder of this work, and if the sensors showed promise as surface profile detectors further LPG based sensors could be manufactured and evaluated at a later stage.

6.3.3 Surface profile detection

Four different surface profile blocks were machined from aluminium to provide a repeating

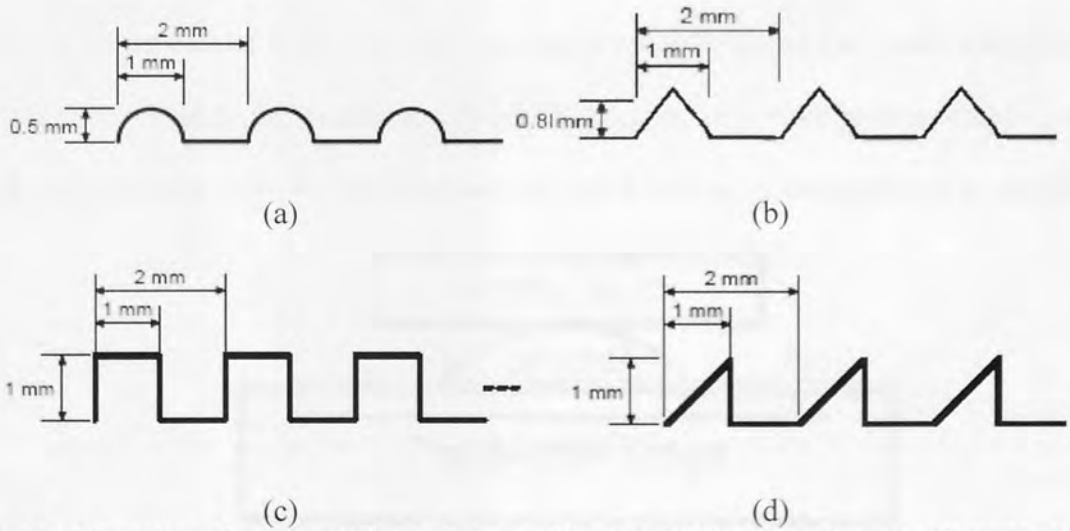

Fig. 114 Dimensions of surface profile blocks (a) semicircular, (b) triangular, (c) square, (d) sawtooth

pattern of ridges with a modulation depth of 1 mm and a period of 2 mm. The cross sectional shapes of the ridges were semicircular, triangular, square and sawtooth (see figs 114,115).

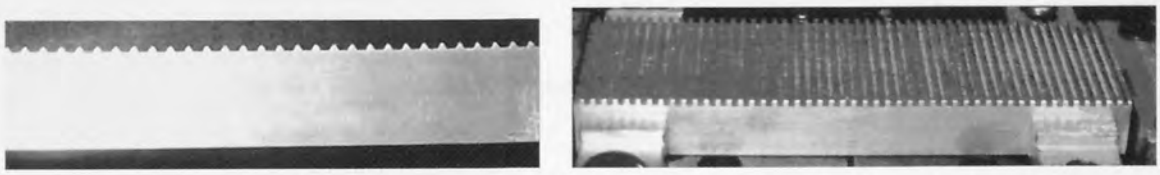

Fig. 115 Edge of triangular profile block (right), square profile block (left).

The sensor was mounted on a manually driven translation stage. A profile block was mounted on a framework above the translation stage so that the sensor made contact with the profile block as it moved beneath it (fig.116, 117). The blocks were mounted with the

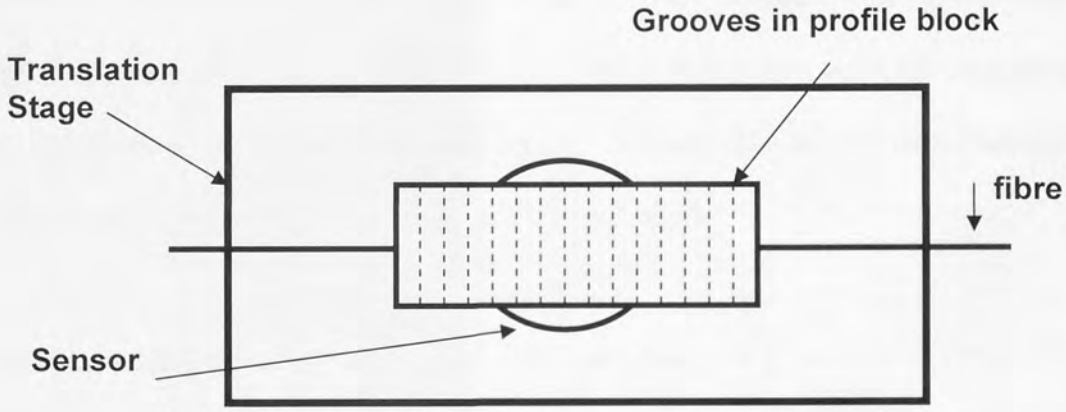

Fig. 116 Arrangement of sensor and block on translation stage, top view

grooves perpendicular to the fibre axis because it was considered that small-scale bending of the fibre would be the mechanism by which detection of surface profile would occur, and this could not happen if the block was mounted with its grooves parallel to the fibre.

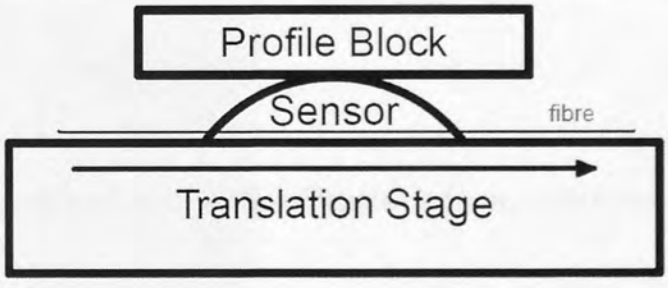

Fig. 117 Arrangement of sensor and block on translation stage, side view

The sawtooth block was used in two directions, designated sharp and blunt (see fig 118)

Fig 118 Sawtooth block showing 'sharp' and 'blunt' directions.

The position of the profile block was adjusted so that it was as horizontal as possible and so that the pressure between the block and the sensor caused the wavelength of the reflected peak to increase by 0.3nm compared with its unloaded value. The same initial pressure was used for each profile block and for every test performed to maintain consistency. The reflected spectrum from the sensor was recorded over a 6mm (3 period) range at intervals of 0.1mm or 0.2mm using a broadband light source (AFC Technologies BBS 1550) and an optical spectrum analyser (HP 70004A). The spectra were characterised by their centroid wavelengths and their rms spectral width.

$$\text{Centroid wavelength} = \lambda_c = \frac{\sum_0^n \lambda_j i_j}{\sum_0^n i_j} \qquad [87] \quad \text{see also 2.5.8.2}$$

where ij and λj represent the intensity and the centre wavelength of the jth spectral component respectively, λ_c is the centroid wavelength and n is the number of spectral components.

$$\text{Rms Spectral width} = \sqrt{\frac{\sum_{j=0}^{n} (\lambda_j - \lambda_c)^2 i_j}{\sum_{j=0}^{n} i_j}}$$

Three sensors were evaluated, with FBGs of lengths 2.5mm, 10mm and 25mm, respectively.

6.3.4 Results of surface profile detection

The square profile gave no perceptible periodic response using any of the sensors, possibly because the recesses in the profile were smaller (1mm wide) than those in the other profiles, so that the silicone was less able to deform into the recesses. Results for that profile are therefore not shown.

6.3.4.1. Sensor with 10mm grating

The changes in central wavelength and the spectral width were plotted against the position for the various surface profiles. The results for the triangular (fig. 119), semicircular (figs.120, 121) and sawtooth (sharp and blunt, figs. 122 and 123) profiles are shown below:

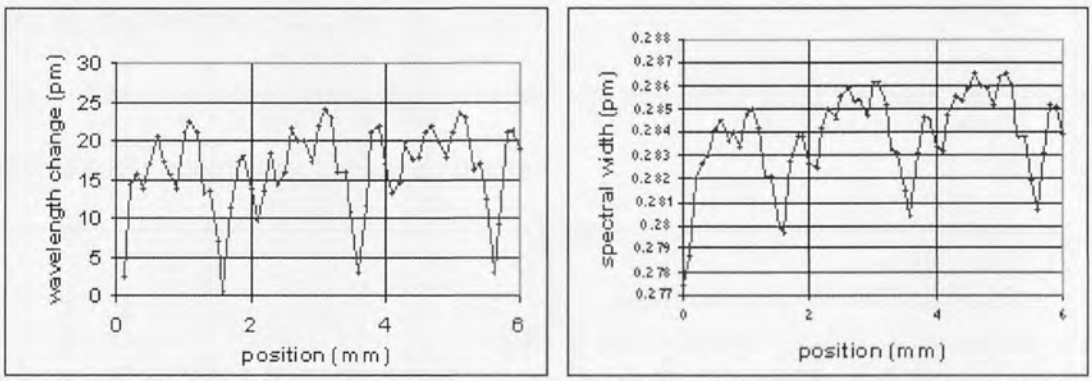

Fig. 119 Centroid wavelength shift (left), spectral width (right) vs. position for 3 periods of the triangular profile block, 10mm grating.

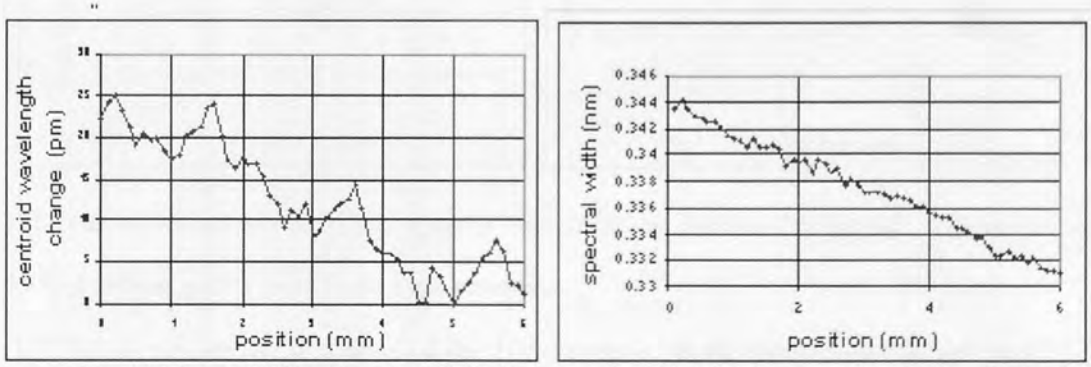

Fig. 120 Centroid Wavelength shift (left), Spectral width (right) vs. position for 3 periods of the semicircular profile block, 10mm grating

The results shown in figs. 119 and 120 show clear periodic variations with the same period (2mm) as the profile block passing over the sensor. The relationship between sensor output and position for the two different shapes of profile block is markedly different, showing

that this sensor seems to be able to distinguish in some way that the profile shapes are not the same. The distinct downward trend seen in fig. 120 (semicircular profile) occurred because the profile block was not precisely horizontal, so as the sensor was traversed beneath the block the stress gradually increased on the sensor. Also there may have been some drift due to ambient temperature changes, although the sensor was encapsulated in silicone polymer, which is a good insulator, and was in contact with the translation stage, which was heavy and made of steel, so would not be expected to change temperature quickly. The wavelength-temperature sensitivity of silica fibre at 1550nm is 13 pm/°C [61], so the estimated worst case drift due to a 2 deg C change in ambient temperature during the duration of an experiment is 26pm.

In each of the following graphs (fig. 121 onwards) any linear trend has been removed by mathematically subtracting the linear function:

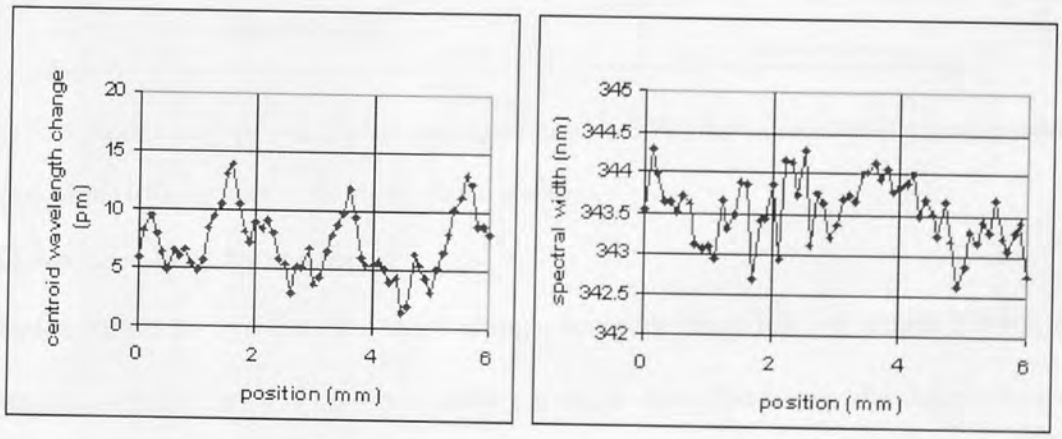

Fig. 121 Centroid Wavelength shift (left), Spectral width (right) vs. position for 3 periods of the semicircular profile block, 10mm grating (with linear trend removed)

Fig. 122 below shows the response of the 10mm sensor to the Sawtooth (sharp) profile. Again the response differs from the responses for the other shapes. Fig. 123, which shows the response for the sawtooth (blunt) profile, has a less clear periodic variation.

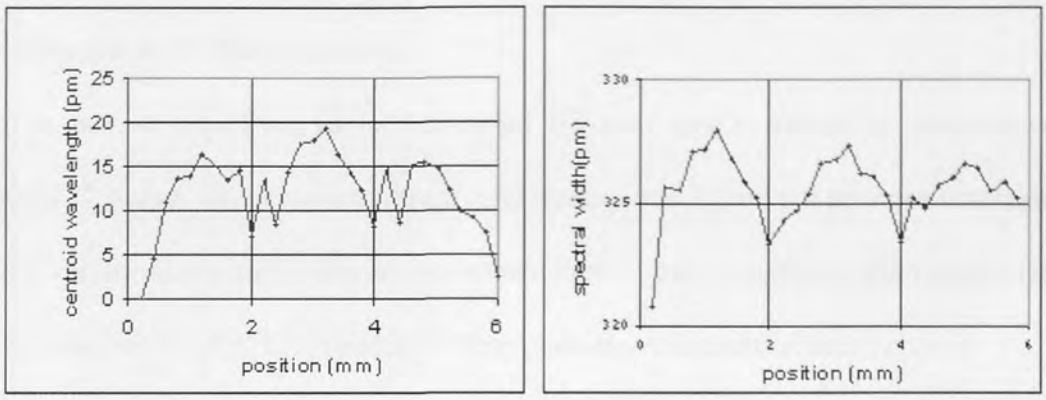

Fig. 122 Spectral characteristics vs. displacement for sawtooth profile (sharp) centroid wavelength shift (left), spectral width (right) for 10mm grating (linear trend removed).

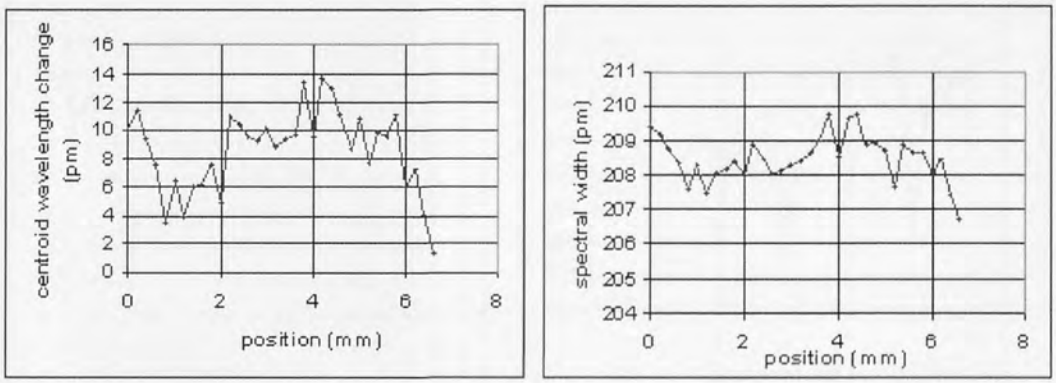

Fig. 123 Spectral characteristics vs. displacement for sawtooth profile (blunt) (linear trend removed) centroid wavelength shift (left), Spectral width (right), 10mm grating.

6.3.4.2 Sensor with 2.5mm grating

The results shown in fig. 124 were taken using a sensor with an FBG of length 2.5mm and the triangular profile block. The other profiles studied using this sensor did not produce a clear periodic variation so the results are not reproduced here.

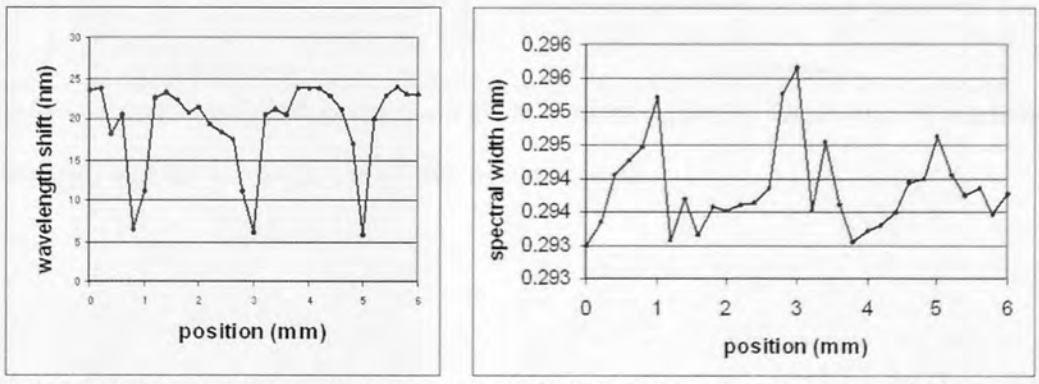

Fig. 124 Spectral characteristics vs. displacement for (left) Centroid wavelength change and (right) rms width for triangular profile block, 10mm grating.

6.3.4.3 Sensor with 25mm grating

A third sensor, with a 25mm sensor embedded in it, was used to obtain the results shown in figs 125-127 below. The sawtooth (blunt) and square profiles did not produce noticeably periodic variations, so the results are not shown here. It can be seen that the triangle (fig. 125) and semicircle (fig. 126) produced clear periodic variations of both centroid wavelength and spectral width with position, the sawtooth (sharp) profile (fig. 127) was less clear.

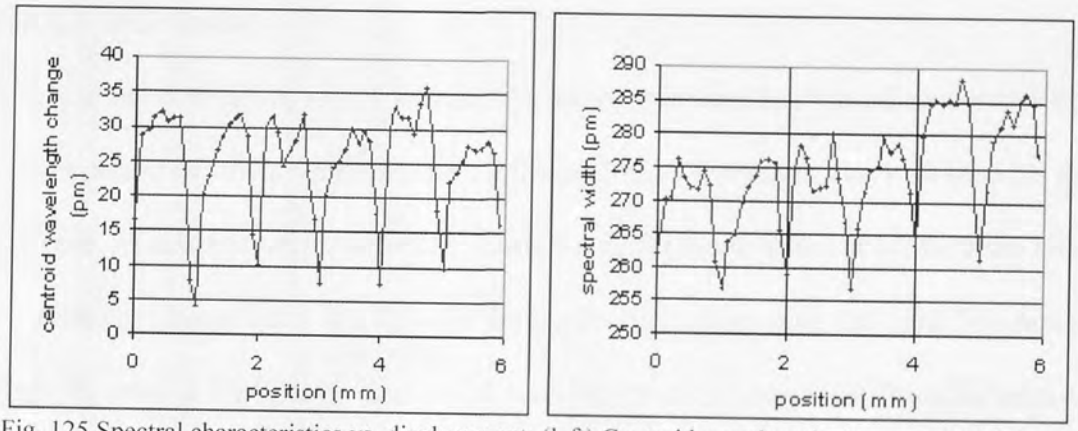

Fig. 125 Spectral characteristics vs. displacement: (left) Centroid wavelength change and (right) rms spectral width for the triangular profile, 25mm sensor.

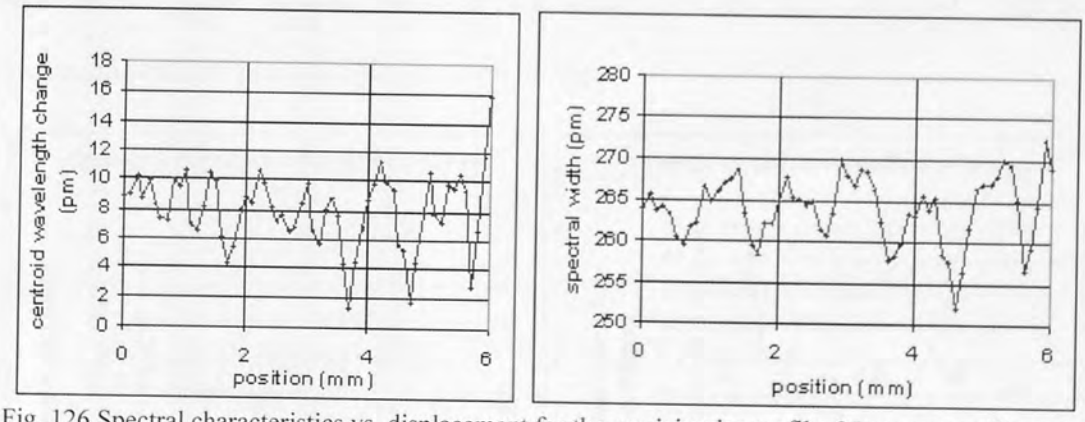

Fig. 126 Spectral characteristics vs. displacement for the semicircular profile, 25mm sensor (linear trend removed): (left) centroid wavelength change and (right) rms width.

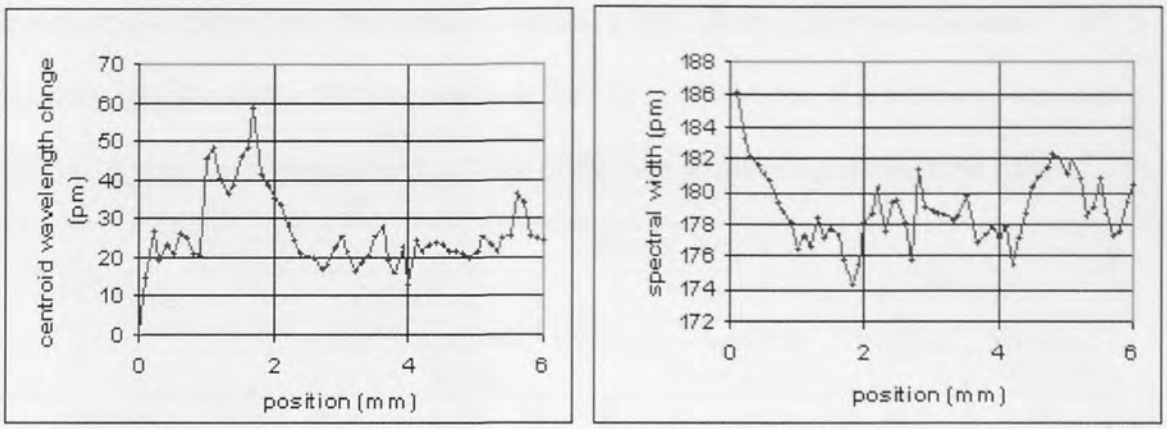

Fig. 127 Spectral characteristics vs. displacement for the sawtooth (sharp) profile, 25mm sensor (linear trend removed) (left) centroid wavelength change and (right) rms width.

6.3.4.4 Noise levels

Because the changes in sensor wavelength above were small, a typical sensor was observed over a period of 150 seconds, recording the centroid wavelength every 10 seconds to check the level of ambient noise. After correcting for drift (due to ambient temperature changes) by plotting a linear trend line through the results then subtracting the trend line function from the results, the change in centroid wavelength due to noise was found to have a peak value of 1.7pm and an rms value of 0.8pm (fig. 128, left). The change in spectral width due to noise had a peak value of 0.6pm and rms value of 0.3pm (fig.128, right). These values are much smaller than the changes seen above.

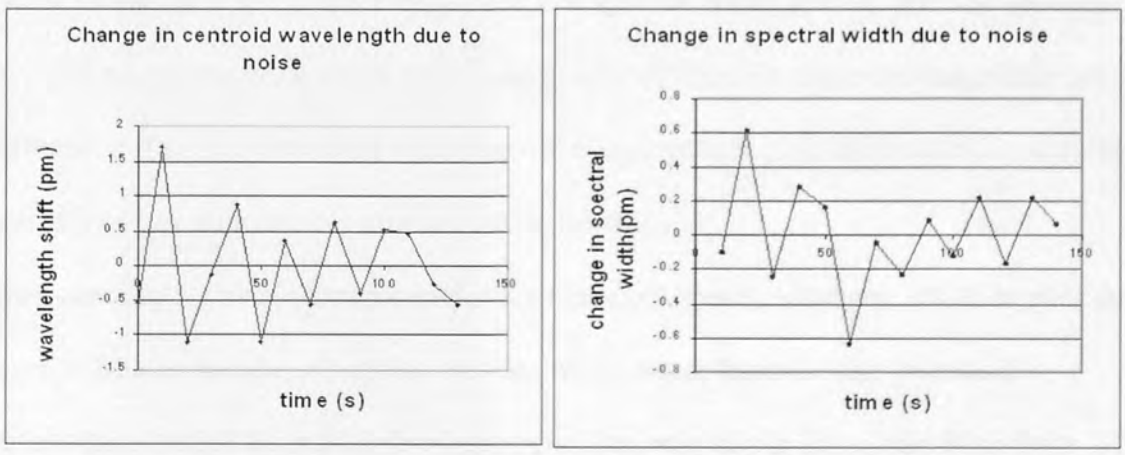

Fig. 128 Changes in spectral characteristics vs. time: centroid wavelength (left), spectral width (right).

To sum up the results from the 3 different sensors, the 2.5mm sensor was the least sensitive, only showing a periodic response for one profile shape. The other two sensors exhibited a periodic response for 3 or 4 out of the five profile shapes (see table 15).

Profile shape	Sensor length					
	2.5mm		10mm		25mm	
	Centroid	Spectral Width	Centroid	Spectral Width	Centroid	Spectral Width
square	n	n	n	n	n	n
triangle	y	y	y	y	y	y
semicircle	n	n	y	?	y	y
Sawtooth sharp	n	n	y	y	y	y
Sawtooth blunt	n	n	Y	?	n	n

TABLE 15 Summary of surface profile detection: y=definite periodic response, n=none, ?=questionable.

6.3.4.5 Conclusions

When the polymer is pressed into contact with the surface to be measured, its elastic properties convert deformation due to protruding surface features into internal strain resulting in variation in the distributed strain along the FBG and hence into changes in its reflected spectrum. Thus the characterisation of how the spectrum varies as the sensor is translated past a rough surface provides a measurement of surface roughness.

For some surface profiles a clear periodicity corresponding to the periodicity in the surface profile is seen in both the wavelength shift and spectral width, and the periodic spectral changes measured versus displacement are clearly different in shape and magnitude for the different surface profiles. Thus these spectral measurements give information concerning both the feature size and the shape of the surface.

There are also harmonic components in the measured spectral changes, which implies that it might be able to measure surface profiles with smaller features than have been demonstrated using the machined blocks here. However this is not certain from these experiments since the results using the square profile block (which had smaller recesses between the surface features) were not periodic. More work is required in this area.

There was a trend in both centroid wavelength shift and spectral width changes for a longer grating to produce a greater response (fig. 129), although the spectral width changes exhibited this phenomenon to a greater extent than the centroid wavelength changes. More experimental work involving sensors with a larger range of grating lengths is required to confirm these results.

A longer fibre Bragg grating usually has a narrower bandwidth and thus can be used to measure more sensitively changes in the spectrum and thus smaller changes in strain. However, being of larger extent may mean that spatial resolution may be lost since the spectral characteristics are effectively being integrated across its whole length. For the 25mm sensor the grating length is 12.5 times longer than the surface profile period being measured yet it is possible to observe a periodicity in the spectral characteristics. The optimum design of these sensors must take account of the physical characteristics of the polymer cap as well as the response of an FBG to a complex distributed strain.

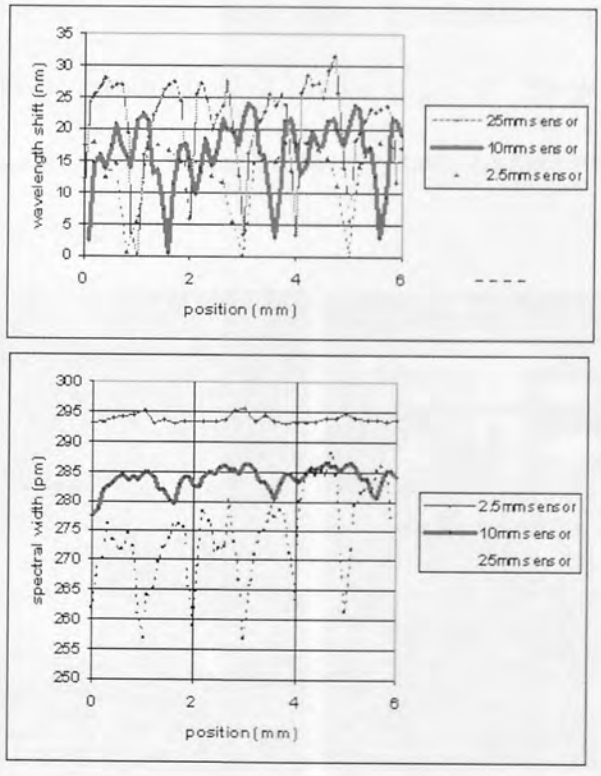

Fig. 129 Spectral changes when using the triangular profile, centroid wavelength (top), spectral width (bottom).

Further work is necessary to optimise the length of the grating, the shape of the silicone pad, the hardness of the silicone material and various other factors, however it has been demonstrated that this approach to tactile sensing shows promise. Also it may eventually be beneficial to use LPG sensors in this application, since they were found to be more sensitive to load and load angle than FBG sensors, providing the mechanical breakage problems can be overcome.

6.3.5 Dynamic response

The procedure followed in 6.3.3. above was slow, time consuming and a manual process in which a series of measurements were taken when the profile block was stationary at various positions on the sensor. In order to simulate a version of surface profile sensing which could be used for a faster sensing rate or even a continuous process (such as textile manufacture), some tests were done using the same sensors but while the profile block was moving.

A sensor was mounted on a translation stage driven by a motion controller (Newport MM4006). which ran at a constant speed of 2mm/s. (fig.130). The profile block was clamped over the translation stage so that the sensor made contact with the profile block but was still able to move beneath it.

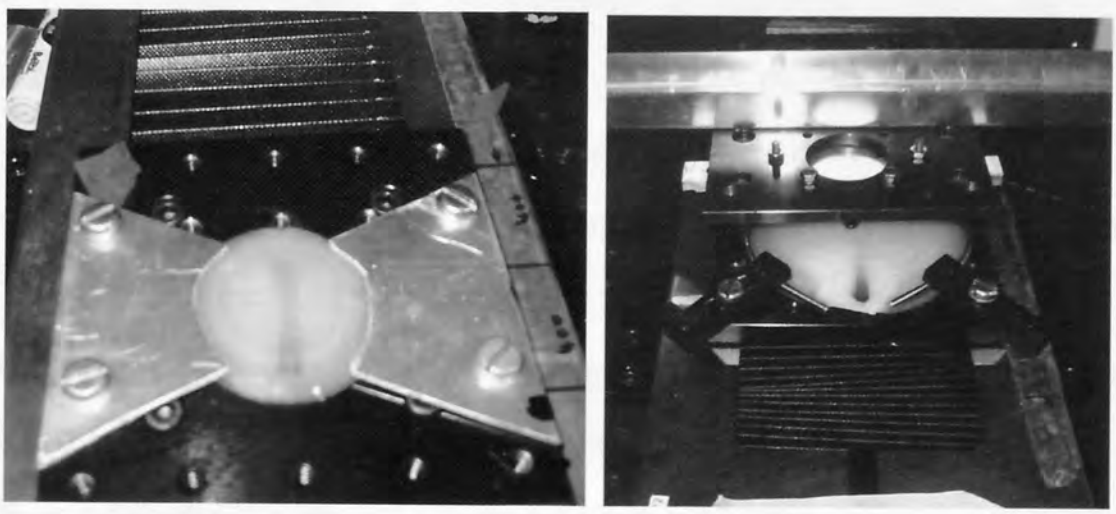

Fig. 130 Sensor mounted on translation stage (left), larger size sensor passing under profile (right)

The pressure between the profile block and the sensor was adjusted so that the spectral shift in the FBG reflected spectrum was 300pm. This value was chosen because it was the greatest value of pressure reliably achievable before the spectral response of the grating began to break up into several smaller, broader peaks representing the uneven distribution of pressure along the grating due to the pressure from the profile block.

The sensor was interrogated using a DFB tuneable laser which was modulated using a sinusoidal signal generator. The centre wavelength of the laser was arranged to coincide with the leading edge of the spectral peak reflected by the grating (fig.131).

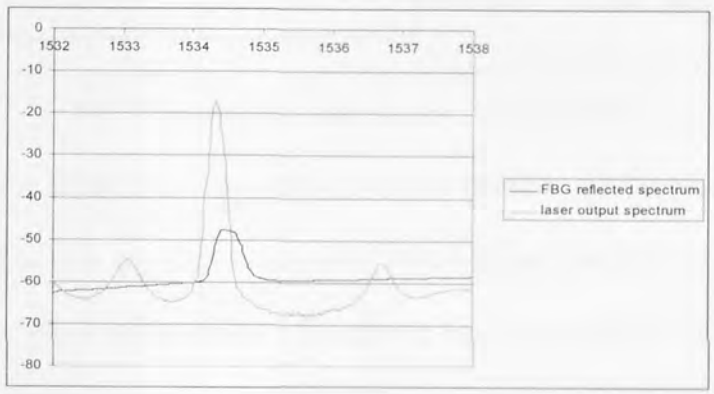

Fig. 131 Relative wavelengths of laser (larger peak) and FBG (smaller peak) spectra

The laser was modulated using a 1 kHz sinusoidal waveform. The modulated laser light reflected from the grating was detected by a photodiode, and the output of the photodiode was monitored by an oscilloscope which recorded the voltage/time waveform, v(t), (fig.132) and calculated the Fourier transform (FFT) of the photodiode signal (fig.133) as the sensor passed under the profile block. The purpose of this arrangement was to shift the frequency of the spectral variations caused by the surface profile from 1Hz (the stage ran at 2mm/sec, which was equal to one period of a profile block per second) to the 1-10kHz range. This avoids low frequency noise and allows the harmonic content of the signals to be analysed more easily. FFT and v(t) signals were recorded five times for each profile block and repeated for two FBG sensors, the 10mm and 2.5 mm sensor

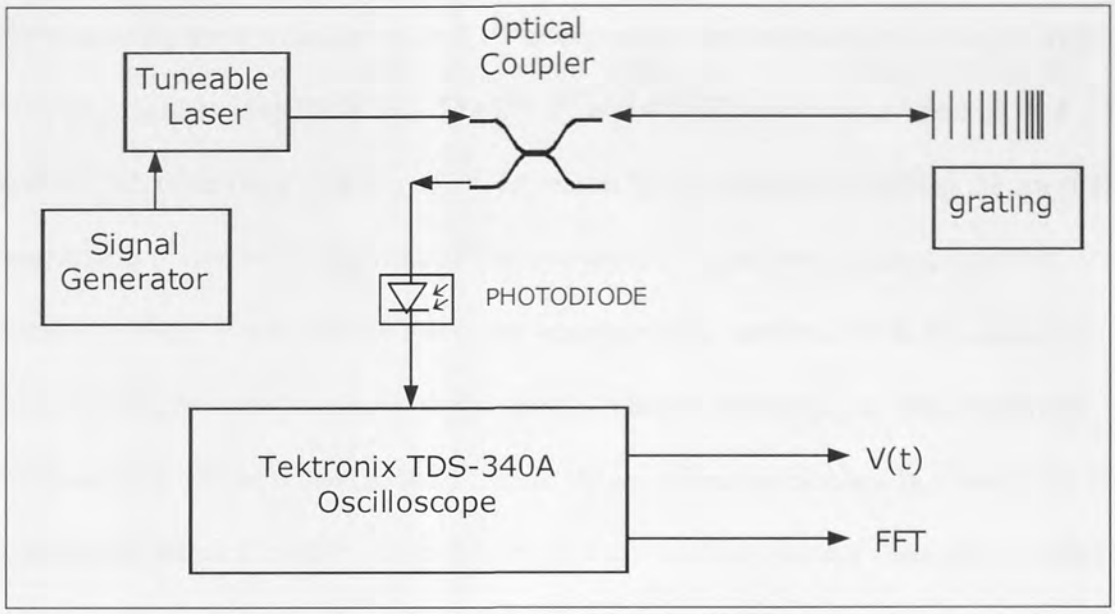

Fig. 132 Experimental arrangement for dynamic tests

Each time the profile block was changed the pressure between the block and the sensor was adjusted to be as near constant as possible. This was achieved by observing the reflected spectrum of the grating using a broadband light source (AFC Technologies BBS 1550 (1520-1565nm, 25-60mW) and an OSA (Hewlett Packard 86142A, resolution bandwidth 0.2nm), and adjusting the vertical position of the profile block so that the reflected spectrum under load was the same for each block.

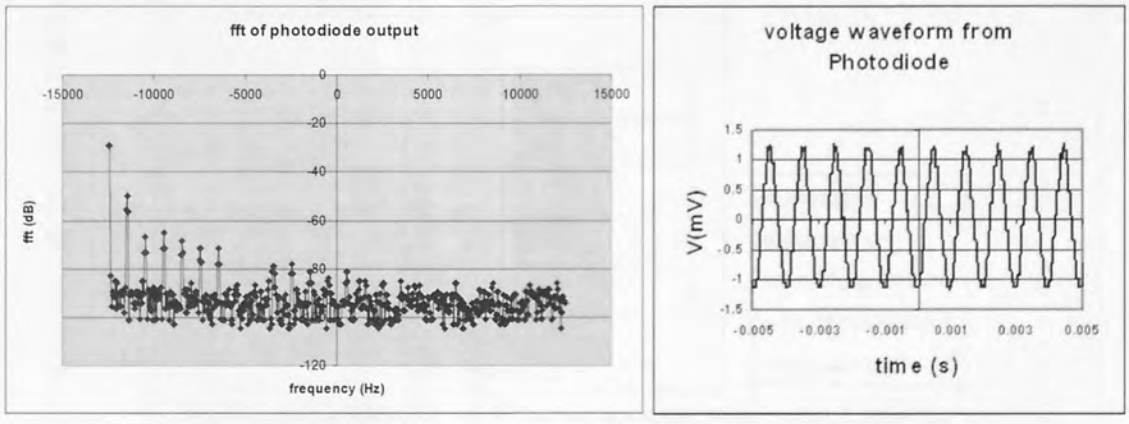

Fig. 133 Typical FFT trace (left) and typical v (t) trace (right)

The profiles used were square, triangle, semicircle, sawtooth (sharp), sawtooth (blunt) and in the case of the sensor with the 10mm grating a smooth profile block (flat).

6.3.5.1 Results

The results for the amplitudes of the FFT components were normalised so that the first component had an amplitude of 1, The 2nd, 3rd and 4th FFT components were plotted against each other (figs. 134 and 135) The reason for recording and plotting the spectral components in this way is because in the first series of experiments (using a manual translation stage) it was noticed that there were harmonic components in the measured spectral changes, and it was considered that the relative magnitudes of these harmonic components might be related to the different shapes of profile blocks. By plotting the FFT components for each profile on the same axes it can be seen whether there is a significant difference between the harmonic components produced.

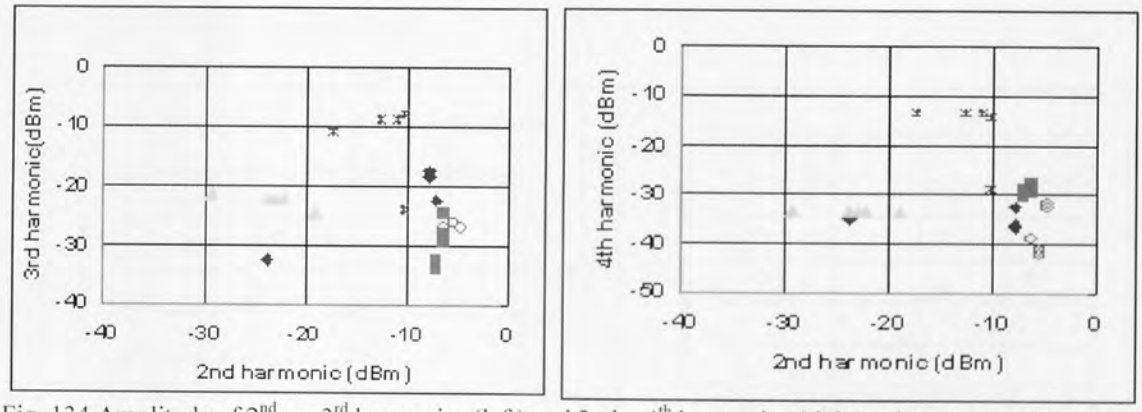

Fig. 134 Amplitude of 2nd vs. 3rd harmonics (left) and 2nd v 4th harmonics (right) using sensor with 2.5mm grating (see fig 135 for key).

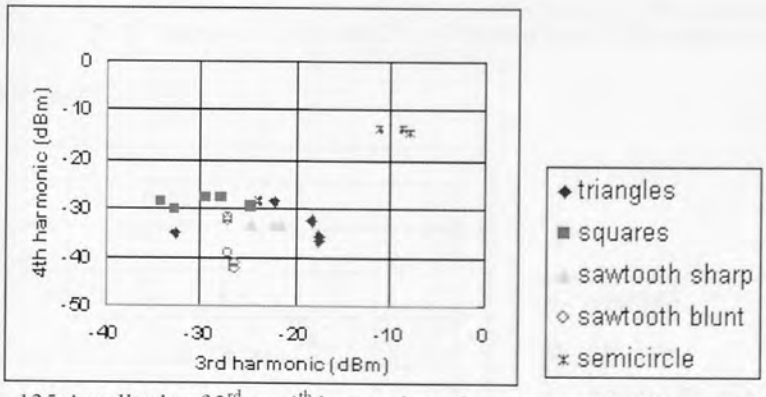

Fig.135 Amplitude of 3rd vs. 4th harmonics using sensor with 2.5mm grating

Figs. 134 and 135 show some separation between the various profile shapes in signal space. To enhance this effect, the 2nd, 3rd and 4th harmonics were plotted against each other

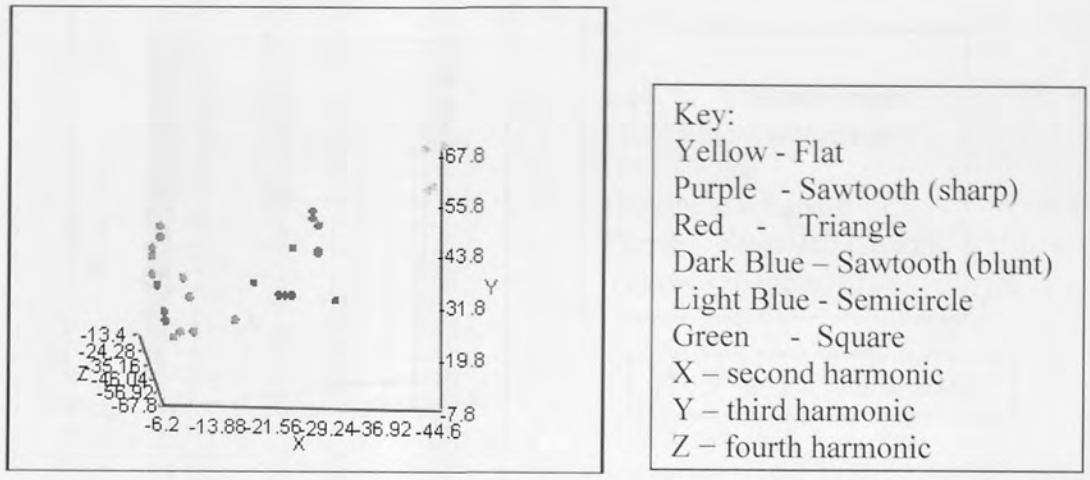

Fig.136 Amplitudes of 2nd, 3rd and 4th harmonics using sensor with 2.5mm grating

Fig. 136 shows that the results for the different surface profiles were separated from each other in signal space, therefore it should be possible to distinguish the profiles by examining their spectral content.

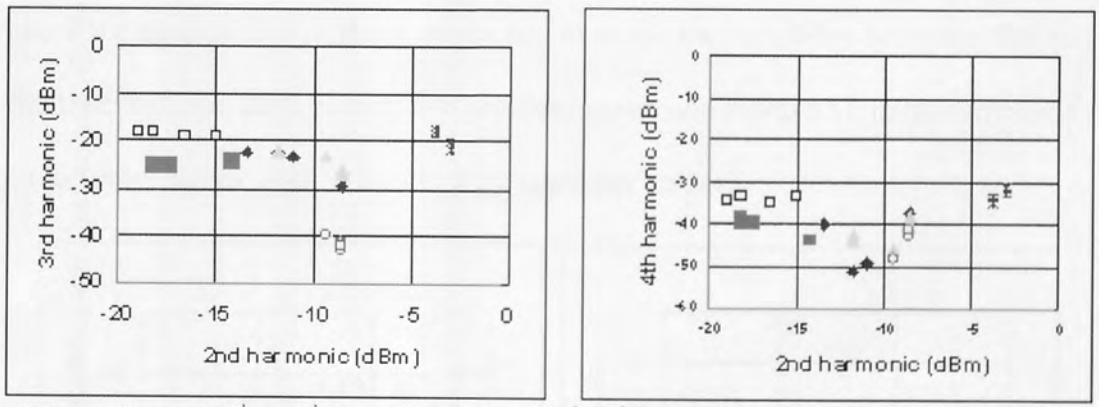

Fig. 137. Amplitude of 2nd vs. 3rd harmonics (left) and 2nd v 4th harmonics (right) using sensor with 10mm grating (see fig.138 for key).

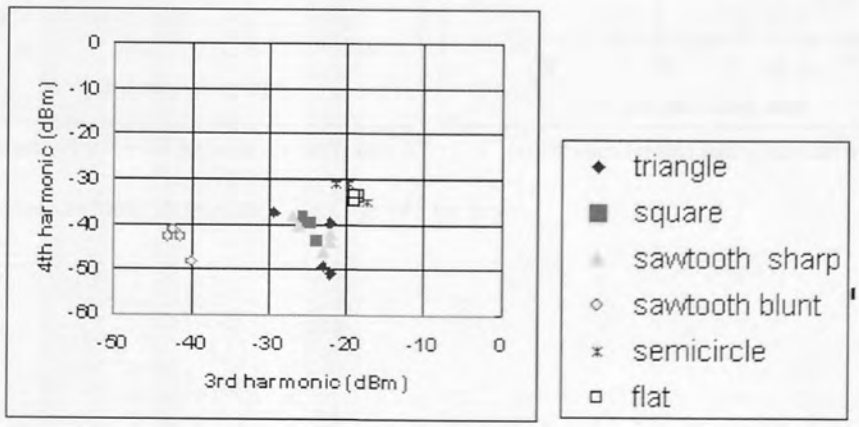

Fig.138 Amplitude of 3rd vs. 4th harmonics using sensor with 10mm grating

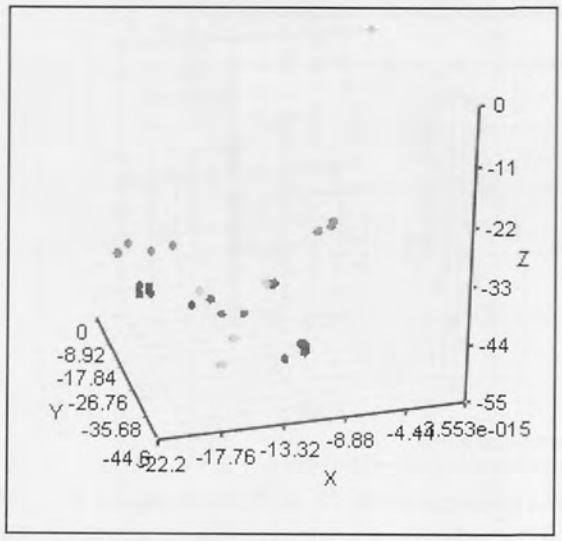

Key:
Red - Sawtooth blunt
Light blue – semicircle
Green – flat
Dark blue – Square
Purple – Sawtooth (sharp)
Yellow - triangle

2^{nd}, 3^{rd} and 4^{th} harmonics

Fig.139 Amplitudes of 2^{nd}, 3^{rd} and 4^{th} harmonics using sensor with 10mm grating

In figs 137-139 it can be seen that better separation is achieved between the different profile shapes when the 2^{nd}, 3^{rd} and 4^{th} harmonics are used than was achieved with any two harmonics. This is true for either of the two grating lengths.

To check the repeatability of these results and to assess the variability of results that might be obtained from the same sensor, two profiles, square and sawtooth (sharp) were used with the 10mm sensor, and 10 results were taken per sensor.

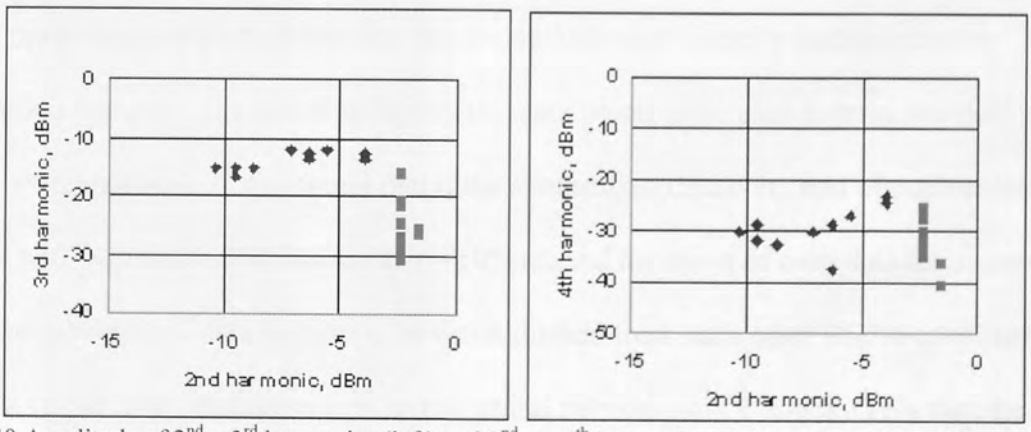

Fig. 140 Amplitude of 2^{nd} v 3^{rd} harmonics (left) and 2^{nd} vs. 4^{th} harmonics (right) using sensor with 10mm grating, square and sawtooth shapes only. (see fig. 141 for key).

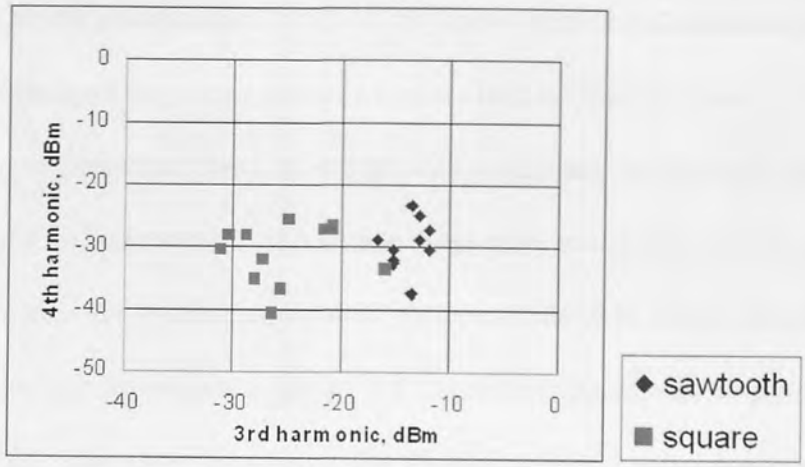

Fig.141 Amplitude of 3rd vs. 4th harmonics using sensor with 10mm grating, square and sawtooth shapes only

It can be seen from figs. 140 and 141 that the amplitudes of the harmonic components of the two shapes used continued to be well separated in signal space even when more samples were taken. The second harmonic for the square profile and the 3rd harmonic for the sawtooth show particularly consistent values.

6.3.5.2 Use of neural networks

In order to establish whether these data clusters can be reliably distinguished from one another, the data sets were expanded by adding random values of a gaussian distribution about the average of each of the data sets (using Microsoft Excel's random number generation feature) . The resulting 'synthetic' data points were used to train, validate and test a neural network. It was found that if the synthesized data consisted of randomised values with a gaussian distribution at +/- 10% around the mean of each data set on each axis, the synthesized data sets could be distinguished from each other 95.5% of the time using a single layer Multilayer perceptron neural network with 5 nodes. (This was the neural network architecture which produced the lowest training error, networks with between 1 and 20 nodes having been trained for this task). The experimental data values were correctly categorized 71% of the time. If neural networks were trained using data arranged within +/- 15% of the mean of the experimental data sets the correct identification

rate for the experimental data rose to 82%. This shows that neural networks could be a useful tool for categorizing the profile of a surface in this type of system.

It should be appreciated that these are preliminary results and substantially more work needs to be done on these systems to validate these early trials. Also a great deal of optimisation of the experimental equipment needs to be done to ensure that anomalies due to the mechanical arrangement are minimised. At present the amount of dismantling and reassembly which has to occur to change the profile shape is disadvantageous. Also to establish whether this kind of neural network could be used reliably to detect the different surface profiles a lot more data would be needed. The data sets for training, validation and testing should not be collected all in one batch, so that any variations in measurements due to mechanical arrangement or ambient temperature are adequately represented. As a way of eliminating the dismantling process a suggested experimental arrangement would be to mount 2 of the profiles end to end, making sure that they each exert the same pressure on the sensor when they contact it, and then observe the differences in the signals from the sensor before and after the transition between the two different surfaces.

6.3.5.3 Conclusions

It can be seen in all the graphs in section 6.3.6 that there is some grouping of data points by profile shape, but there are also some data to which this does not apply. It is possible that the patterns could be interpreted by a neural network, which might be trained to distinguish between some, if not all of the shapes. However it is also possible that some mechanical or physical property of the experimental rig is changing each time the profile block is changed over, and that this is responsible for the grouping of the data. It is also possible that some of the changes seen are due to the effect of changing temperature.

It should be stressed that these are preliminary results and that this work is continuing. The test and results presented here are merely for proof of principle and to suggest a method of

interrogating the sensors that might prove useful.

This form of dynamic real-time surface profile sensing has potential but a great deal of further work is required to fully assess this. As was observed in section 6.3.4.5 above, LPG sensors should also be assessed in this application (provided the breakage problems can be overcome and there is not a problem with the refractive index of the surrounding medium) since LPGs were found to be more sensitive to load parameters than FBGs. In this case either temperature compensation would probably be required (since LPGs are more sensitive to temperature changes than FBGs [73]) or alternatively LPGs in Photonic Crystal Fibre (which are not temperature sensitive [176]) could be used.

6.4 Summary

A sensor made by encapsulating an FBG in silicone and translating it across a ridged surface with 1mm ridges is capable of acting as a sensor to detect those ridges. The static tests showed that triangular and semicircular ridges could be detected reliably and sawtooth ridges could be detected in some circumstances. Square ridges were not detected. The static tests further showed that a longer grating gave a larger response to the ridges than the shorter grating, specifically the 25mm grating gave 40% more wavelength shift and 10 times more change in spectral width than the 2.5mm grating in response to the triangular profile block. The results of dynamic tests were less clear and further work is needed to clarify the results and optimise the experimental arrangement.

Chapter 7 - Conclusions

Tactile sensing is a complex and diverse field, both in the human sense of touch and in the area of artificial tactile sensing systems. Many different types of tactile sensors have been developed for different and often quite specific applications. This is a reflection of the complexity of tactile sensing, which involves not just the presence or absence of a contacting object but also its position, shape, surface texture, weight, size, hardness or softness, the degree of slippage and so on. The human tactile sensing system uses at least 4 types of sensors to detect these parameters and it is considered unlikely that a single type of artificial tactile sensor will ever be capable of sensing all of them. Over the last 20-30 years there has been much development in the field of artificial tactile sensing, however there remains scope and demand for better tactile sensors and there are still applications for which no suitable tactile sensors exist, particularly the area of minimally invasive surgery. Optical fibre sensors are particularly well placed to fulfill this demand since they are electrically passive, very small, light and require fewer connections than electrically powered sensors. They are also immune to electromagnetic interference. Optical fibre sensors do have some disadvantages, their cross sensitivity to temperature being one, however these difficulties are not insurmountable. Fibre Bragg grating sensors have become established in civil engineering applications as strain sensors for monitoring large

structures over long periods of time. They are capable of sensing very small changes in strain and are also sensitive to other measurands. In this work they have been used exclusively as strain sensors.

The use of fibre Bragg grating sensors with neural network processing in a distributive tactile sensing system is novel and has definite advantages for various sensing applications including in minimally invasive surgery. The fact that this type of system enables a small number of sensors to achieve a position resolution much smaller than the inter-sensor spacing means that it is not necessary to introduce a large array of sensors with multiple connecting wires into a device. FBGs have been shown to be at least as effective for use in a distributive tactile sensing system as resistive strain gauges.

It should be possible to use FBG sensors to instrument an endoscope to sense its shape and to detect some parameters of a contacting object. The number and location of such sensors would depend upon the flexibility of the endoscope and the information required. The optimum length of an FBG for use in an endoscope is small because tight bends in flexible endoscopes would otherwise produce distorted spectral peaks due to varying strain along the length of the grating. The issue of a suitable fixing method for the sensors and the type of substrate to which the sensors would be fixed would need to be addressed. Some method of temperature compensation would also be required. Discussion with an end-user would also be useful to ascertain what form of output information would be useful and how it would be best presented. A large amount of data would then need to be obtained experimentally to train a neural network before the degree of tactile sensitivity such an arrangement possessed could be assessed.

The next step in the development of an endoscope with tactile sensitivity using FBG sensors would be to investigate dynamic systems, and to collect data for different types of contacting objects. Tam [49] has begun this kind of work using strain gauges and a pneumatically powered experimental rig, but we consider that it is important to begin using a real endoscope for this work.

We have also demonstrated the use of FBGs in a two-dimensional distributive tactile sensing system for the sensing of load shape and position, where we compared the results with those obtained from a similar system using displacement sensors. The FBG system achieved more accurate results over a greater area of the surface than the comparable system. We have studied the factors which cause errors in such a system and devised ways of improving its accuracy and repeatability. We have also built and tested a larger 2D system capable of taking the weight of a person, suitable for possible use in podiatry, with which we were able to distinguish certain characteristics of a user's feet. This type of system could also have uses in pick and place systems where an object could be recognised and its position and orientation detected so that a robotic arm could then pick it up, security systems (human gait is particular to the individual and very difficult to imitate [180]) and livestock/equine sports applications.

A further development of this work would be to study dynamic systems for gait or balance analysis. A large amount of data would be needed and one parameter to be established is a suitable rate of data capture for a dynamic system investigating gait analysis. It has been found [178] that 30Hz is a suitable sampling rate for palpation, but this might not be sufficiently fast to capture the transient information for gait analysis.

We have seen how using neural networks in interrogation systems can lead to a cheaper form of system using fewer components. It should be noted that because neural networks are trained to recognise the patterns in the sensor data this is an application-specific system which would need to be retrained if it were to be transferred onto another arrangement with the same number of sensors monitoring different types of contacting objects. However this system is scalable without increasing bandwidth and has fewer photodetectors than sensors. It also has a much lower cost than other interrogation systems.

We have seen how a single FBG (or theoretically an LPG) might be used as a surface profile sensor in the 2mm range, and how a neural network might be used to interpret the signals from such a sensor using harmonic analysis. This work is at an early stage and offers much scope for further investigation. Various parameters have yet to be investigated and optimised – the size, shape and material of the encapsulation, the length of the grating and the speed of traverse of the sensor over the surface being monitored, however we believe that this device shows potential as a new type of tactile sensor.

Finally we have seen that fibre Bragg grating sensors combined with neural networks have much to offer to the field of tactile sensing in general and medical applications in particular, and that further research in this area should result in useful advances and new devices based on this technology.

The aims and objectives of this work were:

- To review the current developments in related technologies. This has been done in Chapter 2, focusing in particular on tactile sensing, optical fibre sensors and neural networks.

- To conduct experiments with Fibre Bragg Grating sensors in 1 and 2 dimensional distribute tactile sensing applications. This work was covered in Chapters 3 and 4 respectively, and it was found that FBG sensors produced detection accuracy rates at least as high as those achieved using more conventional sensor types in a comparable experimental arrangement.
- To examine and evaluate a lower cost method of interrogating FBG sensors for use in this type of application. This work has been described in Chapter 5, where a potential cost reduction by a factor of 56 has been identified, although the system described would need to be trained for each application for which it was used, unlike the more expensive version.
- To conduct experiments on a novel arrangement of optical fibre sensors encapsulated in silicone for tactile sensing applications. This work is seen in Chapter 6, where the results of static and dynamic tests are presented. The static results show sufficient promise for this device as a new type of tactile sensor for a patent application to be filed.

Appendix 1 Design of Footplate

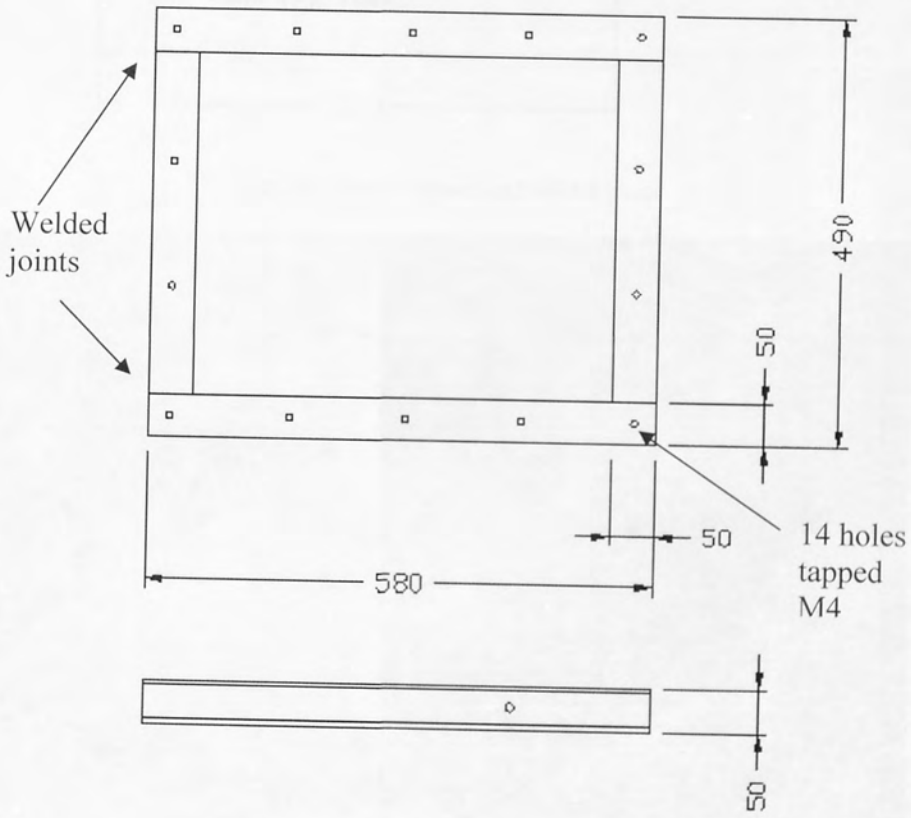

Fig. 142 Design of footplate (3rd angle projection)

Framework: I-section steel 4mm gauge (see fig x and y).
One 1.5mm thick stainless steel sheet 580x490mm with holes M4 clearance countersunk to match M4 tapped holes in framework
One 4mm thick PMMA sheet 580x490mm with holes M4 clearance to match M4 tapped holes in framework and FBG sensors mounted as shown in fig xx.

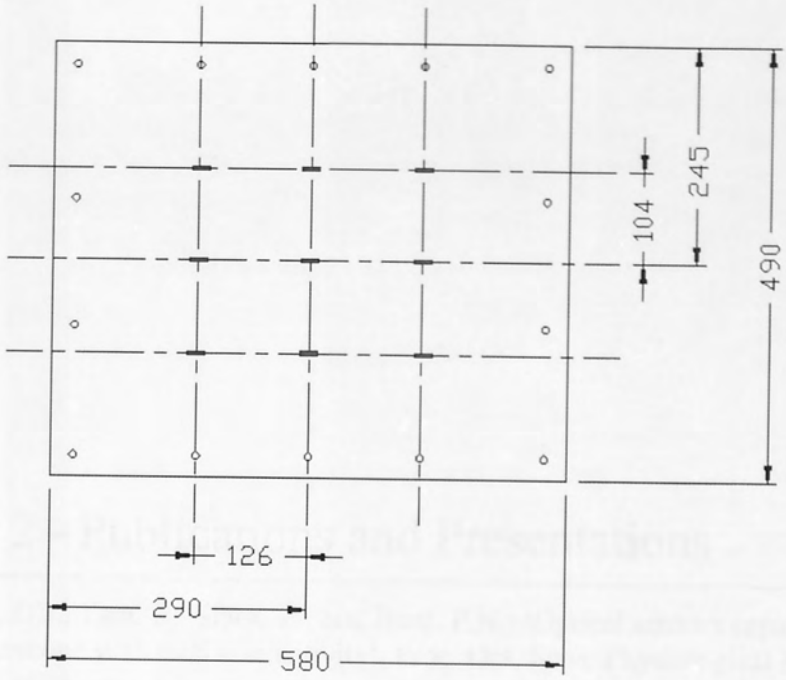

Fig. 143 Sensor layout on PMMA sheet

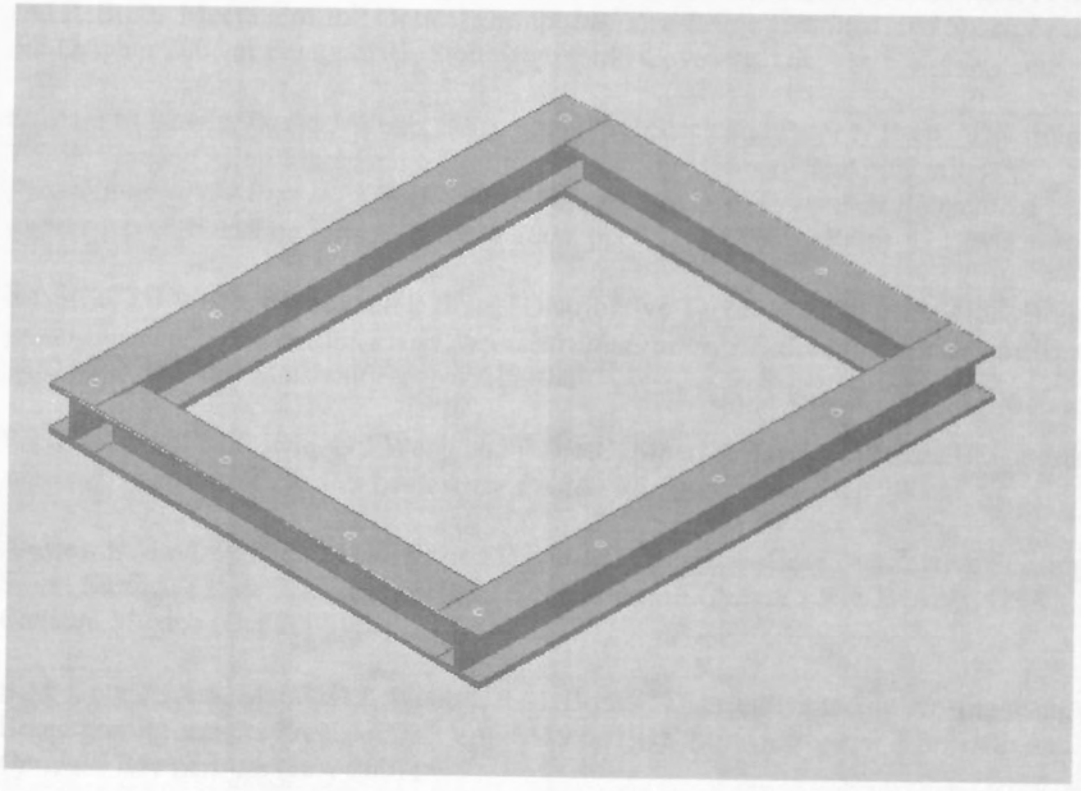

Fig. 144 Supporting framework

Appendix 2 - Publications and Presentations

Cowie, B.,Webb, D.J., Tam, B., Slack, P., and Brett, P.N.: 'Optical sensors capable of providing an endoscope with tactile sensitivity'. Proc. Opt. Sens. Physiological Meas., London, Institute of Physics, May 2005

Presentation: "Smart surfaces using FBG sensors" B. Cowie, D.J. Webb, B. Tam, P. Slack, and P. Brett, Meeting of IoP Optical Group *In-Fibre Bragg Gratings And Special Fibres* 5th October 2005 at Photonex05, Stoneleigh Park, Coventry, UK.

Barbara M Cowie, David J Webb, Betty Tam, Paul Slack and Peter N Brett, "Distributive Tactile Sensing using Fibre Bragg Grating Sensors for Biomedical Applications", *Proceedings of the first IEEE/RAS-EMBS International Conference on Biomedical Robotics and Biomechatronics,. BioRob 2006,* pp. 312- 317 (Feb 2006)

B Cowie, DJ Webb, B Tam and P Brett, "Distributive Tactile sensing using Fibre Bragg grating sensors", *Biophotonics And New Therapy Frontiers,Proceedings of* the SPIE, 6191, pp. 249 (Apr 2006) Strasbourg, paper 61910Z

Presentation: B M Cowie, D J Webb and P Brett, "Smart surface using fibre Bragg grating sensors", *Institute of Physics conference Photon 06*, Manchester (Sep 2006)

Andrew S Main, Barbara M Cowie and David J Webb, "Low Cost Distributive Sensing Smart Surface", *Proc 18th International Conference on Optical Fiber Sensors*, OSA, Cancun, Mexico (Oct 2006) paper FA5.

B.M. Cowie[a], A.S. Main[a], D.J. Webb[a*], P.M. Brett[b] "Distributive tactile sensing using fibre Bragg grating sensors Proceedings" Vol. 6619 *66193T Third European Workshop on Optical Fibre Sensors* (July 2007)

Barbara M Cowie, David J Webb, Betty Tam, Paul Slack and Peter N Brett "Fibre Bragg grating sensors for distributive tactile sensing" *Meas. Sci. Technol.* 18 (2007)

Barbara Cowie, Thomas Allsop, John Willliams, David Webb, Ian Bennion, and Matthew Fisher "An optical fiber Bragg grating tacttile sensor" *Proceedings of the SPIE* Vol. 6585, 65850I (2007)

References

1. M.H. Lee, and H.R. Nicholls, "Tactile sensing for mechatronics - a state of the art survey", *Mechatronics* 9, (1999) pp1-31.
2. V. Maheshwari, and R. Saraf, "High-Resolution Thin-Film Device to Sense Texture by Touch" *Science* 9 (2006) Vol. 312. no. 5779, pp1501 - 1504
3. K.O. Johnson, "The roles and functions of cutaneous mechanoreceptors", *Current Opinion in Neurobiology* 11 (2001) pp455–461.
4. G. Weddell, "The Anatomy Of Cutaneous Sensibility" *Br Med Bull* 3 (1945) pp167-172.
5. M. Tanaka, K. Miyata, T. Nishizawa and S. Chonan, "Development of a tactile sensor system for reading Braille: fundamental characteristics of the prototype sensor system" *Smart Mater. Struct.* 14 (2005) 483–487.
6. http://www.etymonline.com accessed 28/10/07
7. http://www.brandtinst.com/testo/Endoscope/index.html accessed 1/10/07
8. http://www.allen-vanguard.com/Catalogue/SE/615/20150.html accessed 11/2/08
9. http://www.udpg.co.uk/remedialwallties.htm
10. http://www.experts-xylophages.com/html/methodologie.html,
11. www.vet.uga.edu/mis/exotics/equipment/flexible.php
12. http://www.fishvetsociety.org.uk/meetings.php
13. http://www.horsevet.co.uk/endoscopy.php
14. http://www.aie.org.uk/tools/aie_tool_endoscope.html15. R.V. Stambaugh, "A Clinician's 3-Year Experience With Perioscopy", *Compend Contin Educ Dent.* (2002) v23(11A) pp1061-70
16. http://www.istcorp.com/img_nuc_surv_thru_wall_endoscope.html
17. http://ap.pennnet.com/display_article/197754/36/ARTCL/none/none/1/Endoscopic-Inspection-of-Area-Array-Packages. Accessed 12/2/08
18. http://www.1800endoscope.com/endoscopymuseum.htm accessed 9/9/07

33. G. Murali Krishna and K. Rajanna "Tactile Sensor Based on Piezoelectric Resonance" *IEEE Sensors Journal* (2004), Vol. 4, No. 5, pp691-697

34. E.G.M. Holweg, W. Jongkind, "Object recognition using a tactile matrix sensor", *Proceedings of European Robotics and Intelligent Systems Conference*, (1994) vol. 3, pp1379-83.

35. R.E. Ellis, S.R. Ganeshan, S.J. Lederman, "A tactile sensor based on thin-plate deformation" *Robotica* (1994) v 12, pt.4, pp343-51.

36. R.S.W. Stone, P.N.Brett, "Flexible pneumatic actuator for gripping soft irregular shaped objects", *IEE Colloquium (Digest)*, (1995) n 170, p 13/1-13/3.

37. R.S.W. Stone, P.N Brett, "Sensing technique for the measurement of tactile forces in the gripping of dough-like materials". *Proceedings of the Institution of Mechanical Engineers, Part B: Journal of Engineering Manufacture*, (1996) v 210, n B3, , pp261-269.

38. R.S.W. Stone, P.N. Brett, B.S. Evans, "Automated handling system for soft compact shaped non-rigid products" *Proceedings of the IEEE International Conference on Systems, Man and Cybernetics*, (1996) v 4, pp3000-3005.

39. R. S. Stone, P. N. Brett, B. S. Evans, "An automated handling system for soft compact shaped non-rigid products" *Mechatronics* 8 (1998) pp85-102.

40. R.W.S. Stone, P.Tongpadungrod, and P.N. Brett, "A deforming sensing surface for evaluation of contact conditions", *Proceedings of the 20th Annual International Conference of the IEEE Engineering in Medicine and Biology Society* (1998) vol 4, pp1735-1737.

41. P. Tongpadungrod, "A technique to increase performance of a distributive tactile sensing system through an application of the Principal Component Analysis (PCA)", *Proceedings of the IEEE International Conference on Systems, Man and Cybernetics* (2003) Vol 5, pp4210-15.

42. R.S.W. Stone, P.N Brett, "Techniques for Interpretation of data for tactile sensing", *Proceedings of 2nd International Conference on Mechatronics and Machine Vision in Practice*, (1995), pp233-238).

43. P.N. Brett, R.S.W Stone, "Technique for measuring contact force distribution in minimally invasive surgical procedures", *Proceedings of the Institution of Mechanical Engineers, Part H: Journal of Engineering in Medicine* (1997), Vol 211, n 4, pp309-316.

44. PhD Thesis 'A distributive tactile sensing technique for soft deformable contact' RSW Stone, 1997, University of Bristol

45. P.N. Brett, Z. Li, "Tactile sensing surface for artificial neural network based automatic recognition of the contact force position". *Proceedings of the Institution of Mechanical Engineers. Part I: Journal of Systems and Control Engineering* (2000), Vol. 214, n 3, pp207-215.

46. P. Tongpadungrod , T.D.L. Rhys, P.N. Brett "An approach to optimise the critical sensor locations in one-dimensional novel distributive tactile surface to maximise performance" *Sensors and Actuators A* (2003) Vol. 105 pp47–54

47 PhD Thesis, "Characteristics. of distributive tactile sensing system", P. Tongpadungrod,. University of Bristol, 2002

48. B. Tam, P.N. Brett, D.J. Holding and M. Griffiths "An Experimental investigation of the distributive tactile sensing method applied to discriminate contact and motion of a flexible digit typical of invasive clinical environments", *Proc. ASME Int. Design & Engrg Technical Conf & Information Engineering Conf.* (2005) Vol. 4, pp245-248

49. PhD Thesis "A Novel Actuated Digit With Tactile Feedback For Clinical Applications" by Betty Kit Yee Tam, Aston University, 2006.

50. M.J. O'Dwyer, C. Ye, S.W. James, R.P. Tatam, "Thermal dependence of the strain response of optical fibre Bragg gratings" *Measurement Science and Technology* (2004), vol. 15, no. 8 pp. 1607–1613.

51. Y. Zhao, Y. Liao, S. Lai, "Simultaneous Measurement of Down-Hole High Pressure and Temperature With a Bulk-Modulus and FBG Sensor", *IEEE Photonics Technology Letters* (2002).vol. 14, no. 11, pp1584-6

52. L. Jin, W. Zhang, H. Zhang, B. Liu, J. Zhao, Q. Tu, G. Kai, and X. Dong, "An Embedded FBG Sensor for Simultaneous Measurement of Stress and Temperature", *IEEE Photonics Technology Letters* (2006) vol. 18, no. 1, pp 154-6.

53. S. C. Tjin, R. Suresh, N. Q. Ngo, "Fiber Bragg Grating Based Shear-Force Sensor: Modeling and Testing" *Journal Of Lightwave Technology* (2004), vol. 22, no. 7, pp1728-33.

54. E. Pinet, A. Pham, S. Rioux, "Miniature Fiber Optic Pressure Sensor for Medical Applications: an Opportunity for Intra-Aortic Balloon Pumping (IABP) therapy", *Proceedings of SPIE - The International Society for Optical Engineering, OFS-17 (17th International Conference on Optical Fibre Sensors)*(2005), vol 5855 part 1, pp. 234-237.

55. S. Khotiantsev, D. Paredes, D. Molina-Flores, V. Esteban, A. Zemliak, V. Svirid, A. Matiuch, V. Kosinsky, "Fiber optic multipoint high-resolution level sensor for biomedical

applications", *Proceedings of SPIE - The International Society for Optical Engineering* (1995), vol. 2631, pp. 121-126.

56. R.N. Pattison, S. Janani, B. Mendenhall, C. Hwang, B.T. Frohlich, "Measurement and control of dissolved carbon dioxide in mammalian cell culture processes using an in situ fiber optic" *Biotechnology Progress* (2000) v 16, n 5, pp769-774
57. D. L. Williams and R. P. Smith, "Accelerated Lifetime Tests On UV Written Intra-core Gratings in Boron Germania Co doped Silica Fibre," *Electronics Letters* (1995), vol. 31, Iss. 24, pp. 2120-2121.
58. Peter L Fuhr, Stephanus J Spammer and Yinian Zhu "A novel signal demodulation technique for chirped Bragg grating strain sensors" *Smart Mater. Struct.* 9 (2000) pp85–94
59. K. O. Hill, Y. Fujii, D. C. Johnson, and B. S. Kawasaki, "Photosensitivity in optical fibre waveguides: application to reflection filter fabrication," *Applied Physics Letters* (1978), vol. 32, pp. 647-649.
60. H.Z. Phing, J. Ali, R.A. Rahman and B.A. Tahir, "Fiber Bragg grating modeling, simulation and characteristics with different grating lengths". *Journal of Fundamental Sciences* 3 (2007) pp167-175.
61. Y.Rao, "In-fibre Bragg grating sensors", *Measurement Science and Technology* (1997), vol. 8, pp355–375.
62. K.O. Hill, B.Malo, F. Bilodeau, D.C.Johnson, "Photosensitivity in Optical Fibres", *Annual. Review of. Material. Sci.* (1993). Vol.23: pp125-57.
63. J. Zhang, K. Sugioka, S. Wada, H. Tashiro, K. Toyoda, and S. Ruschin. "Origin of High-Speed Modification of Refractive Index in Fused Quartz by Vacuum Ultraviolet Laser Irradiation" *IEEE Journal Of Selected Topics In Quantum Electronics* (1997), Vol. 3, No. 3, pp789-95.
64. http://www.avogadro.co.uk/structure/chemstruc/network/g-molecular.htm accessed 18/1/08
65. K. Kajihara , L. Skuja, M. Hirano, H. Hosono, "Interconversion between non-bridging oxygen hole center and peroxy radical in F2-laser-irradiated SiO2 glass", *Journal of Non-Crystalline Solids* (2004) vol. 345-346 pp219–223
66. PhD Thesis "Optical Fibre Sensors and their Interrogation" A.G. Simpson, Aston University, 2005.
67. M. Douay, W. X. Xie, T. Taunay, P. Bernage, P. Niay, P. Cordier, B. Poumellec, L. Dong, J. F. Bayon, H. Poignant, and E. Delevaque "Densification Involved in the UV-

Based Photosensitivity of Silica Glasses and Optical Fibers" *Journal Of Lightwave Technology* (1997), Vol. 15, No. 8, p1329.

68. L. Wosinski,, M. Dainese and M. Swillo, "UV-Photosensitivity and Refractive Index Engineering in Silica-Based Planar Lightwave Circuits" *Proceedings of 7th International Conference on Transparent Optical Networks*, (2005), Vol. 1, pp343 – 348.
69. E. N. Glezer, M. Milosavljevic, L. Huang, R. J. Finlay, T.-H. Her, J. P. Callan, and E. Mazur "3-D Optical Storage Inside Transparent Materials" *Optics Letters* (1996), Vol. 21, No. 24, p2023.
70. T. Erdogan, "Fiber Grating Spectra", *Journal Of Lightwave Technology* (1997), Vol. 15, No. 8, p1277.
71. S. Shaari and M. C. Shong "Characteristics of large bandwidth fiber Bragg grating with short grating length". *Proceedings of IEEE International Conference on Semiconductor Electronics* (2000), Vol 1, pp203-206.
72. M. Bass, E. W. van Stryland, J. M. Enoch, W. L. Wolfe, "Handbook of Optics" Optical Society of America, 9.5 vol 4 Publisher McGraw Hill Professional. http://books.google.co.uk/books?hl=en&id=vWAWVJ3vjPcC&dq=handbook+of+optics&printsec=frontcover&source=web&ots=Sw147gkU1s&sig=5obGLFONl8G6PP1PIBHImhwxowM&sa=X&oi=book_result&resnum=4&ct=result#PPT230,M1
73. S.W. James and R. P. Tatam "Optical fibre long-period grating sensors:characteristics and application" *Meas. Sci. Technol.* (2003) Vol. 14 ppR49–R61.
74. http://www.insensys.co.uk/index.asp?pgid=83 accessed 29.10.07
75. LabVIEW data acquisition software is produced by National Instruments Corporation http://www.ni.com/labview (accessed 10.1.08)
76. A.G. Simpson, K. Zhou, P. Foote, L. Zhang, I. Bennion "A Polarisation independent, high resolution spectral interrogation of FBGs using a BFBG-CCD array for optical sensing applications" *Proceedings of the SPIE* (2004), Vol. 5272, pp324-331.
77. D.C.C. Norman, D.J. Webb, R.D. Pechstedt, "Interferometric and fibre Bragg grating sensor interrogation using an arrayed waveguide grating" *Proceedings of the SPIE*, Volume 5459, pp. 101-108.
78. A. Cusano, A. Cutolo , J. Nasser , M. Giordano , A. Calabrò "" *Sensors and Actuators A* 110 (2004) pp276–281

79. R W Fallon, L Zhang, L A Everall, J A R Williams and I Bennion "All-fibre optical sensing system Bragg grating sensor interrogated by a long-period grating" *Meas. Sci. Technol.* 9 (1998) pp1969–1973.

80. R Romero, O Frazao, P V S Marques, H M Salgado and J L Santos "Fibre Bragg grating interrogation technique based on a chirped grating written in an erbium-doped fibre" *Meas. Sci. Technol.* 14 (2003) 1993–1997.

81. http://www.insensys.co.uk/windenergy2007.asp accessed 12/10/2007

82. http://www.smartfibres.com/index.htm accessed 12/10/2007

83 http://www.fos-ta.com/FBG-interrogators.html accessed 12/10/2007

84.http://www.micronoptics.com.cn/en/index.html accessed 12/10/2007

85.http://64.78.38.246/fos-s/website/index.html accessed 12/10/2007

86. http://www.micronoptics.com/si720.htm

87. A. Ezbiri, S.E. Kanellopoulos, V.A. Handerek "High resolution instrumentation system for fibre-Bragg grating aerospace sensors" *Optics Communications* (1998) Vol.150 pp43–87.

88. S. D. Dyer, P. A. Williams, R. J. Espejo, J. D. Kofler and S. M. Etzel "Fundamental limits in fiber Bragg grating peak wavelength measurements" *Proc. of SPIE - The Int. Society for Optical Engineering*(2005), *v 5855 PART I, OFS-17* pp88-93.

89. J.M. Gong, C.C. Chab, W. Jin, J.M.K. MacAlpine, M. Zhang, Y.B. Liao "Enhancement of wavelength detection accuracy in fiber Bragg grating sensors by using a spectrum correlation technique" *Optics Communications* (2002) 212 pp29–33.

90. C.C. Chan, W. Jin, M.S. Demokan. "Enhancement of measurement accuracy in fiber Bragg grating sensors by using digital signal processing" *Optics & Laser Technology* 31 (1999) pp299-307.

91. P.L. Fuhr, D.R. Huston, P.J. Kajenski and T.P. Ambrose. "Performance and health monitoring of the Stafford Medical Building using embedded sensors" *Smart Mater. Struct.* 1 (1992) p6348.

92. A. Mendez, T.F. Morse, L.J. Reinhart "Experimental results on embedded optical fiber sensors in concrete" *Proceedings of SPIE - The International Society for Optical Engineering*, (1993) vol 1918, pp420-427.

93. R. Brönnimann, P.M. Nellen and U. Sennhauser "Application and reliability of a fiber optical surveillance system for a stay cable bridge" *Smart Mater. Struct.* 7 (1998) pp229–236.

94. P.M. Nellen, A. Frank, R.Brönnimann, U. Sennhauser "Optical fiber Bragg gratings for tunnel surveillance", *Proceedings of the SPIE - The International Society for Optical Engineering*, v 3986, (2000) pp263-70.

95. G. Wang, K. Pran, G. Sagvolden, G. B. Havsgård, A. E. Jensen, G. A. Johnson and S. T. Vohra "Ship hull structure monitoring using fibre optic sensors" *Smart Mater. Struct.* 10 (2001) 472–478.

96. M. Bugaud, P. Ferdinand, S. Rougeault, V. Dewynter-Marty, P. Parneix and D.Lucas, "Health monitoring of composite plastic waterworks lock gates using in-fibre Bragg grating sensors" *Smart Mater. Struct.* 9 (2000) pp322–327.

97. K. Wood, T. Brown, R. Rogowski and B. Jensen "Fiber optic sensors for health monitoring of morphing airframes I. Bragg grating strain and temperature sensor" *Smart Mater. Struct.* 9 (2000) 163–169.

98. E J Friebele, C G Askins, A B Bosse, A D Kersey, H J Patrick, W R Pogue, M A Putnam, W R Simon, F A Tasker, W S Vincent and S T Vohra Optical fiber sensors for spacecraft applications Smart Mater. Struct. 8 (1999) 813–838.

99. W.L. Schulz, J. P. Conte, E. Udd, J.M.Seim "Static and dynamic testing of bridges and highways using long gage fiber Bragg grating based sensors" *Proceedings of SPIE* (2000) Vol4202 p79 from http://www.bluerr.com/papers/BRR-2000_SPIE_Vol4202_p79.pdf

100. J. Koh1, H. Bang, C. Kim and C. Hong. "Simultaneous measurement of strain and damage signal of composite structures using a fiber Bragg grating sensor" *Smart Mater. Struct.* 14 (2005) pp658–663.

101. V.Dewynter-Marty, P.Ferdinand, E.Bocherens, R.Carbone, H. Beranger, S.Bourasseau, M.Dupont, D.Balageas, "Embedded fiber Bragg grating sensors for industrial composite cure monitoring" *Journal of Intelligent Material Systems and Structures* (1999), v 9, n 10, pp785-787.

102. J.Zhang; L.Qian; L.Shen, Z.Yanan, "FBG sensor devices for spatial shape detection of intelligent colonoscope", *Proceedings of the IEEE International Conference on Robotics and Automation* (2004), n 1, pp 835-840.

103. Kevin Swingler, "Applying neural networks, A Practical guide", Academic Press, 1966 ISBN 0-12-679170-8

104. C M Bishop "Neural Networks for Pattern recognition", Clarendon Press, Oxford, 1995 ISBN 0-19-853864-2

105. H. Herrmann "On functional analysis with neural networks" *Smart Mater Struct.* 7 (1998) pp52–62.

106. http://www.statsoftinc.com/textbook/stneunet.html accessed 29.10.07

107. A.Leung, S.Payandeh, "Application of adaptive neural network to localization of objects using pressure array transducer". *Proceedings of IEEE International Conference on Systems, Man, and Cybernetics. Humans, Information and Technology* (1994), p 2114-19 vol. 3.

108. G.Canepa, R.Petrigliano, M.Campanella, and D.De Rossi "Detection of Incipient Object Slippage by Skin-Like Sensing and Neural Network Processing" *IEEE Transactions On Systems, Man, And Cybernetics—Part B: Cybernetics*, (1998) Vol. 28, No. 3 pp348-356

109. Y.C.Pati, D.Friedman, P.S.Krishnaprasad, C.T.Y.C.Pati, D.Friedman, P.S. Krishnaprasad, C.Tao, M.C. Peckerar, R. Yang, C.R.K Marrian "Neural Networks for Tactile perception", *Proceedings of the 1988 IEEE International Conference on Robotics and Automation* ,(1988), vol.1 pp134-9.

110. J. Worth, and R.R. Spencer "A Neural Network for Tactile Sensing: The Hertzian Contact Problem", *IEEE Transactions on Systems, Man and Cybernetics*, (1992) Vol. 22, Issue 1, pp177 – 182.

111. S.E Watkins, G.W Sanders, F. Akhavan and K Chandrashekhara "Modal analysis using fiber optic sensors and neural networks for prediction of composite beam delamination" *Smart Mater. Struct.* 11 (2002) pp489–495

112. J L Zapico, K Worden and F J Molina "Vibration-based damage assessment in steel frames using neural networks" *Smart Mater. Struct.* **10** (2001) pp553-559,

113. W J Staszewski, K Worden, R Wardle and G R Tomlinson "Fail-safe sensor distributions for impact detection in composite materials" *Smart Mater. Struct.* 9 (2000) pp298–303.

114. K.Worden, W.J Staszewski, "Impact location and quantification on a composite panel using neural networks and a genetic algorithm". *Strain*, v 36, (2000) n 2, pp 61-70.

115. A Caiti, G Canepa, D. De Rossi, F Germagnoli, G Magenes, T Parisini "Towards the realization of an artificial Tactile system: fine form discrimination by a Tensorial Tactile sensor array and neural inversion algorithms", *IEEE Transactions on Systems, Man and Cybernetics*, (1995) Vol 25 no 6. pp 933-46.

116. C.I.Tseng, W.J.Liou and H.J.Lee , "Development of an artificial skin ridge for pattern recognition" *Journal of Intelligent Material Systems and Structures*, (1997) Vol 8 pp4-11.

117. A. Lazaro and I Serrano, "Ultrasonic recognition technique for quality control in foundry pieces" *Meas.Sci Technol* 10 (1999) N113-N118.

118. R Bruno, N Toomarian and M Salama "Shape estimation from incomplete measurements: a neural-net approach" *Smart Mater. Struct.* (1994) vol 3 pp92-97.

119. G Song, V Chaudhry and C Batur "Precision tracking control of shape memory alloy actuators using neural networks and a sliding-mode based robust controller" *Smart Materials and Structures*, (2003) vol 12, n 2, pp 223-31.

120. J N Kudvat, N Munirt and P W Tan "Damage detection in smart structures using neural networks and finite-element analyses" *Smart Mater. Struct.* 1 (1992) pp108-112.

121. L H Yam, Y J Yan, L Cheng and J S Jiang "Identification of complex crack damage for honeycomb sandwich plate using wavelet analysis and neural networks" *Smart Mater. Struct.* 12 (2003) pp661–671

122. R. Jha and C. He "A comparative study of neural and conventional adaptive predictive controllers for vibration suppression" *Smart Mater. Struct.* 13 (2004) pp811–818.

123. C. Li and A. Rayt "Neural network representation of fatigue damage dynamics" *Smart Mater. Struct.* 4 (1995) pp126-133.

124. R K.R.Reddy and R.Ganguli "Structural damage detection in a helicopter rotor blade using radial basis function neural networks" *Smart Materials and Structures* (2003), v 12, n 2, pp 232-41

125. Z. Xu1, Y. Shen and Y. Guo "Semi-active control of structures incorporated with magnetorheological dampers using neural networks" *Smart Mater. Struct.* 12 (2003) pp80–87.

126. D. King, W B Lyons, C. Flanagan, E. Lewis "An Optical Fiber Sensor for use in Water Systems Utilizing Digital Signal Processing Techniques and Artificial Neural Network Pattern Recognition", *IEEE Sensors Journal* (2004) Vol 4 No 1. pp21-7

127. I. M. Raimundo Jr.1, R. Narayanaswamy "Simultaneous determination of relative humidity and ammonia in air employing an optical fibre sensor and artificial neural network" *Sensors and Actuators B* 74 (2001) pp60-68

128. B.K. Wong, Y. Selvi "Neural network applications in Finance: A review and analysis of literature (1990-1996)" *Information & Management* 34 (1998) pp129-139

129. J. Fathi, A. Hansa "Signature recognition using conjugate gradient neural networks" *Proceedings of 9th Joint Conference on Information Sciences* (2006) p 271

130. M.Schlag, E.Broese, B.Feldkeller, O.Granckow, M.Jansen, T.Pappe, C.Schaffner, G.Sorgel, "Neural networks for process control in steel manufacturing" *Proceedings of IEEE Int. Conf. on Acoustics, Speech, and Signal Processing*, (1997) Vol 1, pp155 – 158.

131. G. Yan, G. Ma "Fault Diagnosis Of Diesel Engine Combustion System Based On Neural Networks". *Proceedings of 2004 Int. Conf. on Machine Learning and Cybernetics*, (2004) vol.5 pp3111- 3114.

132. X. Hu, J. Wan, J. R. Slepski, D.C. Wunsch "Vibration Analysis Via Neural Network Inverse Models To Determine Aircraft Engine Unbalance Condition" *Proceedings of the International Joint Conference on Neural Networks*, (2003). Vol. 4 pp3001 – 3006.

133. D.S. Boone, M. Roehm "Retail segmentation using artificial neural networks" *Intern. J. of Research in Marketing* 19 (2002) pp287–301.

134. H. Y. Guo, L. Zhang, L. L. Zhang and J. X. Zhou "Optimal placement of sensors for structural health monitoring using improved genetic algorithms", *Smart Materials and Structures*, 13 (2004) pp528-534.

135. F. Gao, Y. Shen, L. Li "The optimal design of piezoelectric actuators for plate vibroacoustic control using genetic algorithms with immune diversity", *Smart Mater Struct* 9 (2000) pp485-491.

136. U O Akpan, T S Koko, I R Orisamolu and B K Gallant "Fuzzy finite-element analysis of smart structures" *Smart Mater. Struct.* 10 (2001) pp273–284.

137. P Mayhan and G Washington. "Fuzzy model reference learning control: a new control paradigm for smart structures" *Smart Mater. Struct.* 7 (1998) pp874–884.

138. I.J Zeinoun and F. Khorrami "An adaptive control scheme based on fuzzy- logic and its application. I to smart structures" *Smart Mater. Struct.* 3 (1994) pp266-276.

139. D. Wettschereck, D. W. Aha and T. Mohri "A Review and Empirical Evaluation of Feature Weighting Methods for a Class of Lazy Learning Algorithms" *Artificial Intelligence Review* (1997) Vol.11: pp273–314.

140. L.A.Quiroga and L C Rabelo, "Learning from Examples: a review of machine learning, neural networks and Fuzzy logic paradigms", *Proceedings of 17th Int conference on Computers and Industrial Engineering*, (1995) Vol 29 no 1-4. pp561-565.

141. K. H. Fuchs, "Minimally Invasive Surgery", *Endoscopy* (2002) Vol.34 pp154-159.

142. J. Peirs, D. Reynaerts, and H. Van Brussel, "Design of miniature parallel manipulators for integration in a self-propelling endoscope", *Sensors and Actuators A: Physical* (2000), Vol. 85, Issues 1-3, pp409-417.

142. http://www.mondoplast.ro/standarde/SM_G652B.pdf accessed 26/11/07

143. "Metric Practice for Structural steelwork", 3rd Ed, The British Constructional Steelwork Association Ltd, London.

144. D.H. Bacon & R.C. Stephens "Mechanical Technology", 3rd Ed, Butterworth Heinemann Oxford 1998 p 23.

145. S.Timoshenko and S. Woinowsky-Krieger "Theory of Plates and Shells" 1959 McGraw-Hill New York, 2nd Ed p142.

146. Chunn-Yenn Lin, Lon A. Wang and Gia-Wei Chern "Corrugated Long-Period Fiber Gratings as Strain, Torsion, and Bending Sensors" *Journal Of Lightwave Technology* (2001) Vol. 19, No. 8, pp1159-1168.

147. Yun-Jiang Rao, Yi-Ping Wang, Zeng-Ling Ran, and Tao Zhu, "Novel Fiber-Optic Sensors Based on Long-Period Fiber Gratings Written by High-Frequency CO2 Laser Pulses" *Journal Of Lightwave Technology*, Vol. 21, No. 5, May 2003 pp1320-27.

148. T. Allsop, A. Gillooly, V. Mezentsev, T. Earthgrowl-Gould, R. Neal, D.J.Webb, I. Bennion, "Bending and orientational characteristics of long period gratings written in D-shaped optical fiber" *IEEE Transactions on Instrumentation and Measurement*, Volume 53, Issue 1, Feb. 2004 pp130 – 135.

149. H.J. Patrick "Self-aligning, bipolar bend transducer based on long period grating written in eccentric core fibre" *Electronics Letters* 12th October 2000 Vol. 36 No. 219.

150. Young-Geun Han et al "Fibre-optic sensing applications of a pair of long-period fibre gratings" 2001 *Meas. Sci. Technol.* 12 pp778-781.

151. http://www.crystran.co.uk/products.asp?productid=73 accessed 30/1/08

152. Xiao Chun Li, Fritz Prinz and John Seim "Thermal behavior of a metal embedded fiber Bragg grating sensor" *Smart Mater. Struct.* 10 (2001) pp575–579

153. http://www.tangram.co.uk/TI-Polymer-PMMA.html#GP accessed 30/1/08

154. F.A. Khayyattt and P. Stanley "The dependence of the mechanical, physical and optical properties of Araldite CT200 /HT 907 on temperature over the range -10°C to 70°C" *J. Phys. D: Appl. Phys.*, Vol. 11, 1978. Pp 1237-1247.

155. http://www.gaitrite.com/Products/index.html

156. http://www.motionanalysis.com

157. A.S. Main, B.M. Cowie and D.J. Webb, "Low Cost Distributive Sensing Smart Surface", *18th International Conference on Optical Fiber Sensors, OSA*, (Oct 2006) paper FA5.

158. R.W. Fallon, L. Zhang, I. Bennion, "Multiplexed identical broad-band-chirped grating interrogation system for large-strain sensing applications" *IEEE Photonics Technology Letters*, v 9, n 12, Dec. 1997, p1616-18.

159. Prologix £100 http://store.prologix.biz/gpco.html?gclid=CIL5lKz6rZECFQ6hQwodmUbDeg accessed 5/2/08.

160. Quancom £350 (accessed 5/2/08) http://www.quancom.de/quancom/quancom01.nsf/home_prod_eng.htm?OpenFrameSet&Frame=unten&Src=http://www.quancom.de/qprod01/eng/pb/pcigpib_1.htm

161. D. I. Hanson and B. D. Prowell, "Evaluation of circular texture meter for measuring surface texture of pavements," tech. rep., *National Center for Asphalt Technology*, Auburn University, Auburn, Alabama, September 2004. NCAT Report 04-05.

162. "Strategic plan for improved concrete pavement surface characteristics." http://www.cptechcenter.org/publications/surface char exec summary.pdf, July 2006.

163. K. Creath and J. C. Wyant "Absolute measurement of surface roughness" *Applied Optics* (1990) Vol. 29, No. 26 pp3823 – 7.

164. J. Dargahi and S. Payandeh, "Surface texture measurement by combining signals from two sensing elements of a piezoelectric tactile sensor," in *Proceedings of the SPIE*, 3376, pp. 122–128, The International Society for Optical Engineering, 1998.

165. Y. Tada, K. Hosoda, Y. Yamasaki, and M. Asada, "Sensing the texture of surfaces by anthropomorphic soft fingertips with multi-modal sensors," *Proceedings 2003 IEEE/RSJ International Conference on Intelligent Robots and System*, 1, pp. 31-35, (Las Vegas, USA), October 2003.

166. H. Shinoda, M. Uehara, and S. Ando, "A tactile sensor using three-dimensional structure," *Proceedings, 1993 IEEE International Conference on Robotics and Automation*, 1, pp. 435–441, IEEE, May 1993.

167. Y. Mukaibo, H. Shirado, M. Konyo, and T. Maeno, "Development of a texture sensor emulating the tissue structure and perceptual mechanism of human fingers," *Proceedings of the 2005 IEEE International Conference on Robotics and Automation*, pp. 2576–8251, IEEE, (Barcelona, Spain), April 2005.

168. D. K. Pai and P. R. Rizun, "The what: A wireless haptic texture sensor," *Proc. Eleventh Symposium on Haptic Interfaces for Virtual Environment and Teleoperator Systems*, 2003.

169. Mayol-Cuevas, W.W.; Juarez-Guerrero, J.; Munoz-Gutierrez, S "A first approach to tactile texture recognition", *Proc IEEE International Conference on Systems, Man, and Cybernetics, 1998.* Vol 5, 1998 pp4246 - 4250

170. Barbara Cowie, Thomas Allsop, John Williams, David Webb, Ian Bennion, and Matthew Fisher "An optical fiber Bragg grating tactile sensor" *Proc. SPIE* Vol. 6585, 65850I (May. 16, 2007)

171. Patent application Ref: G30705147.7

172. T. Allsop, D. J. Webb and I. Bennion "Investigations of the Spectral Sensitivity of Long Period Gratings Fabricated in Three-Layered Optical Fiber" *Journal Of Lightwave Technology* (2003), Vol. 21, No. 1, pp264 – 268.

173. http://www.fibercore.com/ accessed 15/2/08

174. http://www.aerovac.com/

175. X. Zhang, Z. Wu, and B. Zhang, "Strain dependence of fiber Bragg grating sensors at low temperature," *Optical Engineering* 45, may 2006.

176. H. Dobb, K. Kalli and D.J. Webb "Temperature-insensitive long period grating sensors in photonic crystal fibre" *Electronics Letters* (2004) Vol. 40 No. 11.

177. V. Ishler, D. Wolfgang, and D. Griswold "Prevention and control of foot problems in dairy cows" Department of Veterinary Science and Department of Dairy and Animal Science
The Pennsylvania State University http://www.das.psu.edu/dairynutrition/documents/foot.pdf

178. Peine, W.J., Wellman, P.S., Howe, R.D., "Temporal Bandwidth Requirements for Tactile Shape Displays,"*Proceedings, Sixth Annual Symposium on Haptic Interfaces for Virtual Environment and Teleoperator Systems, ASME International Mechanical Engineering Congress and Exposition*, **61**, pp.107-113, Dallas, 1997.

179. http://www.thorlabs.com/NewGroupPage9.cfm?ObjectGroup_ID=285&pn=FGA21

180. Huang, B., Chen, M., Huang P., and Xu, Y. "Gait Modeling for Human Identification" *Proceedings of 2007 IEEE International Conference on Robotics and Automation* pp. 4833-4838. *Rome, Italy, April 2007.*